



EUROPEAN MECHANICAL SCIENCE

 OPEN
ACCESS

ISSN: 2587-1110

Volume 5
Issue 2
June 2021



Editor in Chief: M. Ozcanli

Editor in Chief

Mustafa Ozcanli (Automotive Engineering, Cukurova University, Turkey)

Editors

Sandra Spaszkievicz (West Pomeranian University of Technology, Poland)
Iva Petrikova (Applied Mechanics, Technical University of Liberec, Czech Republic)
Elżbieta Piesowicz (West Pomeranian University of Technology, Poland)
Tomeh Elias (Vehicles and Engines, Technical University of Liberec, Czech Republic)
Aleksandra Borsukiewicz, West Pomeranian University of Technology, Poland
Alptekin Ergenç (Automotive Engineering, Yildiz Technical University, Turkey)
Hasan Serin (Automotive Engineering, Cukurova University, Turkey)
M. Atakan Akar (Automotive Engineering, Cukurova University, Turkey)
Ahmet Çalık (Mechanical Engineering, Mersin University, Turkey)
Tayfun Ozgur (Automotive Engineering, Cukurova University, Turkey)
Cihat Aydın (Materials Engineering, Mersin University, Turkey)

Layout Editor

Ahmet Calik (Mersin University, Turkey)

Secretary

Şafak Yıldızhan (Cukurova University, Turkey)

Indexed / Abstracted in:

TR-Dizin, CrossRef, Index Copernicus, Journal Factor, Rootindexing, ResearchBip, JournalFactor, JIFACTOR, Google Scholar, I2OR, Cosmos Impact Factor, International Innovative Journal Impact Factor (IIJIF), Scientific Indexing Services, InfoBase Index, Scientific Journal Impact Factor

Aims and Scopes

European Mechanical Science (EMS) is an international, peer reviewed journal which publishes full length original research papers, reviews related to all areas of Mechanical Engineering such as: Solid Mechanics, Materials Engineering, Automotive Engineering, Fluid Mechanics, Thermal Engineering, Engine and Power Engineering, Dynamics & Control, Robotics & Mechatronics, Transportation Engineering, Computational Mechanics, Design, Systems, Manufacturing, Bio-Medical Engineering; Process Engineering, Aerospace Engineering. No charges are required from the Authors to publish the articles.EMS is a quarterly published journal operating an online submission and peer review system. It allows authors to submit articles online and track their progress via its web interface.

<http://dergipark.gov.tr/ems>

Contents

- Research Paper** Experimental Investigation of the Hybrid Damper Clutch System Under Dynamic Conditions of an Automobile Powertrain 44
Mehmet Onur Genç, Süleyman Konakçı, Necmettin Kaya, Çağlar İmer, Ali Kamil Serbest
- Research Paper** On the Effect of Through-Thickness Integration for the Blank Thickness and Ear Formation in Cup Drawing FE Analysis 51
Bora Sener, Toros Arda Akşen, Mehmet Firat
- Research Paper** A Numerical Investigation of The Fracture Energy of Materials for Fuel Cell End Plates 56
Adem Avcu, Naghdali Choupani, Gökhan Tüccar
- Research Paper** Spark Plasma Sintering of Nano Silicon Carbide Reinforced Alumina Ceramic Composites 64
Mustafa Guven Gok
- Research Paper** Building up Mathematical Modeling Using Spot Welding Parameters and Prediction Weld Nugget by Minitab 71
İlhan Çekic, Kadir Çavdar
- Research Paper** Fibre Volume Fraction and Impact Strength Analysis of Reinforced Polyester Composites 80
Dickson David Olodu, Osagie Ihenyen
- Research Paper** Thermal Comfort in an Office Room Using Square Diffuser 86
Alper Yildirim, Coskun Ozalp

Experimental Investigation of the Hybrid Damper Clutch System Under Dynamic Conditions of an Automobile Powertrain

Mehmet Onur Genç*¹ , Süleyman Konakçı¹ , Necmettin Kaya² , Çağlar İmer¹ ,
Ali Kamil Serbest³ 

¹Valeo Automotive Systems, Bursa, Turkey.

²Bursa Uludağ University, Mechanical Engineering, Bursa, Turkey – necmi@uludag.edu.tr

³Angst-Pfister Advanced Technical Solutions, Bursa, Turkey – alikamil.serbest@angst-pfister.com

Abstract

Automobile components are subjected to high dynamic forces and vibrations under operational conditions, which need detailed system analysis for work properly. Clutch is one of the important parts of the automobile powertrain system with torque transmission controlling and vibration damping properties. Metallic helical springs are widely preferred within the clutch discs with their durable mechanic properties against dynamic variables on an automobile. Recently, the rubber components are used in the automotive industry due to some advantages such as wear reduction, cost etc. Therefore, in this study, the clutch system consists of metallic and rubber spring dampers are investigated to observe mechanical behaviours together in use. In order to investigate this hybrid damper behaviour under dynamic condition in clutch system, the torsional endurance was observed with the functional bench tests to simulate driving condition. Results show that the Hybrid dampers have a close durability performance within acceptable damper torque decrease found according to experimental vehicle test results. These results also shows that for medium vehicle segments, Hybrid damper is an alternative within the aimed vehicle comfort level. Hybrid clutch dampers are new in literature, and firstly were investigated in this study in terms of endurance capability.

Keywords: Hybrid damper, Rubber damper, Metallic damper, Hyper-viscoelastic modeling, Torsional fatigue, Clutch disc, Powertrain system, Vehicle comfort

1. INTRODUCTIONS AND MAIN SECTIONS

Automobile clutch system components are subjected to high dynamic forces under operational conditions. The clutch disc is in charge of damping the vibrations coming from the engine properly to improve driving comfort and transmitting the torque. Torque transmission role of a clutch disc is achieved with a damper system which consists of metallic springs conventionally.

A clutch disc transmits clamped force through the friction from pressure plate and flywheel (Figure 1). During gear shifting, drivers push the clutch pedal and clutch disc locates to disengagement position, which provides torque cutting to enable gear shifting. Torque (T) which is transmitted by friction between flywheel and pressure plate is proportional with clutch disc facing friction coefficient f_s , clamp load $F(N)$, a number of friction surface N and medium diameter of friction surface R_m (Eq.1).

$$T = f_s F N R_m \quad (1)$$

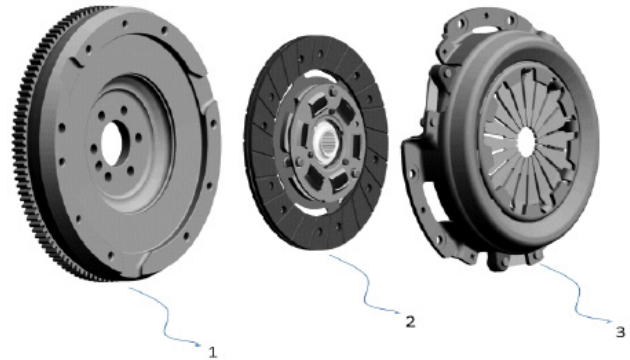


Figure 1. Clutch damper system

Under driving conditions between engine and transmission relative motions occur between engine and transmission due to dynamic variables. Relative motion between flywheel and clutch disc causes slippage that leads to dissipated energy. During slippage, thermal load in clutch house increases and this may cause permanent or temporary changes on materi-

* Corresponding author
Email: mehmetonurgenc@gmail.com



al properties of the components. The dissipated energy and wear on friction materials increase with slipping duration. Under normal working conditions, the amount of kinetic energy converted into heat leads to temperature increase. Generated heat flux during the slippage phase is distributed between flywheel and clutch based on their thermal diffusivity. The heat is transferred by conduction between the solid parts depending on their specific heat C_p [J/kg K] and mass m [kg] (Eq. 2).

$$Q = M C_p \Delta T \tag{2}$$

Rubber materials have viscoelastic properties that need high attention before modeling such as ‘Mullins effect’, which is called as stress softening behavior of cross-linked rubbers at first cycles. Rubbers have variable hysteresis behaviors which change based on variable dynamic conditions apart from metallic springs. During rubber damper spring design, some countermeasures should be taken into account due to its viscoelastic properties, which subject to loss of stiffness under dynamic condition. Rubber based materials are accepted as incompressible and have a specific range of Poisson ratio and young modulus. Figure 2 shows the experimental compression test results of the standard test specimen measured in this study compared to metal spring. This graph explains the importance of stabilization process of rubbers for the chosen strain rate in the dynamical system. Rubbers show nonlinear load characteristics, and they are modeled with different kinds of material behaviors. Instead, metal springs tend to show same linear force reaction under compression.

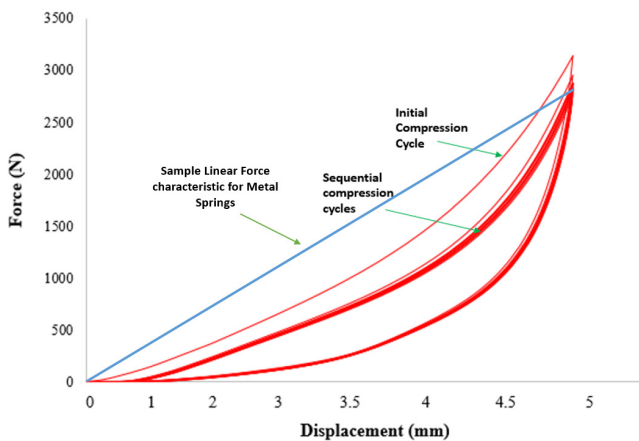


Figure 2. The experimental test of ‘Mullins Effect’ vs. Metal spring linear characteristic

There are both advantages and disadvantages of using rubber springs in automobile clutch systems compared to metal helical springs. The major advantage in using rubber springs is the low-cost. Besides that, since the internal hysteresis of the rubber springs is higher than the metal helical spring, under normal driving conditions, it is expected that the vibration amplitude transmitted from engine to gearbox may be lower with higher damping coefficient. As a disadvantage of rubber spring, damping torque loss occurs due to loss of stiffness within the time related to viscoelastic material behavior. In metal helical springs, the stiffness is more durable

due to the metal material behavior during product lifetime. The hybrid damper system (Figure 3) is the new generation design for the clutch system technology, and in the near future, the usage of this damper type is expected to be increased. The system consists of metallic and rubber springs in the clutch disc.

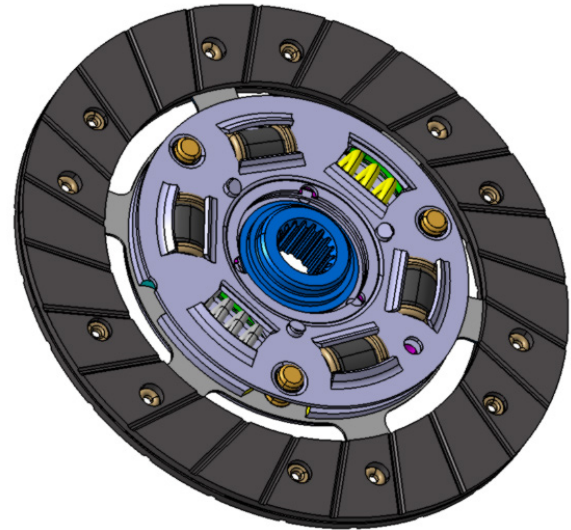


Figure 3. Hybrid damper clutch disc design

In the literature, rubber-based materials have been investigated with different approaches. Jadhav et al. [1] have studied the hyperelastic modeling of the mechanical behaviors of rubber materials, such as natural rubber and silicone, and rubber materials, ranging from muscles to biological materials such as skin texture, by hyperelastic modeling. Marvalova [2] experimentally measured the viscoelastic stress response by characterizing the mechanical behavior of rubber structures in deformation processes under isothermal conditions. Viscoelastic stress relaxation behaviors were investigated by examining the structural function parameters under variable frequencies. Zhang and Zhang [3] studied the viscoelastic parameters of rubber bushings and studied thermal analysis, which determines their physical properties by DMA (Dynamic Mechanical Analysis). A new approach to the prediction of hysteresis losses based on the interaction between molecular chains of polymer structures has been proposed. Bani et al. [4] observed the temperature of increased rubber-metal springs under loading conditions and observed heat accumulation due to hysteresis losses and low rubber thermal conductivity resulting from increased temperature. They categorize physical and chemical impairments as a result of heat accumulation, which is the main cause of aging in rubber, and point out that the increase in hardness and the decrease in damping ability. Zhang and Zhang [5] investigated the deterioration and the parameters of the thermal behavior of the rubber caused by the working conditions in the rubber bushes used in aviation or aviation to reduce noise and vibration. The data obtained at a different frequency and amplitude values are modeled by modeling the temperature-dependent change in viscoelastic behavior. Genç and Kaya [6] investigated the elastomer damper design under

various conditions in their study. They used NBR rubber material in their rubber spring. According to their results, in case of full elastomer damper was used with NBR material, the clutch damper tends to lose %15 stiffness in first 10K km driving. These results show the sensitive design necessity of rubber dampers in automotive clutch system due to stiffness losing issue.

The focus of this article is to investigate Hybrid Damper Clutch behaviors in automotive clutch system. In order to obtain the results, the same clutch design was produced with metal and rubber springs. The Hybrid damper systems have newness for its area, and during this study, the system was investigated and functional test results were obtained. Torsional endurance behavior is the most important parameter for the damper systems because the target damping level can be achieved in case the nearly constant damper stiffness level is obtained. Figure 4 explains the general workflow conducted in this study.

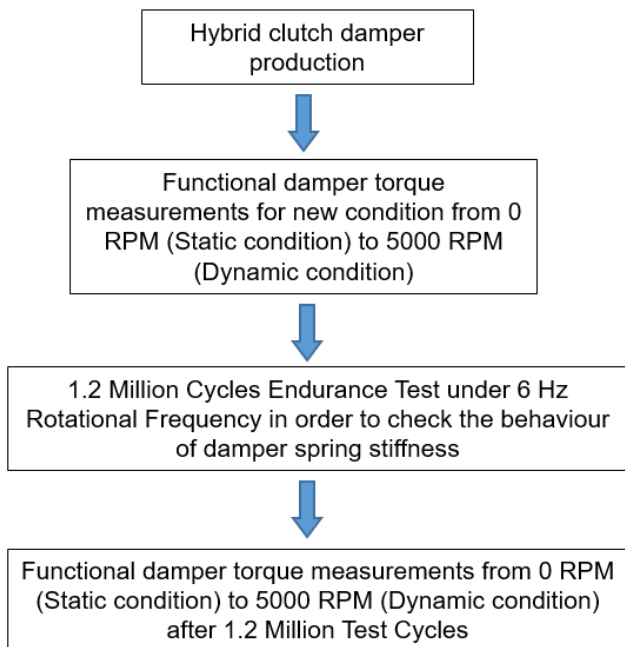


Figure 4. Workflow performed in the study

2. MATERIAL AND METHODS

In this section, the properties of the Hybrid Damper system and the test methods are investigated. Figure 5 shows the prototype of the Hybrid Damper consists of four (4) rubber-based springs and two (2) metallic springs. The geometry and the number of springs can be selected according to clutch house design and automobile properties. The damper system should be checked and verified in terms of system endurance and robustness.

In an automobile powertrain system, it is expected that there will be a loss of stiffness in the rubber damper spring during the life of the product in case of temperature, frequency compression, loss of length (creep). In parallel with these stiffness losses, the hysteresis (damping torque) varies due to internal friction changes. Due to these situations, it is

expected that the filtering properties of the clutch damper will decrease in the following kilometers. These features can be obtained with sensors and data collection devices in long vehicle tests and NVH tests. With the loss of stiffness, vibrations are expected to be less dampened and the vibration amplitudes measured in the transmission are higher than in the past. These situations lead to a decrease in vehicle comfort and an increase in the level of vibration felt by passengers.

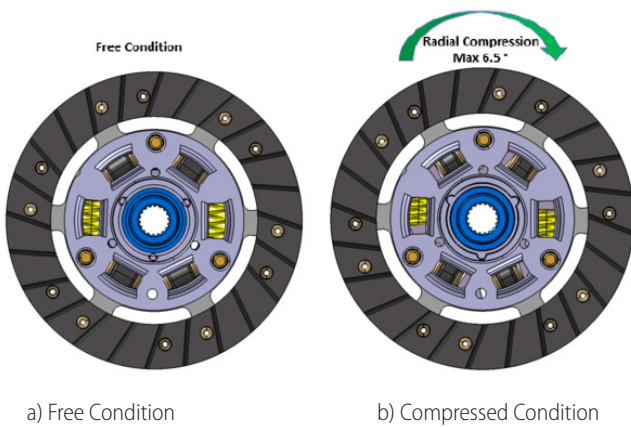


Figure 5. The prototype of hybrid damper clutch disc

Dynamic torsional endurance test simulates the worst condition on the automobile with representing the endurance of springs against torque oscillations generated by the engine. Many factors have high effects on the torque oscillations of the automobile such as driver profile, air conditioner on/off, lightening on/off, fuel type gasoline/diesel, fuel quality, engine maintenance quality, abusive usage, etc. In this study, the clutch discs with hybrid damper have been subjected to dynamic torsional fatigue compressions under various RPM (revolution per minute) with 6 Hz test frequency. Figure 6 shows the torsional compression on the clutch disc during the dynamic torsional endurance test. The test was performed at 1000, 2000, 3000, 4000 and 5000 RPM with a total 1.2 M cycles. According to experimental vehicle test results obtained during driving condition, 1.2 Million cycles equal to 100K Km in real vehicle usage [7]. The target is to observe the torsional endurance including stiffness loose and wear behavior on the rubber springs. Conversely, the metallic springs are expected to keep its stiffness level during the test condition thanks to its material properties.

Figure 7 shows the compression and release phases of rubber springs on the torsional durability test bench. In this study, the clutch disc was compressed to 6,5° angular travel and then released phase was started till to starting position. Hysteresis is the loss of damper torque that occurred due

to internal friction in the hybrid damper. Clutch disc using rubber springs is fitted on “Dynamic torsional endurance test bench (Figure 8) with test flange providing relative motion at each cycle of test. The test machine consists of two main parts, one of them is the dynamic controlling screen, which enables to control mechanical test machine under option from 1 Hz to 6 Hz. Second part is the mechanical test machine operates based-on the hydraulic forces. Disc assembly using rubber springs is fitted with test flange providing relative motion at each cycle of test. Test was performed up to 5000 RPM (revolution per minute) at 6 Hz compression frequency. During the rotations from 0 RPM to 5000 RPM, the hybrid clutch damper is forced to withstand 6 Hz oscillations which simulates possible endurance performance during driving conditions on the road. As a result of this functional bench test, the endurance performance under dynamic conditions can be predicted.



a) Free Condition b) Compressed Condition
Figure 6. Torsional endurance test a) Clutch disc at free condition b) Clutch disc compressed condition on the test bench

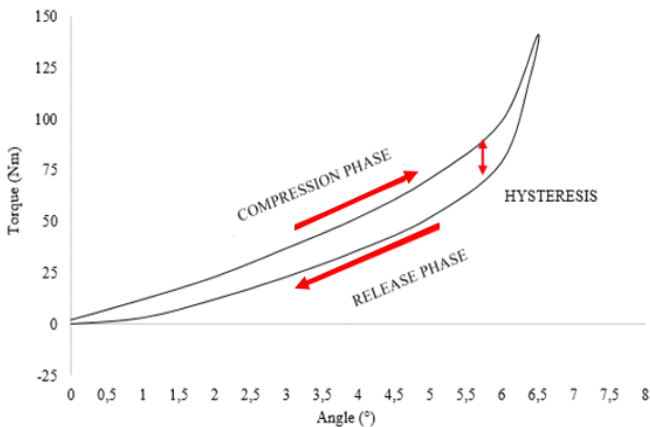


Figure 7. Compression and release phases of rubber springs

Figure 9 shows the dynamic condition effect on damper springs. Centrifuge effect is expected to increase in parallel to RPM. By means of centrifuge effect, measured damper torque is increased because of friction force rising between damper springs and the metallic components such as retainer plate, drive plate of the clutch damper disc.



Figure 8. Dynamic torsional endurance test bench

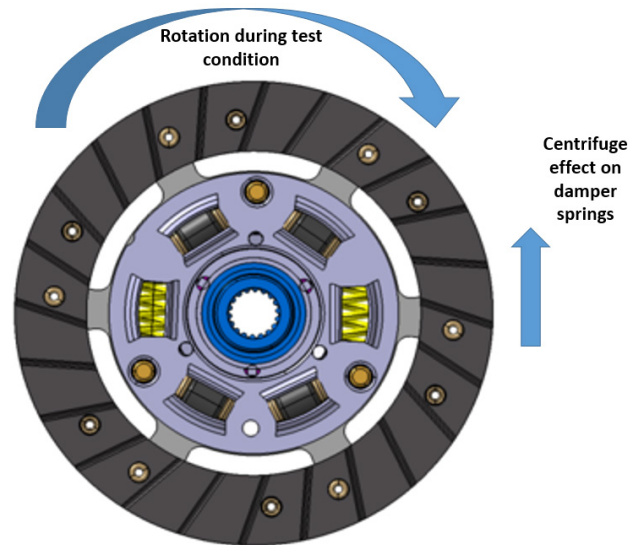


Figure 9. Centrifuge effect on damper torque behavior

3. ANALYSIS AND DISCUSSIONS

3.1. Experimental Results

In this section, the dynamic torsional endurance test performed to hybrid damper clutch disc is observed and the results are evaluated. Figure 10 shows the torsional damper curve prior to the dynamic functional curve. The graph explains the dynamic damper torque of the hybrid damper system. The damper torque graph shows that the dynamic torque of the clutch damper system tends to increase during the RPM value is drastically increased. Table 1 indicates the detailed values for each RPM compared to measured torque level.

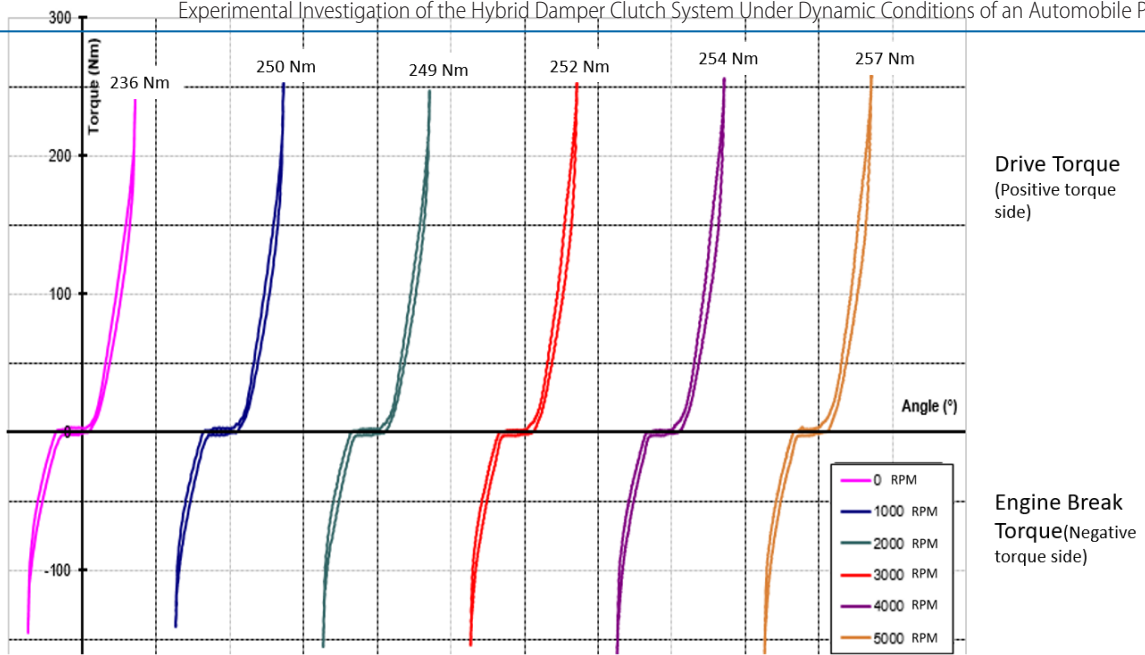


Figure 10. Dynamic torsional endurance test under 6 Hz & damper torque measurements before the test under various RPM

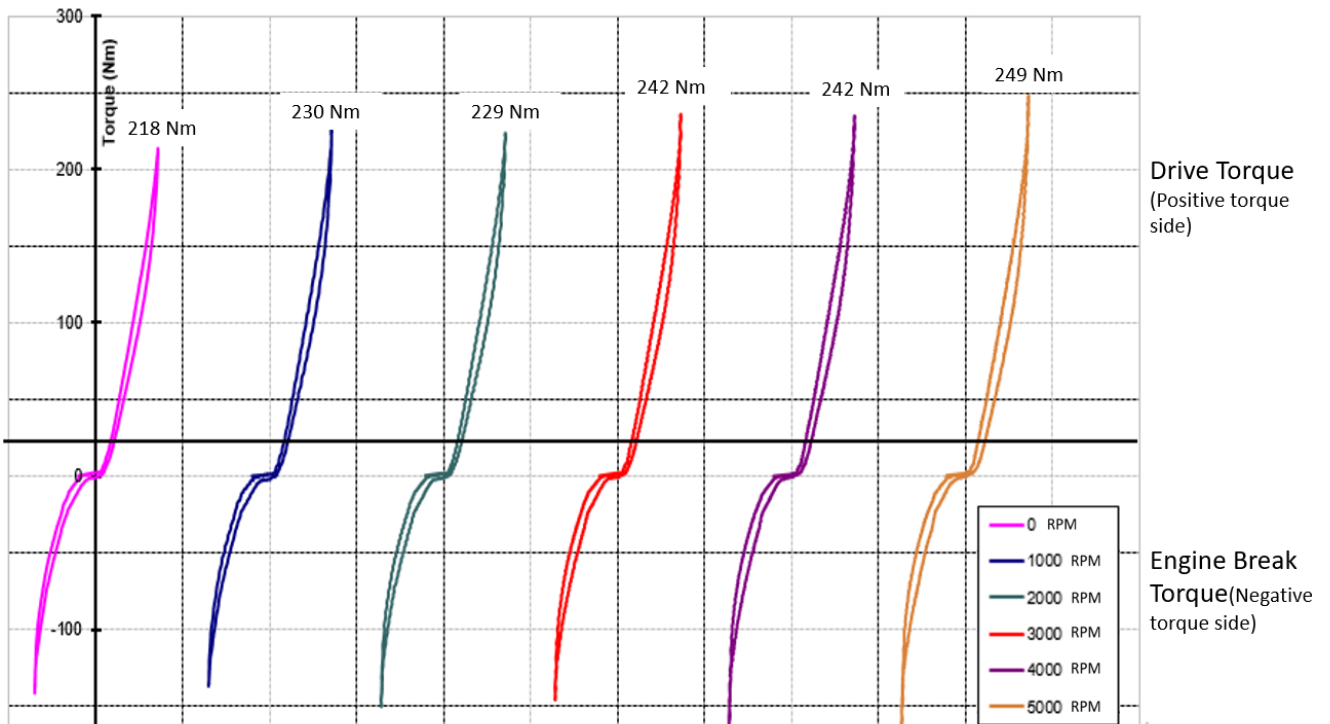


Figure 11. Dynamic torsional endurance test under 6 Hz & damper torque measurements after 1.2 M cycle under various RPM

Table 1. Measured dynamic torque under dynamic condition & Initial Condition

RPM (Revolution per minute)	Damper torque measured (Nm)
0	236
1000	250
2000	249
3000	252
4000	254
5000	257

Figure 11 is the graph of dynamic torsional endurance test measured after 1.2 M cycle. Results show that the damper torque decrease is observed at the minimum level. This information shows the endurance level of the hybrid damper system is verified for the defined clutch disc design. Table

2 indicates the detailed values for each RPM compared to measured torque level after 1.2 M Cycle.

Table 2. Measured dynamic torque under dynamic condition & After 1.2 M Cycle

RPM (Revolution per minute)	Damper torque measured (Nm)
0	218
1000	230
2000	229
3000	242
4000	242
5000	249

Table 3 is the comparison of the full metallic (conventional) damper system and hybrid damper system designed for the

same vehicle application (Figure 12). Both design have same geometries and components except damper spring group. Hybrid damper system consists of four (4) rubber spring and two (2) metallic spring compared to full metallic system which has 6 metallic spring. The clutch type used in this study is of medium torque transmission capacity and used in B segment passenger vehicles. Figure 13 shows the comparable geometries of both springs. Due to envelope limits, metallic and rubber springs were designed for nearly same mechanical reaction forces, also this phenomena widely called as damper stiffness. The point that also needs attention is metallic spring production process has more steady geometrical tolerances, however the rubber springs have not this kind of stability due to injection process. This is also the disadvantages of rubber spring production process.

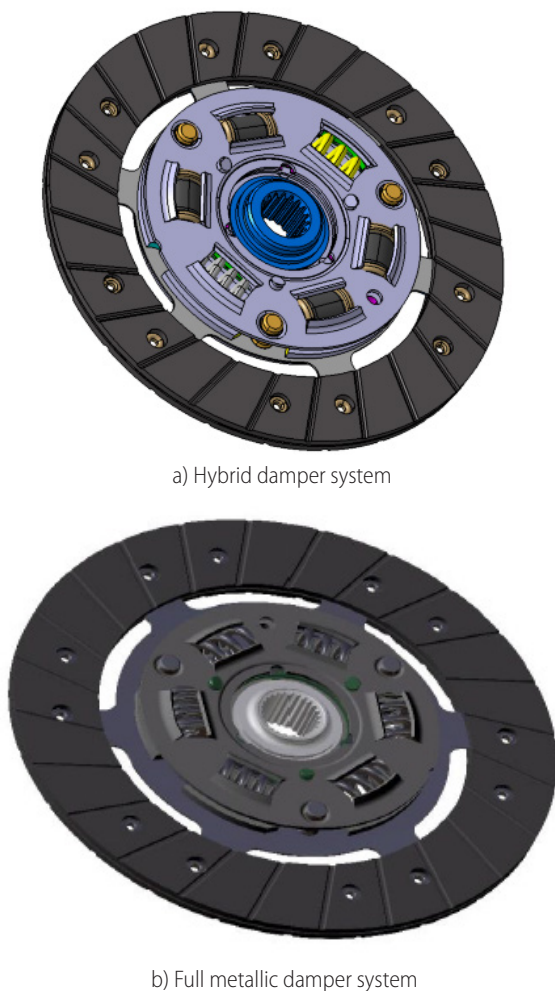


Figure 12. Hybrid damper system design vs. Full metallic (conventional) damper system design

Metallic damper test was performed in Valeo Automotive plant [7]. Results show that the damper torque loss is observed about 3% for the full metallic system, however, the hybrid damper system was observed about 8%. This result explains that the hybrid damper system can be operated in a safe condition and the rubber damper inside the system can keep its stiffness level during the product life. These results show that full metallic spring usage creates more safety

in terms of stiffness decrease compared to Hybrid damper system. However, damper torque decrease can tolerate the deviations up to 10% according to experimental test results on the road [7]. Nevertheless, in case full rubber spring uses instead of hybrid or full metallic system, more stiffness loose is expected which can create critical torque transmissibility [6].



Figure 13. Detailed view of metallic and rubber spring

Table 3. Damper torque comparison of Hybrid & Full Metallic damper systems at static condition (0 RPM)

	Max damper torque before the test (Nm)	Max damper torque after 1.2 M dynamic torsional endurance test (Nm)	Damper torque loss ratio (%)
The full metallic damper system [7]	217	210	3
Hybrid damper system	236	218	8

3.2. Vehicle comfort overview based on experimental results

Vehicle comfort is one of the phenomena for vehicle clutch design. In literature, this condition is called as Noise, Vibration and Harshness (NVH). Generated torque transmission on powertrain system creates unwanted oscillations in the system, and clutch damper disc is one of the damping section showing in Figure 14. This 1-D model is prepared with LMS Amesim software with real vehicle configuration data. This schematic view works based on mathematical model, and this means that major deviations on damper stiffness more likely creates resonance changes on the sub-sections of the powertrain system such as Gearbox, Propeller Shaft etc [13, 14]. For the vibration analysis of rotational components, as in vehicle powertrain system, angular frequency should be taken into account which has directly linked with stiffness (k) in mathematical condition. Therefore, in case the performance reliability of vehicle comfort is compared in sequence for all three (3) conditions, full metallic damper has consistent better NVH performance than the Hybrid and Rubber dampers due to less stiffness decrease within the time. However, Hybrid dampers have average stiffness loose, and it can be obtained from the experimental results that Hybrid damper system can be preferred in most cases for medium segment vehicles such as B Segment and low torque C Segments (Table 3).

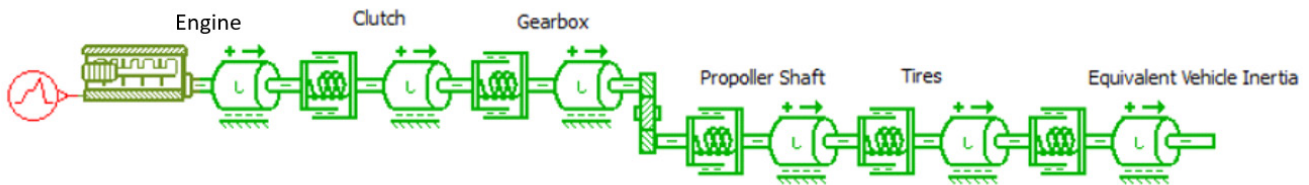


Figure 14. 1-D Modeling of vehicle powertrain system for designed Hybrid damper clutch

4. CONCLUSIONS

This study investigates the design of the hybrid damper system under dynamic conditions verified with dynamic torsional endurance test. In the study, the produced samples of hybrid damper clutch disc were subjected to dynamic torsional endurance test comparatively with a full metallic clutch damper system. The results show that the hybrid damper system design loses its damper torque level averagely 8% after 1.2 M cycles which equals 100K Km vehicle usage in real driving condition, however, the conventional full metallic damper system design loses 3% with the same test condition. These results show that the hybrid damper system design is safe because the damper torque loss is under 10%, which is accepted as safety limit. During driving conditions, the vehicle is supposed to show variant driving profiles which results in different product life with small deviations. The functional bench test results obtained in this study simulate the real driving condition, according to results, hybrid damper systems can be an alternative solution of full metallic damper clutches in automotive industry.

Acknowledgements

The authors gratefully acknowledge the support of TUBITAK under grant the 3180181 project ongoing with collaboration between Valeo Automotive, Angst-Pfister and Bursa Uludag University.

REFERENCES

- [1] Jadhav, N., Bahuliker, S.R., Sapate, N.H. (2016), "Comparative Study of Variation of Mooney-Rivlin Hyperelastic Material Models under Uniaxial Tensile Loading" Vol-2 Issue-4, IJARII- ISSN(O)-2395-4396 Publishing Corporation Scientific World Journal, Article ID 379196
- [2] Marvalova, B. (2007), "Viscoelastic Properties of Filled Rubber. Experimental Observation and Material Modelling", *Engineering Mechanics*, Vol.14, No.1/2, p.81–89
- [3] Zhang, Z., Zhang, H. (2014), "Viscoelastic Parameter Identification based Structure-Thermal Analysis of Rubber Bushing", *Global Journals of Research in Engineering*, Volume 14 Issue 3 Version 1.0
- [4] Bani, M. S., Stamenkovi, D.S., Miltenovi, V.D., Milosevic, M.S., Miltenovi, A.V., Djeki, P.S., Rackov, M.J. (2012), "Prediction Of Heat Generation In Rubber Or Rubber-Metal Springs" *Thermal Science*, Vol. 16, Suppl. 2, pp. S527-S539 Title
- [5] Zhang, Z., Zhang, H. (2016), "FEA based Dissipation Energy and Temperature Distribution of Rubber Bushing" *International Journal of Engineering Research and Applications* ISSN: 2248-9622, Vol. 6, Issue 1, pp.48-6
- [6] Genc, M. O., Kaya, N., "Design and verification of elastomer spring damping system for automobile powertrain systems", *Journal of the Faculty of Engineering and Architecture of Gazi University* 35:4 (2020) 1957-1971
- [7] Valeo Technical Documentation, 2019, Bursa, Turkey
- [8] Melnik, R.V.N, Strunin, D.V, Roberts, A.J. (2005), "Nonlinear Analysis Of Rubber-Based Polymeric Materials With Thermal Relaxation Models", *Numerical Heat Transfer, Part A*, 47: 549–569
- [9] Pacheco, J. L., Bavastrri, C.A., Pereira, J.T. (2015), "Viscoelastic Relaxation Modulus Characterization Using Prony Series, *Latin American Journal of Solids and Structures*" Vol:12, pp 420-445
- [10] Monsia, M. D. (2011), "A Simplified Nonlinear Generalized Maxwell Model for Predicting the Time-Dependent Behavior of Viscoelastic Materials" *World Journal of Mechanics*, 1, 158-167
- [11] Mohammed, M.A. (2014), "Visco-Hyperelastic Model for Soft Rubber-like Materials", *Sains Malaysiana*, Vol: 43(3), pp 451–457
- [12] Hwang, S. J., Chen, J. S., Liu, L., Ling, C. C., "Modelling and Simulation of a powertrain system with automatic transmission" *International Journal of Automobile Design*, 2000, Vol. 23, No:1
- [13] Macor, A., Benato, A., Rossetti, A., Bettio, Z., "Study and Simulation of a Hydraulic Hybrid Powertrain" 72nd Conference of the Italian Thermal Machines Engineering Association, ATI2017, 6–8 September 2017, Lecce, Italy
- [14] Genc, M. O., Kaya, N. (2018). Modelling and Experimental Investigation of Clutch Damper Spring Stiffness on Truck Driving Comfort. *International Journal of Advances on Automotive and Technology*, 2(2): 121-136.
- [15] Wu, H., Wu, G., "Driveline Torsional Analysis and Clutch Damper Optimization for Reducing Gear Rattle" *Shock and Vibration* Volume 2016, Article ID 8434625, 24 pages <http://dx.doi.org/10.1155/2016/8434625>
- [16] Chen, X., Wu, G., Wu, H., "The Nonlinear Characteristics Impact of Multi-Stage Stiffness Clutch Damper on the Automobile Creeping" *SAE 2016 World Congress and Exhibition*, DOI: 10.4271/2016-01-0431, April 2016



On the Effect of Through-Thickness Integration for the Blank Thickness and Ear Formation in Cup Drawing FE Analysis

Bora Şener¹ , Toros Arda Akşen^{2*} , Mehmet Fırat² 

¹Yildiz Technical University, Faculty of Mechanical Engineering, Mechanical Engineering Department /Istanbul, Turkey

²Sakarya University, Faculty of Engineering, Mechanical Engineering Department/Sakarya, Turkey

Abstract

Various numerical parameters such as element size, mesh topology, element formulations effect the prediction accuracy of sheet metal forming simulations and wrong selection of these parameters can lead to inaccurate predictions. Therefore, selection of proper numerical parameters is crucial for obtaining of realistic results from finite element (FE) analyses. In the present work, influence of the number of through-thickness integration points from the numerical parameters was investigated on the cup drawing simulation. Highly anisotropic AA 2090-T3 aluminum alloy was selected as test material and the anisotropic behavior of the material was defined with Barlat 91 yield criterion. Firstly, cup drawing model was created with implicit code Marc and then FE analyses were performed with five, seven and nine layers to investigate the effect of number of through-thickness integration points. The computed earing profiles and thickness strain distributions were compared with measurements. Comparisons showed that the angular locations of maximum cup heights and thickness strain distributions along rolling and transverse directions were captured accurately by Yld91 yield criterion and also it was observed that the layer number effects the maximum cup height and thickness strain distribution along the rolling direction.

Keywords: Cup Drawing, Finite Element Simulation, Earing Profile, Thickness Strain

5. INTRODUCTION

Governments force automotive companies to reduce exhaust emissions and improve fuel efficiency. In order to satisfy these requirements, engineers develop projects on reducing vehicle weight [1]. At this point, aluminum (Al) alloys become attractive for automotive manufacturers because of their lightweight and strength-to-weight ratios. Although Al alloys are preferred by most automotive manufacturers, modelling of these materials is difficult due to complex anisotropic behaviors. Anisotropic behavior of the sheet materials is represented by orthotropic anisotropic yield criteria. Various anisotropic yield criteria have been developed in the literature. The first anisotropic yield criterion was proposed by Hill in 1948 [2]. Hill48 criterion has a quadratic form and it gives consistent results for steels. However, conventional Hill's quadratic criterion can't represent the anisotropic behavior of aluminum alloys. According to Hill48 yield criterion, biaxial yield stress ratio (σ_b / σ_0) is lower than unity when the normal anisotropy coefficient (r_n) is less than unity and also $r_0 > r_{90}$ when $\sigma_0 > \sigma_{90}$. However, experimental studies performed by Woodthorpe and Pearce for some Al alloys showed that σ_b / σ_0 was always

around 1.1 and r_n varied between 0.5 to 0.6 and $r_0 > r_{90}$ then $\sigma_0 < \sigma_{90}$ [3]. This behavior was referred as "the first and the second anomalous" behavior by researchers. Therefore, non-quadratic yield functions are required to use for describing the anisotropic behavior of these materials. Hill developed a non-quadratic yield criterion in 1979 [4]. Hill79 criterion can model the first anomalous behavior, but it couldn't model second anomalous behavior of Al alloys. Then, Hill improved his yield criterion and proposed a new non-quadratic yield criterion in 1990 [5]. Hill90 criterion can describe both the first and second anomalous behaviors, but this model is not user friendly and it requires long simulation time for FE analysis. Unlike Hill's models, Barlat et al. developed various anisotropic yield functions for Al alloys that these functions are referred as Yld89 [6], Yld91 [7], Yld96 [8], Yld2000-2d [9] and Yld2004 [10] in the literature. These models are derived from linear transformation approach and give better results than Hill's models for Al-alloys.

Several studies have been carried out about the modeling of Al-alloys in the literature. Chung and Shah [11] defined the anisotropic behavior of AA 2008-T4 alloy using Barlat91

* Corresponding author
Email: ardaaksen@sakarya.edu.tr



(Yld91) yield criterion and performed FE analyses of the bulge and cup drawing tests. They compared the predicted bulge profiles, cup height and thickness values with experimental results. Similar studies were carried out by Yoon et al. [12] and Chung et al. [13]. They predicted earing profiles and thickness strain distributions with FE simulations and found good agreement between FE simulation and experiment. Then Yoon et al. used Yld91 yield criterion to predict earing of AA 2008-T4 alloy and compared with Hill48 [14]. Parente et al. modeled the cup drawing of AA 2008-T4 alloy with solid-shell elements and Yld91 yield criterion [15]. They applied the model to predict earing and obtained a good agreement with experimental results. Yoon et al. [16] applied Yld2004 yield criterion to predict earing of AA2090-T3 alloy. They used solid elements in FE analyses and successfully predicted the earing profile of the cup. Younas et al. [17] investigated the effect of solid-shell elements on the earing prediction and compared with standard solid elements. They performed FE simulations of cup drawing tests with Hill48, Yld91 and Yld2004 yield functions for AA2090-T3 alloy and obtained closer results with non-quadratic yield functions to the experiments. Although successful results were obtained in these studies, it is seen that researchers haven't performed any study about the influence of number of through-thickness integration points in cup drawing simulations.

In this study, this effect was investigated for highly anisotropic AA2090-T3 aluminum alloy. Anisotropy of the material was defined with Yld91 yield criterion and FE analyses were carried out with different number of integration points. Then the computed earing profiles and thickness distributions were compared with measurements.

6. MATERIAL AND METHOD

6.1. Plasticity Model

A yield criterion, a flow rule and a hardening rule must be defined in order to establish a plasticity model. Yield criterion defines the elastic boundary in stress space, flow rule determines the direction of plastic strain increment and hardening rule defines the evolution of yield surface. In this study, Yld91 yield criterion was used for definition of initial anisotropy of the material and the criterion is explained in below:

Yld91 is a six-component yield criterion and it is developed by Barlat et al. to identify anisotropic behavior of Al-alloys. This criterion is based on the linear transformation approach and expressed as the following:

$$\phi = |S_1 - S_2|^m + |S_2 - S_3|^m + |S_3 - S_1|^m = 2\bar{\sigma}^m \tag{1}$$

where $\bar{\sigma}$ is the effective stress, S_1 , S_2 and S_3 are the principal values of the transformed deviatoric stress tensor $S_{\alpha\beta}$,

$$S_{\alpha\beta} = \begin{bmatrix} S_{xx} & S_{xy} & S_{xz} \\ S_{yx} & S_{yy} & S_{yz} \\ S_{zx} & S_{zy} & S_{zz} \end{bmatrix} = \begin{bmatrix} \frac{C_2 C - C_2 B}{3} & C_6 H & C_5 G \\ C_6 H & \frac{C_1 A - C_3 C}{3} & C_4 F \\ C_5 G & C_4 F & \frac{C_2 B - C_1 A}{3} \end{bmatrix} \tag{2}$$

here

$$\begin{aligned} A &= \sigma_{yy} - \sigma_{zz}, & B &= \sigma_{zz} - \sigma_{xx}, & C &= \sigma_{xx} - \sigma_{yy}, \\ F &= \sigma_{yz}, & G &= \sigma_{zx}, & H &= \sigma_{xy} \end{aligned} \tag{3}$$

Linear transformation of the deviatoric symmetric stress tensor can be expressed as follows for plane stress conditions.

$$S_{\alpha\beta} = \begin{bmatrix} S_{xx} & S_{xy} & 0 \\ S_{yx} & S_{yy} & 0 \\ 0 & 0 & S_{zz} \end{bmatrix} = \begin{bmatrix} \frac{C_3(\sigma_{xx} - \sigma_{yy}) - C_2\sigma_{xx}}{3} & C_6\sigma_{xy} & 0 \\ C_6\sigma_{xy} & \frac{C_1\sigma_{yy} - C_3(\sigma_{xx} - \sigma_{yy})}{3} & 0 \\ 0 & 0 & -S_{xx} - S_{yy} \end{bmatrix} \tag{4}$$

where $C_{i=1-6}$ are the constants describing the anisotropy of the material. When $C_{i=1-6} = 1$, the material is isotropic and the criterion transforms Tresca yield criterion for $m=1$ or ∞ and von Mises criterion for $m = 2$ or 4 . The parameter m is related to the crystallographic structure of the material. This parameter is taken as 6 for body-centered-cubic and 8 for face-centered-cubic materials. Also yield surface is convex for $m > 1$. For the plane stress state, the number of constants reduces to four (C_b, C_c, C and C_6). These constants could be determined by solving the system of nonlinear equations [18]. Depending on the yield stresses along three directions ($0^\circ, 45^\circ$ and 90°) and equibiaxial yield stress (σ_b) these equations are written as following:

$$f_1(C_i) = \sigma_{eq}(\sigma_{xx} = \sigma_b, \sigma_{yy} = \sigma_b, \sigma_{xy} = 0) - \sigma_b = 0 \text{ for } i = 1, 2, 3, 6 \tag{5}$$

$$f_2(C_i) = \sigma_{eq}(\sigma_{xx} = \sigma_0, \sigma_{yy} = 0, \sigma_{xy} = 0) - \sigma_0 = 0 \text{ for } i = 1, 2, 3, 6 \tag{6}$$

$$f_3(C_i) = \sigma_{eq}\left(\sigma_{xx} = \frac{\sigma_{45}}{2}, \sigma_{yy} = \frac{\sigma_{45}}{2}, \sigma_{xy} = \frac{\sigma_{45}}{2}\right) - \sigma_{45} = 0 \text{ for } i = 1, 2, 3, 6 \tag{7}$$

$$f_4(C_i) = \sigma_{eq}(\sigma_{xx} = 0, \sigma_{yy} = 0, \sigma_{xy} = \sigma_{90}) - \sigma_{90} = 0 \text{ for } i = 1, 2, 3, 6 \tag{8}$$

The Newton-Raphson (N-R) numerical method was used to solve the system of nonlinear equations in this study (Eg.5-8).

Associated flow rule was used to determine the plastic strain increments. It can be expressed as following equation:

$$d\epsilon_{ij}^p = d\lambda \frac{d\phi}{d\sigma_{ij}} \tag{9}$$

where $d\epsilon_{ij}^p$ shows the increment in the plastic strain tensor, $d\lambda$ is the plastic multiplier, ϕ is the yield function and σ_{ij} denotes the Cauchy stress tensor. Isotropic hardening rule was assumed and hardening curve was defined with Swift power law is given in Eq. (10).

$$\sigma = K(\epsilon_0 + \epsilon_p)^n \tag{10}$$

where K is the strength coefficient, ϵ_0 is initial plastic strain and n is strain hardening coefficient. The parameters in Eq. (10) are given in Table 1.

Table 1. Swift parameters for AA2090-T3 [19]

K	ϵ_0	n
646	0.025	0.227

6.2. Finite Element Method

In the present work, cup drawing process of AA2090-T3 alloy was investigated. Information about tool geometry and dimensions can be found in the study [19].

The process was modelled by using Marc software. Full models of the parts were prepared to reflect anisotropy of the material. The blank was discretized by shell elements, full-integrated element formulation was selected and different number of through-thickness integration points were used to study the effect of the number of layers. Therefore, three different FE models were built and the blank was modeled with 5, 7 and 9 layers. FE model of the cup drawing process was shown in Figure 1. The tools were modeled as rigid bodies. The die was fixed in its initial position and the punch moved upwards according to position-time data table. 22.2 kN blank holder force was applied. Segment to segment contact algorithm was used for defining the contact and the friction coefficient between the parts was taken as 0.1.

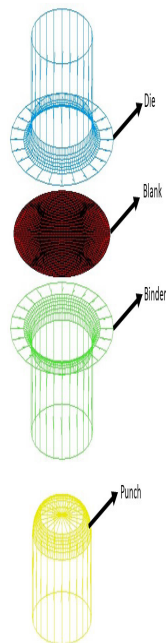


Figure 1. FE model of cylindrical cup deep drawing process

Required yield stress ratios for determination of Yld91 coefficients are given in Table 2. In Table 2, $\bar{\sigma}_\theta$ indicates the normalized yield stress along θ direction. In this study, yield stress in rolling direction (σ_0) was taken as reference yield stress in the determination of yield stress ratios (Eq 11). Yld91 coefficients were determined by solving the system

of nonlinear equations with N-R numerical method. Marc program takes yield stress ratios as input and calculates Yld91 coefficients with N-R numerical method. The determined Yld91 coefficients were given in Table 3.

$$\bar{\sigma}_\theta = \frac{\sigma_\theta}{\sigma_0} \tag{11}$$

Table 2. Yield stress ratios of AA2090-T3 in different directions and biaxial stress state [19]

Material	$\bar{\sigma}_0$	$\bar{\sigma}_{45}$	$\bar{\sigma}_{90}$	$\bar{\sigma}_b$
AA2090-T3	1.0000	0.8114	0.9102	1.0350

Table 3. Anisotropy parameters of Yld91 yield criterion for AA2090-T3

C_1	C_2	C_3	C_6
1.06746	0.855986	1.12964	1.29708

7. RESULTS AND DISCUSSION

FE analyses were carried out with different number of layers. The predicted earing profiles and thickness strain distributions were compared with measurements to evaluate the influence of number of through-thickness integration points on the results. Experimental cup heights and thickness strain distributions were taken from literature [19].

7.1. Comparison of Earing Profile

In the present section, the influence of number of integration points on the earing prediction were examined. Therefore, the computed earing profiles from FE simulations were compared with measurements [19]. The final configuration of a full drawn cup and comparisons were shown in Figure 2 and Figure 3, respectively.

Figure 2. Equivalent stress distribution on fully drawn cup

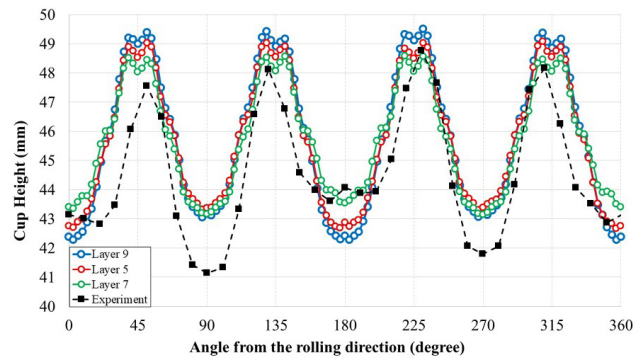


Figure 3. Computed and experimental cup heights [19]

It is seen from the Figure 3 that the earing profiles computed from simulations were similar and compatible with experiment, whereas the overall height predictions were different from each other. Cup height prediction of layer 7 was closer to the experiment than the other models at 135° and 315° from rolling direction, whereas the prediction of layer 5 was closer to the experimental data at 225° from rolling. Besides, it was observed that the cup height predictions of the models at 90°, 180° and 270° from rolling direction were incompatible with experimental results [19]. In addition to that it can be observed from the Figure 2 and 3 that four ears were predicted in the simulations, but six ears were observed in

the experiment. Extra two ears were observed along the rolling directions in the experiment [19]. This is due to the coefficient identification procedure of Yld91 criterion. This criterion is a stress based yield criterion and only it takes only yield stress ratios as input.

7.2. Comparison of Thickness Strains

Thickness strains predicted from the analyses were compared with measurements [19]. Comparisons of the calculated and experimental thickness strains in rolling and transverse directions were shown in Figure 4 and Figure 5, respectively.

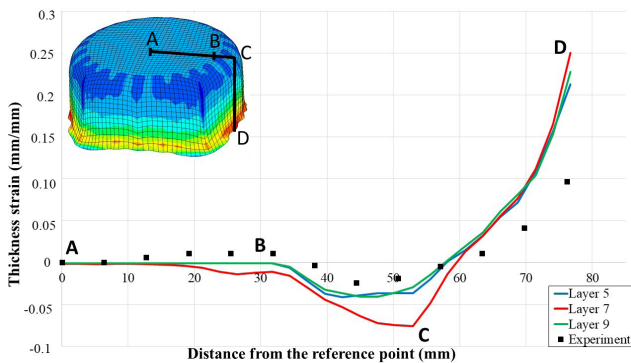


Figure 4. Computed and experimental thickness strains along the rolling direction [19]

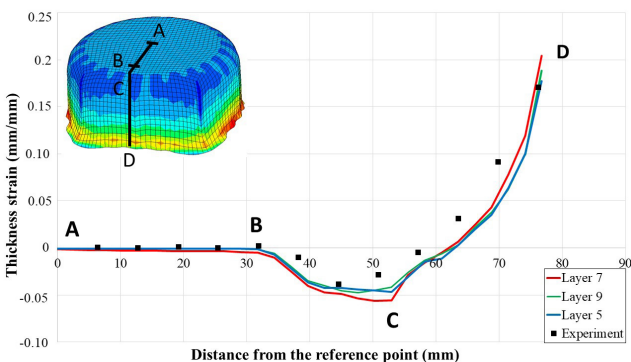


Figure 5. Computed and experimental thickness strains along the transverse direction [19]

It is seen from the Figure 4 and 5 that thickness strains along the rolling and transverse directions remained constant between reference point A and point B, then they decreased until point C and finally thickness strains continuously increased until point D. In both simulation and experiment, minimum and maximum thickness strains were observed on the corner region and the rim of the cup, respectively. This is an expected result, because both radial and tangential stresses occur on the corner region, whereas compressive stresses occur on the rim of the cup. Therefore, more thinning is observed on the corner region, while more thickening is observed on the rim of the part.

It is also could be observed from the Figure 4 and 5 that the differences of thickness strain between the FE simulation and experiment were small along rolling and transverse directions. Only, the predicted thickness strain from the layer 7 deviated from the experiment between 40 and 60 mm from the rolling direction.

8. CONCLUSIONS

Studies in the literature don't investigate the effect of through-thickness integration on the cup drawing simulations. In this study, the effect of this numerical parameter on the cup drawing simulation was studied. The anisotropic behavior of the material was defined with Yld91 yield criterion and implicit FE code Marc was used. Cup drawing simulations were performed with different layer numbers in order to investigate the effect of layer number through the thickness.

Conclusions drawn from this study are summarized in below:

1. Yld91 yield criterion could sufficiently define the anisotropic behavior of AA2090-T3 alloy
2. The computed earing profiles and thickness strain distributions from the simulations were compatible with the experiment.
3. Positioning of the ears on the drawn cup could be accurately predicted by Yld91 yield criterion. However differences between predicted and experimental cup heights were observed.
4. Layer number through the thickness from numerical parameters has a strong effect on the predicted maximum cup heights.

REFERENCES

- [1] Miller, W.S., Zhuang, L., Bottema, J., Wittebrood, A.J., De Smet, P., Haszler, A., Vieregge, A. (2000). Recent development in aluminum alloys for the automotive industry. *Materials Science and Engineering A*, 280(1): 37-49, DOI: 10.1016/S0921-5093(99)00653-X.
- [2] Hill, R. (1948). A theory of the yielding and plastic flow of anisotropic metals. *Proceedings of the Royal Society of London Series A Mathematical and Physical Sciences*, 193: 281-297, DOI: 10.1098/rspa.1948.0045.
- [3] Woodthorpe, J., Pearce, R. (1970). The anomalous behavior of aluminium sheet under balanced biaxial tension. *International Journal of Mechanical Sciences*, 12(4): 341-347, DOI: 10.1016/0020-7403(70)90087-1.
- [4] Hill, R. (1979). Theoretical plasticity of textured aggregates. *Mathematical Proceedings of the Cambridge Philosophical Society*, 85: 179-191, DOI: 10.1017/S0305004100055596.
- [5] Hill, R. (1990). Constitutive modelling of orthotropic plasticity in sheet metals. *Journal of the Mechanics and Physics of Solids*, 38(3): 405-417, DOI: 10.1016/0022-5096(90)90006-P
- [6] Barlat, F., Lian, K. (1989). Plastic behavior and stretchability of sheet metals. Part I: A yield function for orthotropic sheets under plane stress conditions. *International Journal of Plasticity*, 5(1): 51-66, DOI: 10.1016/0749-6419(89)90019-3.
- [7] Barlat, F., Lege, D.J., Brem, J.C. (1991). A six-component yield function for anisotropic materials. *International Journal of Plasticity*, 7(7): 693-712, DOI: 10.1016/0749-6419(91)90052-Z.
- [8] Barlat, F., Maeda, Y., Chung, K., Yanagawa, M., Brem, J.C., Hayashida, Y., Lege, D.J., Matsui, K., Murtha, S.J., Hattori, S., Becker, R.C., Makosey, S. (1997). Yield function development for aluminum alloy sheets. *Journal of the Mechanics and Physics of Solids*, 45(11-12): 1727-1763, DOI: 10.1016/S0022-5096(97)00034-3

- [9] Barlat, F., Brem, J.C., Yoon, J.W., Chung, K., Dick, R.E., Lege, D.J., Pourboghra, F., Choi, S.-H., Chu, E. (2003). Plane stress yield function for aluminum alloy sheets-part 1: theory. *International Journal of Plasticity*, 19: 1297-1319, DOI: 10.1016/S0749-6419(02)00019-0.
- [10] Barlat, F., Aretz, H., Yoon, J.W., Karabin, M.E., Brem, J.C., Dick, R.E. (2005). Linear transformation-based anisotropic yield functions. *International Journal of Plasticity*, 21: 1009-1039, DOI: 10.1016/j.ijplas.2004.06.004.
- [11] Chung, K., Shah, K. (1992). Finite element simulation of sheet metal forming for planar anisotropic metals. *International Journal of Plasticity*, 8(4): 453-476, DOI: 10.1016/0749-6419(92)90059-L.
- [12] Yoon, J.W., Song, I.S., Yang, D.Y., Chung, K., Barlat, F. (1995). Finite element method for sheet forming based on an anisotropic strain-rate potential and the convected coordinate system. *International Journal of Mechanical Sciences*, 37(7): 733-752, DOI: 10.1016/0020-7403(95)00003-G.
- [13] Chung, K., Lee, S.Y., Barlat, F., Keum, Y.T., Park, J.M. (1996). Finite element simulation of sheet forming based on a planar anisotropic strain-rate potential. *International Journal of Plasticity*, 12(1), 93-115, DOI: 10.1016/S0749-6419(95)00046-1.
- [14] Yoon, J.W., Yang, D.Y., Chung, K. (1999). Elasto-plastic finite element method based on incremental deformation theory and continuum based shell elements for planar anisotropic sheet materials. *Computer Methods in Applied Mechanics and Engineering*, 174(1-2), 23-56, DOI: 10.1016/S0045-7825(98)00275-8.
- [15] Parente, M.P.L., Valente, R.A.F., Jorge, R.M.N., Cardoso, R.P.R., De Sousa, R.J.A. (2006). Sheet metal forming simulation using EAS solid-shell finite elements. *Finite Elements in Analysis and Design*, 42(13), 1137-1149, DOI: 10.1016/j.finel.2006.04.005.
- [16] Yoon, J.W., Barlat, F., Dick, R.E., Karabin, M.E. (2006). Prediction of six or eight ears in a drawn cup based on a new anisotropic yield function. *International Journal of Plasticity*, 22, 174-193, DOI: 10.1016/j.ijplas.2005.03.013.
- [17] Younas, N., Chalal, H., Abed-Meraim, F. (2020). Finite element simulation of sheet metal forming processes using non-quadratic anisotropic plasticity models and solid-shell finite elements. *Procedia Manufacturing*, 47, 1416-1423, DOI: 10.1016/j.promfg.2020.04.302.
- [18] Banabic, D. (2010). *Sheet Metal Forming Processes Constitutive Modelling and Numerical Simulation*. Springer-Verlag, Berlin.
- [19] Yoon, J.W., Barlat, F., Chung, K., Pourboghra, F., Yang, D.Y. (2000). Earing predictions based on asymmetric nonquadratic yield function. *International Journal of Plasticity*, 16(9), 1075-1104, DOI: 10.1016/S0749-6419(99)00086-8.



A Numerical Investigation of The Fracture Energy of Materials for Fuel Cell End Plates

Adem Avcu* , Naghdali Choupani , Gökhan Tüccar 

Mechanical Engineering Department /Faculty of Engineering /Adana Alparslan Türkeş Science and Technology University /Adana, Turkey

Abstract

Nowadays, with increasing energy requirements, the use of clean energy resources has become important. Fuel cells are an important key for clean energy technology due to wide range of utilization areas such as automotive, portable power applications, electricity generation, space, aviation and naval technologies. Additionally, they have many significant properties such as not producing harmful gases, therefore they do not cause environmental and chemical pollution. Besides, they have not any moving parts, also they do not produce noise. By comparison to fossil fuel, fuel cells have high efficiency that reaches up to 60% in appropriate conditions. Proton Exchange Membrane Fuel Cell (PEMFC) has many advantages than other fuel cell types due to simple structure, higher efficiency and low operating temperature. PEMFC may consist of one or more stacks to generate more electricity. End plate of PEMFC holds together all parts of it. Therefore, the material selection for end plate is important to provide safe conditions. To use PEMFC safely, investigation of material fracture energy is required to decide that the material is in safe conditions or not. There are three fracture energy modes which are mode I, mode II and mode III. There are many methods to investigate failure of material at different modes. Unlike other methods, Arcan specimen gives facility to evaluate of mode I, mode II and mixed modes. The main purpose of this paper was to compare the results of fracture energy (strain energy release rate) of different materials for end plates in fuel cells. Another goal was to select a suitable material was selected as PEMFC end plate.

Keywords: PEMFC, End plate, Fracture energy, Strain energy release rate.

9. INTRODUCTION

Fossil fuels are used for energy procurement widely, so environmental pollution rises due to harmful gases release. The usage of clean energy sources has started to increase in order to prevent environmental pollution. For this reason, fuel cells have seen as a significant option among clean energy sources with its positive sides. Besides, research and development on fuel cells have become important issue. There are advantages of fuel cell's properties such as, being environmentally and friendly, not producing harmful gases, high efficiency, noiseless, no moving parts and therefore low maintenance required. At First, fuel cells were used in space and marine technology, usage of them has started to become more widespread with the great advances in fuel cells [1, 2].

Fuel cells are devices that convert chemical energy to electrical energy directly. They generally produce electricity and water by the reaction of Hydrogen and Oxygen. As a result of chemical reaction, they do not create harmful waste for the environment. Only water and heat are produced after

chemical reaction, it is the most important feature of fuel cells in energy production [2-5].

Generally, fuel cells are classified as Alkaline Fuel Cell (AFC), Direct Methanol Fuel Cell (DMFC), Proton Exchange Membrane Fuel Cell (PEMFC), Phosphoric Acid Fuel Cell (PAFC), Molten Carbonate Fuel Cell (MCFC) and Solid Oxide Fuel Cell (SOFC). Each of them has advantages with their specific features according to usage areas. PEMFC is used more widely today than other fuel cells. With its high voltage, current and power density, low pressure operation, corrosion-resistant electrolyte usage, tolerance to pressure change, simple structure, low temperature operation, portable usage, it is more accurate choice than the other fuel cells with its advantages [2, 6, 7].

Metal, non-metal and composite materials are used as material of end plates in fuel cells. Composite materials are also preferred in fuel cells due to their light weight, corrosion resistance and high mechanical properties [8]. There are studies with composite on bipolar flow plates and end plate

* Corresponding author
Email: ademavcu01@gmail.com



plates. However, there are many studies on bipolar flow plates, few studies on end plates [9-12].

Fracture energy is an important case to decide safe conditions of material. When different loads are applied to specimen, it is significant to determine what kind of breakage may occur. There are three fracture modes which are mode I (opening), mode II (sliding shear) and mode III (tearing) [13]. These modes are evaluated by using methods for mode I Double Cantilever Beam (DCB), for mode II End Notched Flexure (ENF), for mode III Crack Rail Shear (CRS) and Asymmetric Double Cantilever Beam (ADCB), Asymmetric Tapered Double Cantilever Beam (ATDCB), Crack Lap Shear (CLS) and Single Leg Bending (SLB) methods are used to calculate fracture energy of material. To compute fracture energy of mixed mode which is combining load form of mode I and mode II, different methods are required. The use of different test cases can lead to difficult test conditions and results. To carry out mixed mode conditions to test material, Arcan specimen is efficient due to facility observation of different mixed modes [14-16].

In this study, numerical analysis of fracture energy for different materials was compared for selected end plate of PEMFC. Strain energy release rates were calculated numerically by using Arcan specimen for mode I, mode II and mixed modes. To decide appropriate material for PEMFC end plate, the fracture energy results were compared for wide range of material system.

10. DESCRIPTION OF SET-UP

Fuel cells are devices that convert chemical energy to electrical energy directly. PEMFC is common type fuel cell and it contains membrane, gas diffusion layer (GDL), catalyst layer (CL), bipolar flow plate (BFP) or bipolar plate and end plate. Membrane, GDL and CL are joined together to form a membrane electrode assembly (MEA). Parts of PEMFC are shown in Figure 1. A single fuel cell consists of a MEA and two BFP producing about 1.2 V [17]. This assembly of cell is called a fuel cell stacks. For more voltage, more cells are stacked [18]. Stacks are clamped between two end plates to hold them together [10, 19].

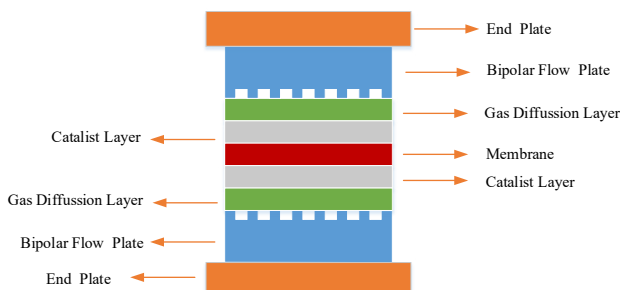


Figure 1. Parts of PEMFC

In PEMFC fuel cells, an end plate is used to hold the stacks together. Generally end plates have to be possessed of low density, electrochemical stability, high mechanical strength and stiffness and electrical insulation. So, metal, non-metals and composites materials can be used as fuel cell end plate

[19-21]. End plate materials are used with different thickness and design by changing their material properties. Yu et. al. [10] determined size of composite plate as given in Figure 2. Besides they set down thickness of composite material as 10 mm for stainless steel and 15 mm for composite material.

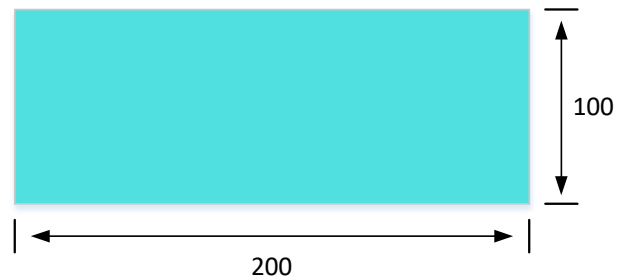


Figure 2. Size of end plate

Fuel cell stacks are combined with end plates, so it has to have high flexural stiffness to keep together all parts in ideal conditions. If there is too much contact pressure, this condition can compress gas diffusion layer (GDL) and can change GDL porosity. Besides, gas and water flow will not transfer from PEMFC flow channels sufficiently. However, if there is little contact pressure, this can cause high contact resistance between back of GDL and bipolar flow plates (BFP) that can reduce performance of fuel cell. Hence, PEMFC end plate should high flexural stiffness. If it has low flexural stiffness, it may yield a non-uniform contact pressure in the whole plate as given in Figure 3 [10].

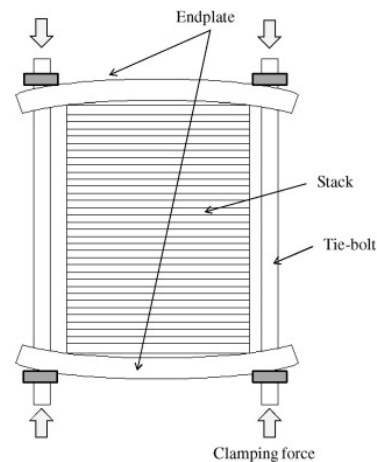


Figure 3. Deflection of PEMFC End Plate [10]

Composite materials are combined with two or more components therefore they may have different mechanical properties at each direction. When different loads are applied to specimen by varying angles, it is important to determine what kind of failure may occur. Also, fracture energy is important in order to decide safe conditions of material [13, 22].

11. THEORITICAL BACKGROUND

The fracture energy of material is investigated by using linear elastic fracture mechanics which is used to calculate the strain energy release rate at the crack tip [23]. It is a useful tool for composite material cracks when the specimen is orthotropic material [15]. The Generalized Hooke's law is

given in the following equation [24, 25].

$$\begin{pmatrix} \epsilon_x \\ \epsilon_y \\ \epsilon_z \\ \gamma_{yz} \\ \gamma_{xz} \\ \gamma_{xy} \end{pmatrix} = \begin{pmatrix} a_{11} & a_{12} & a_{13} & a_{14} & a_{15} & a_{16} \\ a_{21} & a_{22} & a_{23} & a_{24} & a_{25} & a_{26} \\ a_{31} & a_{32} & a_{33} & a_{34} & a_{35} & a_{36} \\ a_{41} & a_{42} & a_{43} & a_{44} & a_{45} & a_{46} \\ a_{51} & a_{52} & a_{53} & a_{54} & a_{55} & a_{56} \\ a_{61} & a_{62} & a_{63} & a_{64} & a_{65} & a_{66} \end{pmatrix} \begin{pmatrix} \sigma_x \\ \sigma_y \\ \sigma_z \\ \tau_{yz} \\ \tau_{xz} \\ \tau_{xy} \end{pmatrix} \quad (1)$$

Expressions of letters are strain (ϵ), normal stress (σ), shear stress (τ), shearing strain (γ) and constants (a_{ij}). Elastic constants are given as the following relationships.

$$\begin{aligned} a_{11} &= \frac{1}{E_x} & a_{22} &= \frac{1}{E_y} & a_{33} &= \frac{1}{E_z} \\ a_{44} &= \frac{1}{G_{yz}} & a_{55} &= \frac{1}{G_{xz}} & a_{66} &= \frac{1}{G_{xy}} & a_{12} &= a_{21} = -\frac{\nu_{xy}}{E_x} = -\frac{\nu_{yx}}{E_y} \\ a_{13} &= a_{31} = -\frac{\nu_{xz}}{E_x} = -\frac{\nu_{zx}}{E_z} & a_{23} &= a_{32} = -\frac{\nu_{yz}}{E_y} = -\frac{\nu_{zy}}{E_z} \end{aligned} \quad (2)$$

Where E_x, E_y, E_z are elastic modulus in direction of x, y, z. G_{xy}, G_{yz}, G_{xz} are shear modulus in each plane and $\nu_{xy}, \nu_{yx}, \nu_{yz}$ are Poisson's ratio.

In case of a thin plate, principal axes are in xy plane and assuming conditions are given as:

$$\sigma_z = \tau_{yz} = \tau_{xz} = 0 \quad (3)$$

If the Eq. (3) assumptions are written in Eq. (1), then equation is turned into Eq. (4).

$$\begin{pmatrix} \hat{\alpha}_x \\ \hat{\alpha}_y \\ \gamma_{xy} \end{pmatrix} = \begin{pmatrix} a_{11} & a_{12} & a_{16} \\ a_{12} & a_{22} & a_{26} \\ a_{16} & a_{26} & a_{66} \end{pmatrix} \begin{pmatrix} \sigma_x \\ \sigma_y \\ \tau_{xy} \end{pmatrix} \quad (4)$$

Where $\sigma_x, \sigma_y, \tau_{xy}$ are plane stresses and $\epsilon_x, \epsilon_y, \gamma_{xy}$ are plane strains.

The another assumptions are given in Eq. (5)

$$\epsilon_z = \gamma_{yz} = \gamma_{xz} = 0 \quad (5)$$

$$\sigma_z = \frac{-(a_{13}\sigma_x + a_{23}\sigma_y + a_{13}\tau_{xy})}{a_{33}} \quad (6)$$

$$\begin{pmatrix} \hat{\alpha}_x \\ \hat{\alpha}_y \\ \gamma_{xy} \end{pmatrix} = \begin{pmatrix} b_{11} & b_{12} & b_{16} \\ b_{12} & b_{22} & b_{26} \\ b_{16} & b_{26} & b_{66} \end{pmatrix} \begin{pmatrix} \sigma_x \\ \sigma_y \\ \tau_{xy} \end{pmatrix} \quad (7)$$

Where the terms of constants b_{ij} are defined in terms of the following nonzero entries a_{ij} of the compliance matrix:

$$b_{ij} = a_{ij} - \frac{a_{i3}a_{j3}}{a_{33}} \quad (i, j=1, 2, 4, 5, 6) \quad (8)$$

$$a_{16} = a_{26} = a_{36} = a_{45} = 0, \quad b_{16} = b_{26} = 0,$$

$$b_{11} = \frac{a_{11}a_{33} - a_{13}^2}{a_{33}}, \quad b_{12} = \frac{a_{12}a_{33} - a_{13}a_{23}}{a_{33}},$$

$$b_{22} = \frac{a_{22}a_{33} - a_{23}^2}{a_{33}}, \quad b_{66} = \frac{a_{66}a_{33} - a_{36}^2}{a_{33}} \quad (9)$$

The strain energy release rates are calculated by Eq. (10). Where G_I and G_{II} are mode I and mode II strain energy release rates, E_I and E_{II} effective moduli, K_I and K_{II} are mode I

and mode II stress intensity factors, respectively.

$$G_I = \frac{K_I^2}{E_I}, \quad G_{II} = \frac{K_{II}^2}{E_{II}} \quad (10)$$

$$E_I = \sqrt{\frac{2}{a_{11}a_{22}}} \frac{1}{\sqrt{\left(\left(\sqrt{\frac{a_{22}}{a_{11}}}\right) + \frac{2a_{12} + a_{66}}{2a_{11}}\right)}}$$

$$E_{II} = \frac{\sqrt{2}}{a_{11}} \frac{1}{\sqrt{\left(\left(\sqrt{\frac{a_{22}}{a_{11}}}\right) + \frac{2a_{12} + a_{66}}{2a_{11}}\right)}} \quad (\text{for plane stress});$$

$$E_I = \sqrt{\frac{2}{b_{11}b_{22}}} \frac{1}{\sqrt{\left(\left(\sqrt{\frac{b_{22}}{b_{11}}}\right) + \frac{2b_{12} + b_{66}}{2b_{11}}\right)}}$$

$$E_{II} = \frac{\sqrt{2}}{b_{11}} \frac{1}{\sqrt{\left(\left(\sqrt{\frac{b_{22}}{b_{11}}}\right) + \frac{2b_{12} + b_{66}}{2b_{11}}\right)}} \quad (\text{for plane strain}) \quad (11)$$

12. FINITE ELEMENT MODELING OF MIXED MODE FRACTURE

Finite element analysis was carried out by using J-integral method for numerical calculation. Arcan specimen is applied constant 1000 N load by using Abaqus. Arcan Specimen modelling in Abaqus is shown in Figure 4. The model was created using eight nodes and collapsed elements of the model (CPE8RH). The mesh was focused around the crack tip, and linear elastic finite element analysis was performed under the plane strain conditions.

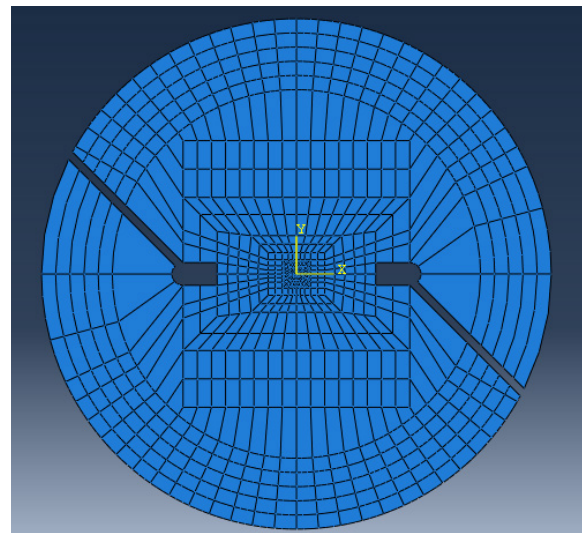


Figure 4. Arcan Specimen modelling in Abaqus

Fracture behaviors of selected materials were investigated numerically by using 2D arcan specimen under different loading conditions. The typical loading angles of mode I (0°), mixed mode (45°) and mode II (90°) are shown in Figure 5.

Composite materials show distinct characteristics in each direction, but metal and ceramic materials have the same properties due to homogeneous structure. Therefore, all materials have different properties so they give different strain energy release rate results under mode I, mode II and

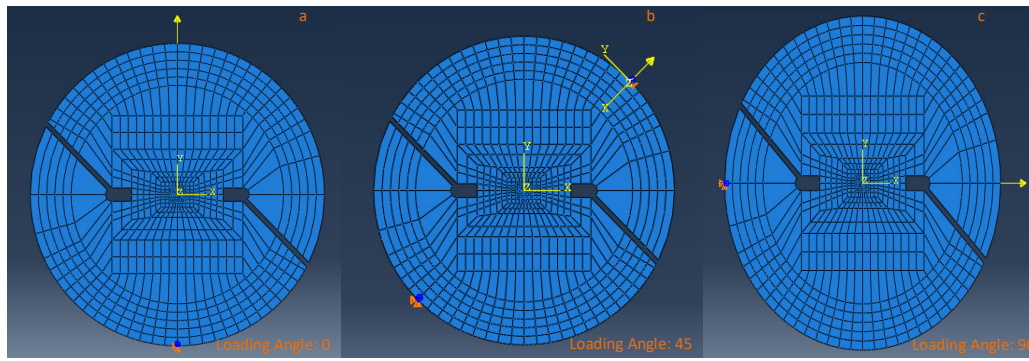


Figure 5. Arcan specimen under different loading angle, (a) mode I loading condition, (b) mixed mode loading condition and (c) mode II loading condition

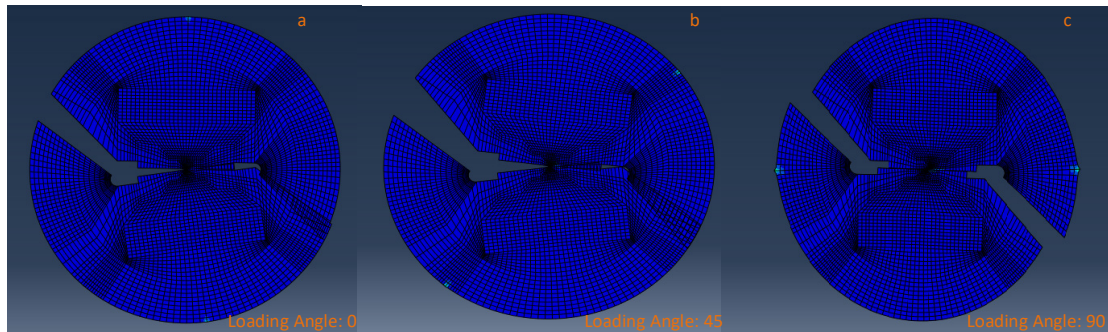


Figure 6. Arcan specimen numerical deformation results, (a) mode I fracture result, (b) mixed mode fracture result and (c) mode II fracture result

Table 1. Elastic property of materials under investigation.

Material	E_1 [GPa]	E_2 [GPa]	E_3 [GPa]	G_{12} [GPa]	G_{13} [GPa]	G_{23} [GPa]	ν_{12}	ν_{13}	ν_{23}
Steel [28]	207	207	207	79.6	79.6	79.6	0.30	0.30	0.30
Titanium [29]	110	110	110	42	42	42	0.31	0.31	0.31
Aluminum [28]	72	72	72	27	27	27	0.33	0.33	0.33
Boron-epoxy [29]	193.06	18.62	18.62	5.52	5.52	7.76	0.21	0.21	0.2
UD Gr-epoxy [29]	132.7	8.83	8.83	4.76	4.76	3.40	0.36	0.36	0.30
CP Gr-epoxy [29]	71.2	71.2	8.83	4.76	4.0	4.0	0.04	0.32	0.32
Kevlar-KM2 [35]	84	1.34	1.34	24.4	24.4	0.54	0.0095	0.0095	0.24
Glass-Polyester [27]	47.92	13.94	13.94	5.21	5.21	20.9	0.27	0.27	0.33
CFRP [26]	138	10	10	6	6	3.7	0.27	0.27	0.45
Aluminum6061 [34]	68.9	68.9	68.9	25.9	25.9	25.9	0.33	0.33	0.33
AlSiC [30]	150	150	150	57.7	57.7	57.7	0.3	0.3	0.3
T300 [31]	135	9.26	9.26	6.15	6.15	3.07	0.32	0.32	0.51
Ceramic [32]	96	96	96	37.2	37.2	37.2	0.29	0.29	0.29
GFRP [33]	31.22	31.62	24.61	9.05	9.25	9.31	0.22	0.30	0.24

mixed loading conditions. Arcan Specimen numerical deformation results are given in Figure 6. It can be seen that the material undergoes different deformation in each mode.

13. RESULTS AND DISCUSSION

In this study, the values of strain energy release rates for mode I, mode II, and mixed mode were obtained by using 2D Arcan specimen model by changing loading angles. Constant value of the load 1000 N is applied to different materials in order to compare the results and investigate the loading angle variations of fracture energy parameters. The end plate should be assembled with ideal clamping pressure. That can be affected performance of PEMFC parts. Particularly, MEA performance depends on change of clamping pressure. Therefore, PEMFC efficiency is affected from changing the clamping pressure. The end plate provides de-

sired working conditions so decision of convenient material is significant. Besides, the end plate should have low density, electrochemical stability, high rigidity, insulating property and corrosion resistance [20, 21].

Generally metals, non-metals and composite materials can be used as fuel cell end plate [19, 20]. In this study, steel, titanium, aluminum, boron-epoxy, UD graphite-epoxy, CP graphite-epoxy, kevlar-KM2, glass-polyester, CFRP (Carbon Fiber Reinforced Polymer), aluminum6061, AlSiC (Aluminum Silicon Carbide), T300 (T300/976 UD tape), ceramic and GFRP (Glass Fiber Reinforced Polymer) are selected as end plate of PEMFC material system. The elastic properties of all materials used in numerical analysis are listed in the Table 1 [26-35]. In this paper, strain energy release rate of the 14 different materials were investigated by numerical analysis of Arcan specimen. Additionally, their fractu-

re energy were obtained in order to make decision about the most appropriate material as end plate. To obtain strain energy release rates of materials, 1000 N load is applied at pure mode I, mixed mode with 15° intervals and pure mode II conditions.

Values of mode I strain energy release rates versus loading angle for various materials are shown in Table 2 and Figure 7. As it can be seen, for all materials used in this investigation the mode I fracture energy decreases as the mode II loading contribution increases. The mode I fracture energy has the maximum value for the Kevlar-KM2 and the minimum value for the steel among the studied materials under all loading angle conditions.

Table 2. Mode I fracture energy G_I (J/m²) for various materials under different loading angles.

Material	Loading angle (Degrees)						
	0°	15°	30°	45°	60°	75°	90°
Kevlar-KM2	528.92	493.31	396.58	264.27	132.13	35.40	0
UD Graphite-epoxy	227.02	211.80	170.28	113.57	56.76	15.21	0
CFRP	179.47	167.50	134.66	89.76	44.88	12.03	0
T300	176.70	164.86	132.52	88.39	44.18	11.84	0
Glass-Polyester	174.75	163.08	131.09	87.39	43.69	11.70	0
Boron-epoxy	144.63	134.97	108.51	72.35	36.18	9.70	0
GFRP	92.63	86.40	69.47	46.31	23.15	6.20	0
CP Graphite-epoxy	82.37	76.86	61.79	41.19	20.59	5.51	0
Aluminum6061	35.77	33.41	26.86	17.92	8.97	2.40	0
Aluminum	34.27	31.98	25.72	17.15	8.58	2.30	0
Ceramic	26.46	24.69	19.85	13.25	6.63	1.78	0
Titanium	22.81	21.28	17.22	11.42	5.72	1.53	0
AlSiC	16.88	15.75	12.67	8.45	4.23	1.13	0
Steel	12.27	11.45	9.21	6.15	3.08	0.82	0

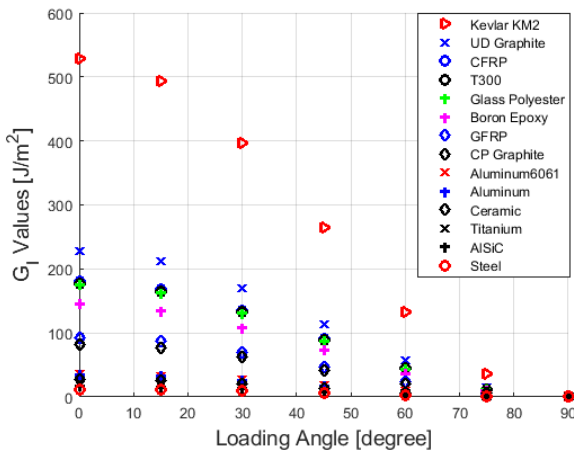


Figure 7. G_I fracture energy versus loading angle graph.

Table 3 and Figure 8 show the mode II fracture energy of the materials system under study. It reveals that the mode II fracture energy has its highest value at 90 degrees loading angle and increases as the mode II loading contribution increases for all investigated materials. For all materials under study in this investigation, Glass-Polyester has the highest G_{II} fracture energy value; on the other hand the G_{II} value of steel has the lowest among the materials.

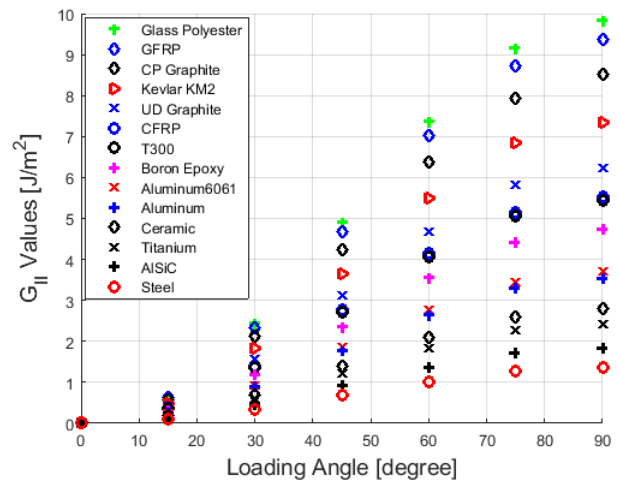


Figure 8. G_{II} fracture energy versus loading angle graph

Table 3. Mode II fracture energy G_{II} (J/m²) for various materials under different loading angles.

Material	Loading angle (Degrees)						
	0°	15°	30°	45°	60°	75°	90°
Glass-Polyester	0	0.66	2.46	4.92	7.38	9.18	9.83
GFRP	0	0.63	2.34	4.68	7.02	8.72	9.36
CP Graphite-epoxy	0	0.57	2.12	4.25	6.37	7.93	8.52
Kevlar-KM2	0	0.48	1.83	3.66	5.50	6.84	7.34
UD Graphite-epoxy	0	0.42	1.56	3.12	4.68	5.81	6.23
CFRP	0	0.37	1.38	2.77	4.15	5.15	5.53
T300	0	0.36	1.36	2.71	4.07	5.07	5.43
Boron-epoxy	0	0.32	1.18	2.37	3.56	4.42	4.73
Aluminum6061	0	0.25	0.93	1.85	2.77	3.45	3.70
Aluminum	0	0.24	0.89	1.78	2.66	3.31	3.55
Ceramic	0	0.19	0.70	1.40	2.09	2.60	2.79
Titanium	0	0.16	0.61	1.21	1.82	2.26	2.42
AlSiC	0	0.12	0.46	0.92	1.37	1.71	1.83
Steel	0	0.14	0.34	0.68	1.02	1.27	1.36

The total strain energy release rates obtained by $G_T = G_I + G_{II}$ in different loading angles are shown for the all materials in Table 4 and Figure 9. Total strain energy release under mixed-mode loading conditions changes with the loading angle. In pure mode I loading angle, they have the highest G_T value for all materials. As loading angle increases towards mode II conditions its value decreases. As compared for all the materials, Kevlar-KM2 has the highest G_T value in pure mode I, pure mode II and all mixed mode conditions. On the other hand, G_T of steel has the lowest value among all material in mode I, mode II and mixed mode loadings.

Table 5 summarizes the fracture energy values of the mode I (G_I), the mode II (G_{II}), the total (G_T), the fracture toughness (G_{IC}), and the ratio (G_{IC}/G_I) for all materials system under investigation in this study. The fracture toughness values of the materials are obtained from the literature. It can be seen that values of G_I and G_T of kevlar-KM2 are higher among the other materials. However, aluminum has the highest value of G_{IC} among all the materials in the table. Furthermore, G_{II} of glass-polyester has the highest value among the materials. Meanwhile, the fracture energy ratio (G_{IC}/G_I) of steel is supreme among the selected metallic materials so it is the best choice when other criteria like density are not

Table 4. Total fracture energy G_T (J/m²) for various materials under different loading angles.

Material	Loading angle (Degrees)						
	0°	15°	30°	45°	60°	75°	90°
Kevlar-KM2	528.92	493.79	398.41	267.93	137.63	42.24	7.34
UD Graphite-epoxy	227.02	212.22	171.84	116.69	61.44	21.02	6.23
CFRP	179.47	167.87	136.04	92.53	49.03	17.18	5.53
T300	176.67	165.22	133.88	91.10	48.25	16.91	5.43
Glass-Polyester	174.75	163.74	133.55	92.31	51.07	20.89	9.83
Boron-epoxy	144.63	135.29	109.69	74.72	39.74	14.12	4.73
GFRP	92.63	87.03	71.81	50.99	30.17	14.92	9.36
CP Graphite-epoxy	82.37	77.43	63.91	45.44	26.97	13.44	8.52
Aluminum6061	35.79	33.66	27.79	19.77	11.74	5.85	3.70
Aluminum	34.27	32.22	26.61	18.93	11.24	5.61	3.55
Ceramic	26.46	24.88	20.55	14.65	8.72	4.38	2.79
Titanium	22.81	21.44	17.83	12.63	7.54	3.79	2.42
AlSiC	16.88	15.87	13.13	9.37	5.60	2.84	1.83
Steel	12.27	11.59	9.55	6.83	4.1	2.09	1.36

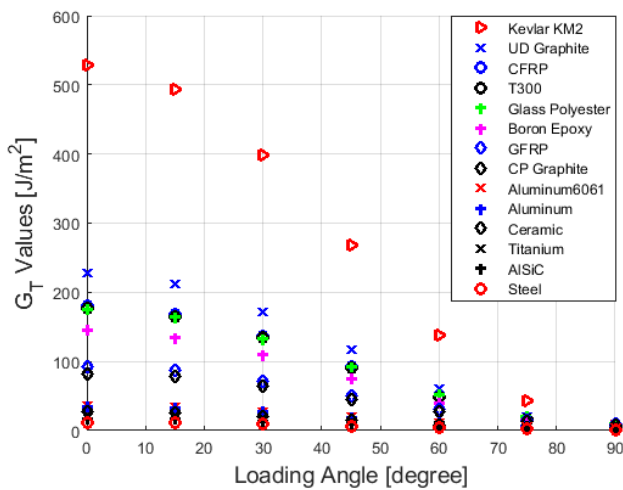


Figure 9. G_T fracture energy versus loading angle graph.

Table 5. Strain energy release rates versus fracture toughness properties.

Material	G_I	G_{II}	G_T	G_{IC}	G_{IC}/G_I
Steel	12.27	1.36	13.63	9835 [38]	801.55
Titanium	22.81	2.42	25.23	12180 [38]	533.86
Aluminum	34.27	3.54	37.81	14391 [38]	420.00
Aluminum6061	35.77	3.70	39.47	10877[34]	304.08
AlSiC	16.88	1.83	18.71	480.54 [40]	28.47
CP Graphite-epoxy	82.37	8.52	90.89	1500 [25]	18.21
Kevlar-KM2	528.92	7.34	536.26	8717.7 [35]	16.48
GFRP	92.63	9.36	101.99	1440 [33]	15.54
Ceramic	26.46	2.79	29.25	152 [41]	5.74
UD Graphite-epoxy	227.02	6.23	233.25	800 [39]	3.52
Glass-Polyester	174.75	9.83	184.58	496 [42]	2.84
CFRP	179.47	5.53	185.00	436 [26]	2.43
Boron-epoxy	144.63	4.73	149.36	328 [43]	2.27
T300	176.70	5.43	182.13	165 [44]	0.93

considered. Additionally, other parameters like density of material should be considered in order to consider for proper material selection of end plate. Composite materials with the advantage of strength and hardness along with lightness have proven their use through many applications in various fields. In this investigation, CP graphite-epoxy, kevlar-KM2 and GFRP with densities of 1.60 g/cc, 1.45 g/cc and 2.20 g/cc, respectively [35-37], were found to ensure the maximum

value of G_{IC}/G_I among studied composite materials. In this study, a numerical attempt was made to explain some of the important issues related to the fracture energy of the selected material used in the end plates of the fuel cell. Due to the importance of the issue, there is still significant activity in this area. Therefore, some future research in this area may be required to perform parallel design exercises using numerical and experimental fracture approaches on commonly used materials as end plate material.

14. CONCLUSION

In this paper, PEMFC end plates materials and their strain energy release rates were investigated by numerical analysis of Arcan specimen under different loading conditions. Firstly, stress intensity factors are obtained for each material by finite element analyzing Arcan specimen using Abaqus package program finite element and fracture energy of materials in mode I, mode II and mixed mode conditions were calculated. According to the results, for loading angles close to mode I condition, mode I fracture was dominant. For loading angles close to mode II condition, mode II strain energy release rates became dominant. Besides, it was concluded that the total strain energy release rate under mixed mode loading conditions decreases with the increasing loading angle. Among the studied metals, steel, titanium and aluminum were found to have superior fracture energy values. Various applications of composite materials in primary and secondary structures have made them as a suitable alternative to metal materials. Composite materials with strength and stiffness combined with lightness have proven their application through many applications in various fields. Due to their importance in engineering applications, in this investigation, CP graphite-epoxy, kevlar-KM2 and GFRP were confirmed to warrant the appropriate fracture resistance among studied composite materials. Kevlar-KM2 has lower density and higher fracture toughness values than CP graphite-epoxy and GFRP. Therefore, kevlar-KM2 was found as an appropriate composite material for PEMFC end plate by considering fracture energy and density of the material parameters.

REFERENCES

- [1] Bayrak Z.U., Gençoğlu M.T. (27-30 June 2010) Mathematical Models of PEM Fuel Cells 5th International Ege Energy Symposium and Exhibition (IEESE-5) Pamukkale University, Denizli, Turkey
- [2] Giorgi, L., Leccese, F. (2013). Fuel cells: technologies and applications. The Open Fuel Cells Journal, 6(1) DOI: 10.2174/1875932720130719001
- [3] Scott K., Shukla A.K. (2004) Polymer electrolyte membrane fuel cells: Principles and advances Reviews in Environmental Science & Bio-Technology (2004) 3: 273–280
- [4] Vishnyakov V.M. (2006) Proton Exchange Membrane Fuel Cells Vacuum 80 doi:10.1016/j.vacuum.2006.03.029
- [5] Habibi A., Mousavi N., Mohammadi M., Farahmand S. (2019). The Performance of Types of Fuel Cell: Energy Generation International Journal of Engineering Science and Application, 3(3)

- [6] Dhand A., Suresh S., Jain A., O N.V. Kerawalla M.A.K., Goswami P. (2017) Advances in Materials for Fuel Cell Technologies-A Review International Journal for Research in Applied Science & Engineering Technology (IJRASET) ISSN: 2321-9653; IC Value: 45.98; SJ Impact Factor:6.887 Volume 5 Issue IX, September 2017
- [7] Perry, M. L., & Fuller, T. F. (2002). A historical perspective of fuel cell technology in the 20th century. *Journal of the electrochemical society*, 149(7), S59
- [8] Baroutaji A., Carton J.G., Sajjia M., Olabi A.G. (October 2015) Materials in PEM Fuel Cells Materials Science and Materials Engineering DOI: 10.1016/B978-0-12-803581-8.04006-6
- [9] Tamilarasan U., Karunamoorthy L., Palanikumar K. (2015) Mechanical Properties Evaluation of the Carbon Fibre Reinforced Aluminium Sandwich Composites Materials Research DOI: <http://dx.doi.org/10.1590/1516-1439.017215>
- [10] Yu H.N., Kim S.S., Suh J. D., Lee D.G. (2010) Composite endplates with pre-curvature for PEMFC (polymer electrolyte membrane fuel cell) Composite Structures doi:10.1016/j.compstruct.2009.10.023
- [11] Hermann A., Chaudhuri T., Spagnol P. (2005) Bipolar Plates for PEM fuel cells: A review International Journal of Hydrogen Energy 30 (2005) 1297 – 1302 doi:10.1016/j.ijhydene.2005.04.016
- [12] Wilberforce T., El Hassan Z., Ogungbemi E., Jacob O., Khabiri Durrant A., Thompson J., Baroutaji A., Olabi A.G. (2019) A comprehensive study of the effect of bipolar plate (BP) geometry design on the performance of proton exchange membrane (PEM) fuel cells Renewable and Sustainable Energy Reviews 111 (2019) 236–260 doi: 10.1016/j.rser.2019.04.081
- [13] Bhat M.A., Shaikh A. A. (2014) FEA simulation and geometric calibration of Arcan fixture for butterfly specimen of RP material International Journal of Engineering and Technical Research (IJETR) ISSN: 2321-0869, Volume-2, Issue-10, October 2014
- [14] Abadi R.H., Torun A.R., Fard A.M.Z., Choupani N. (2020) Fracture characteristics of mixed-mode toughness of dissimilar adherends (cohesive and interfacial fracture) Journal of Adhesion Science and Technology <https://doi.org/10.1080/01694243.2019.1674102>
- [15] Nikbakht, M., & Choupani, N. (2008). Numerical investigation of delamination in carbon-epoxy composite using arcan specimen. *International Journal of Mechanical, Industrial and Aerospace Engineering*, 2(4), 259-266.
- [16] Darıck, F., & Aslan, Z. (2017). Characterization of delamination crack in multidirectional e-glass/epoxy composite under mode I loading. *European Mechanical Science*, 1(4), 117-128.
- [17] Mubin, A. N. A., Bahrom, M. H., Azri, M., Ibrahim, Z., Rahim, N. A., & Raihan, S. R. S. (2017). Analysis performance of proton exchange membrane fuel cell (PEMFC). *MS&E*, 210(1), 012052.
- [18] Qi, Z., & Kaufman, A. (2002). PEM fuel cell stacks operated under dry-reactant conditions. *Journal of Power Sources*, 109(2), 469-476.
- [19] Yu, H. N., Kim, S. S., & Do Suh, J. (2010). Axiomatic design of the sandwich composite endplate for PEMFC in fuel cell vehicles. *Composite Structures*, 92(6), 1504-1511.
- [20] Kim, J. S., Park, J. B., Kim, Y. M., Ahn, S. H., Sun, H. Y., Kim, K. H., & Song, T. W. (2008). Fuel cell end plates: a review. *International Journal of Precision Engineering and Manufacturing*, 9(1), 39-46.
- [21] Asghari, S., Shahsamandi, M. H., & Khorasani, M. A. (2010). Design and manufacturing of end plates of a 5 kW PEM fuel cell. *International journal of hydrogen energy*, 35(17), 9291-9297.
- [22] Wang T. W. H., Blum F. D. (1999) Effect of interfacial mobility on flexural strength and fracture toughness of glass/epoxy laminates Journal of Materials Science 34 (1999) 4873 – 4882
- [23] Abaqus 6.11 Analysis User's Manual Volume II Analysis (2011), Dassault Systèmes, USA
- [24] Kaw, A. K. (2006) Mechanics of composite materials, CRC Press, 6000 Broken Sound Parkway NW
- [25] Choupani, N., 2008. Experimental and numerical investigation of the mixed-mode delamination in Arcan laminated specimens. *Materials Science and Engineering: A*, 478(1-2): 229-242.
- [26] Ning, H., Li, J., Hu, N., Yan, C., Liu, Y., Wu, L., ... & Zhang, J. (2015). Interlaminar mechanical properties of carbon fiber reinforced plastic laminates modified with graphene oxide interleaf. *Carbon*, 91, 224-233.
- [27] Salam, S. S., Mehat, N. M., & Kamaruddin, S. (2019, August). Optimization of Laminated Composites Characteristics via integration of Chamis Equation, Taguchi method and Principal Component Analysis. In *IOP Conference Series: Materials Science and Engineering* (Vol. 551, No. 1, p. 012110). IOP Publishing.
- [28] Choupani, N. (2008) Interfacial mixed-mode fracture characterization of adhesive bonded joints. *International Journal of Adhesion and Adhesives*, 28(6), 267-282.
- [29] Choupani, N. (2009). Characterization of fracture in adhesively bonded double-lap joints. *International Journal of Adhesion and Adhesives*, 29(8), 761-773.
- [30] Garić, S., Ivanović, L., Stojanović, B., Miladinović, S., & Milovanović, V. (2016) Numerical Analysis of Aluminum Composite Cylindrical Gears. *Cometa 2016 3rd International Scientific Conference*
- [31] Prini, F., Benson, S. D., & Dow, R. S. (2017, April). The effect of laminate, stud geometry and advance coefficient on the deflection of a composite marine propeller. In *Proceedings of the 6th International Conference on Marine Structures (MARSTRUCT 2017)*. Newcastle University.
- [32] Li, L. L., Wang, Z. Y., Bai, Z. C., Yong, M., Bo, G., Xin, H. T., ... & Bing, L. (2006). Three-dimensional finite element analysis of weakened roots restored with different cements in combination with titanium alloy posts. *Chinese medical journal*, 119(4), 305-311.
- [33] Miura, M., Shindo, Y., Takeda, T. and Narita, F., 2012. Interlaminar fracture characterization of woven glass/epoxy composites under mixed-mode II/III loading conditions at cryogenic temperatures. *Engineering Fracture Mechanics*, 96, pp.615-625.
- [34] Hellier, A. K., Chaphalkar, P., & Prusty, G. B. (2017). Fracture toughness measurement for aluminium 6061-T6 using notched round bars.
- [35] Herráez, M., Fernández, A., Lopes, C. S., & González, C. (2016). Strength and toughness of structural fibres for composite material reinforcement. *Philosophical Transactions of the Royal Society A: Mathematical, Physical and Engineering Sciences*, 374(2071), 20150274.
- [36] Sockalingam, S., Gillespie Jr, J. W., & Keefe, M. (2015). Dynamic modeling of Kevlar KM2 single fiber subjected to transverse impact. *International Journal of Solids and Structures*, 67, 297-310.
- [37] Hosen, M., Alengaram, U. J., Jumaat, M. Z., Sulong, N. H., & Darain, K. (2017). Glass Fiber Reinforced Polymer (GFRP) bars for enhancing the flexural performance of RC beams using side-NSM technique. *Polymers*, 9(5), 180.
- [38] Rao, A. R. M., & Lakshmi, K. (2009). Multi-objective optimal design of hybrid laminate composite structures using scatter search. *Journal of composite materials*, 43(20), 2157-2182.

Referanslar dizi-zeltimeli

- [39] Gdoutos, E.E. (2005) Fracture mechanics An Introduction Second edition, Springer, Netherlands
- [40] Choupani, N., 2008. Experimental and numerical investigation of the mixed-mode delamination in Arcan laminated specimens. *Materials Science and Engineering: A*, 478(1-2), pp.229-242.
- [41] Flom Y., Parker B. H., Chu H. P. (1989) Fracture Toughness of SiC/Al Metal Matrix Composite NASA Technical Memorandum 100745
- [42] Asby M. F., Jones D. R. H. (2006) *Engineering Materials 2 An Introduction to Microstructures, Processing and Design* Third Edition, Elsevier Linacre House, Burlington
- [43] Ozdil, F., Carlsson, L. A., & Davies, P. (1998). Beam analysis of angle-ply laminate end-notched flexure specimens. *Composites Science and Technology*, 58(12), 1929-1938.
- [44] Chalkley, P. and Rider, A., 2003. Toughening boron/epoxy bonded joints using the resin film infusion technique. *Composites Part A: Applied Science and Manufacturing*, 34(4), pp.341-348.
- [45] Zhu Y. (2009) Characterization of Interlaminar Fracture Toughness of A Carbon/epoxy Composite Material The Pennsylvania State University The Graduate School Department of Engineering Science and Mechanics
- [46] Asghari S., Shahsamandi M.H., Khorasani M.R.A. (2010) Design and manufacturing of end plates of a 5 kWPEM fuel cell international journal of hydrogen energy 35 (2010) 929 1-9297 doi:10.1016/j.ijhydene.2010.02.135
- [47] Chung, T. T., Lin, C. T., & Shiu, H. R. (2016). Mechanical design and analysis of a proton exchange membrane fuel cell stack. *Journal of the Chinese Institute of Engineers*, 39(3), 353-362.

Spark Plasma Sintering of Nano Silicon Carbide Reinforced Alumina Ceramic Composites

Mustafa Guven Gok 

Hakkari University, Engineering Faculty, Materials Science and Eng. Department, Turkey

Abstract

Although Al_2O_3 has been commercially preferred material, it cannot be used in applications subject to variable and sudden loads due to its low fracture toughness. In this study, as the primary purpose, nano-SiC particles were used as reinforcement phase to improve the fracture toughness of the Al_2O_3 ceramic. Ultrasonic dispersion was used to ensure good dispersion of the nano reinforcement phase in the matrix. Production was carried out by spark plasma sintering method at temperatures of 1325 °C for 5 min under 40 MPa pressure and vacuum atmosphere. Densification behavior, density, microstructure, phase analysis, hardness and fracture toughness of the sintered Al_2O_3 /nano-SiC composites were investigated. The highest hardness and fracture toughness of 22.83 GPa and 6.09 $\text{MPa}\cdot\text{m}^{1/2}$ were achieved, respectively.

Keywords: Spark Plasma Sintering; Al_2O_3 ; Nano-SiC; Ceramic Composite; Fracture Toughness.

15. INTRODUCTION

Alumina (Al_2O_3), as an engineering ceramic, has high melting temperature (2072 °C), high hardness, low density (3.9 gr/cm^3) and low thermal conductivity. In addition, its corrosion resistance and biocompatibility are very good. Thanks to these features, it has a high potential to be used in a number of sectors such as aerospace and automotive industries, ballistic armor applications, high temperature refractory materials, cutting and abrasive tools and biomaterials. However, fracture toughness value of Al_2O_3 , which is resistance to crack propagation, is quite low [1-5]. This negative feature limits the use of Al_2O_3 . On the other hand, there are many studies to increase the fracture toughness of Al_2O_3 based ceramics through microstructure control and reinforcement phase mechanisms [1, 3, 4, 6-9]. The reinforcement phase mechanism of Al_2O_3 matrix is occurred by secondary phases in the forms of particle and/or fiber. Thus, a composite material is produced. As shown schematically in Figure 1, the main purpose of the reinforcement phase mechanism is to reduce the energy of the crack propagating in the matrix. In the crack deflection mechanism given in Figure 1 (a), as the crack moves through the material, when it intersects with the reinforcement particles, the direction of the crack propagation plane changes and its energy decreases. In the other mechanism called as crack branching (Figure 1 (b)), the crack intersecting with the reinforcement particles splits into two or more cracks and its energy decreases. In the case

of crack bridging mechanism shown in Figure 1 (c), the reinforcement phase in the form of fiber acts like a spring trying to close the crack and prevents further spreading the crack.

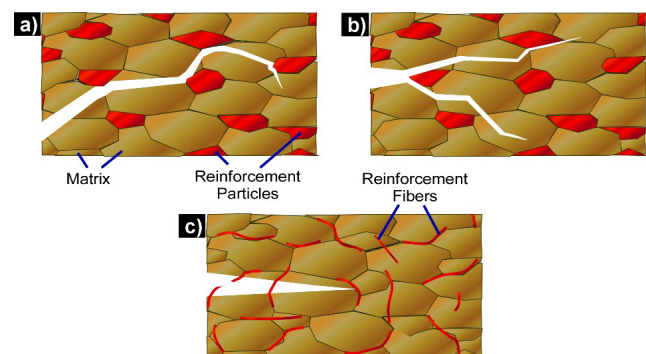


Figure 1. Schematic explanation of the improvement in the fracture toughness through reinforcement phases; crack deflection (a), crack branching (b), crack bridging (c).

When silicon carbide (SiC) is selected as the ceramic reinforcement phase, significant improvements in mechanical properties of the Al_2O_3 are possible [10]. At this point, it is reported that the amount, size, morphology and distribution of SiC phase added into the alumina matrix has a great effect on the mechanical properties of Al_2O_3 [11]. Razavi et al. [10] produced the Al_2O_3 -SiC composite ceramics by using spark plasma sintering (SPS) method at temperatures of 1600 °C for 10 min holding time and they measured the hardness and fracture toughness values of the monolithic Al_2O_3 as 1387 Hv and 250.4 MPa, respectively. Researchers showed that hardness of the composite containing 20 wt. %

* Corresponding author
Email: m.guvengok@hakkari.edu.tr



SiC increased to 2329 Hv and flexural strength of the composite containing 10 wt. % SiC increased to 293.1 MPa. In another study [11], Al_2O_3 -SiC composite containing 17 vol. % SiC was produced by SPS method (1550 °C temperature, 80 MPa pressure and 30 min. holding time) and its hardness value measured as maximum 21.7 GPa. Saheb et al. [2] produced the Al_2O_3 -SiC-CNT composites using the SPS method at 50 MPa pressure, 1500 °C sintering temperature and 10 min. holding time. As a result, they showed that while the fracture toughness value of monolithic Al_2O_3 was 3.61 MPa.m^{1/2}, this value increased to 6.98 MPa.m^{1/2} in the composite of Al_2O_3 -10SiC-2CNT (vol. %). In the study conducted by Alweendo et al. [12] determined the hardness and fracture toughness values of the monolithic Al_2O_3 produced by SPS method as 15.8 GPa and 4.2 MPa.m^{1/2}, respectively. They also showed that it was possible to increase the hardness and fracture toughness up to 16.1 GPa and 4.7 MPa.m^{1/2}, respectively, by adding 10 % SiC by volume.

On the other hand, although there are other pressure and non-pressure sintering processes in ceramic composite production, SPS is one of the newest and technological methods in the production of engineering ceramics. In this method, heat is produced directly on the powders and the molds thanks to the electric current applied in the form of square wave pulses that can be controlled completely, and therefore, the sintering temperature can be reached in a very short time. During the process, pressure is applied to the powders and the microstructure can be controlled by high heating rate [10, 11].

In this study, Al_2O_3 /nano-SiC composites containing different ratio of nano-SiC particles (0-30 vol. %) were produced by using spark plasma sintering process. To achieve good dispersion, the nano-SiC particles were dispersed ultrasonically in the Al_2O_3 matrix. The effects of nano-SiC ratio on densification behavior, microstructure, mechanical properties and phase structure of composites were investigated.

16. MATERIAL AND METHODS

16.1. Powder Preparation

Firstly, commercial Al_2O_3 (*US Research Nano Materials, USA, an average particle size 500 nm, alpha, 99+%*) and (*US Research Nano Materials, USA, 45-65 nm, beta, cubic, 99+%*) SiC powders were weighed in the proportions given in Table 1. Then, the nano SiC powders were added to the merck quality ethanol in separate beakers. An ultrasonic probe (Heiscer-UP200Ht) was placed in beakers containing ethanol and nano SiC powders, and dispersion of nano-sized powders in ethanol was provided for 15 minutes. The process was continuously controlled so that the ethanol in the beaker did not overheat, the ethanol was kept cold with the aqueous system placed under the beaker, and the temperature of the system was measured with a thermometer. After the distribution of nano-sized powders, Al_2O_3 powders were added to the same beakers in appropriate proportions and ultrasonic dispersion was performed for another 15

minutes. Then, magnetic stirring bars were placed to the beakers and the ethanol evaporated on a magnetic stirrer having heater and vacuum fan. The beakers were placed in a drying-oven at 80 °C to dry the powders completely.

Table 1. Sample Compositions.

Specimen Name	Amount of Powder (vol. %)	
	Al_2O_3	SiC
100A	100	-
90A10S	90	10
80A20S	80	20
70A30S	70	30

16.2. Spark Plasma Sintering Process

Prepared powders were sintered by using spark plasma sintering process. A SPS system (7.40 MK VII, SPS Syntex Inc.) with a capacity of 20000A was used. Thanks to this system, composite specimens with 50 mm diameter and 5 mm thickness were produced as shown in Figure 2. Graphite molds having 50 mm inner-diameter and graphite punches were used for composite production. The inner surface of the mold was covered with graphite paper, the lower punch was placed and graphite papers were placed both on the surfaces of upper and lower punches. The powder to be sintered was poured into mold cavity and upper punch placed. Then, the graphite mold was pre-compressed under 10 MPa pressure by using a hand press. In order to minimize heat loss, the graphite molding system was surrounded by a graphite blanket and sintering carried out in a vacuum environment. During SPS process, current was increased manually and shrinkage curves were controlled continuously. 40 MPa pressure was applied to the punches and pulsed direct current (12 ms/on, 2 ms/off) was passed through the samples and graphite molds during sintering process. The process was completed by holding the specimens 5 minutes at temperature of 1325 °C. Temperature measurements were performed by a pyrometer from the outside of chamber. During sintering, a software was used to control instant parameters such as shrinkage, shrinkage rate, temperature, vacuum value, current, voltage and pressure, and a heating rate of 150 °C/min was applied.

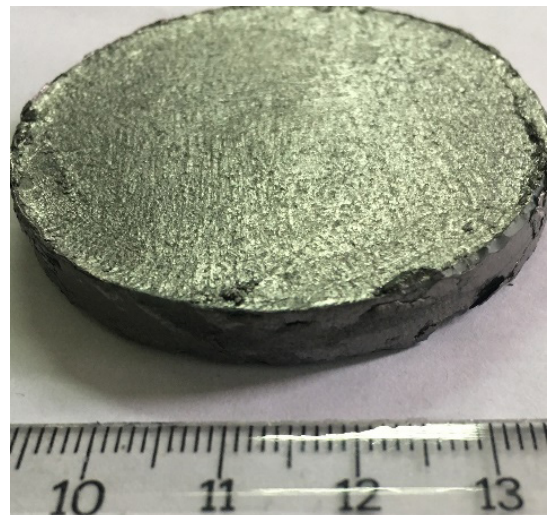


Figure 2. Macro image of the sample produced via SPS process.

16.3. Characterization Methods

The sintering behaviors of the specimens were evaluated by using shrinkage curves obtained from the SPS device. Density of the specimens was determined using Archimedes' principle. Theoretical density values of composites were determined according to the mixture rule and these theoretical values were proportioned to the measured density values. Thus, the relative density values of the composites were calculated (Equation 1).

$$D_R = \frac{D_B}{D_T} \times 100 \quad (1)$$

In this equation, D_R is the relative density (g/cm^3), D_B is the density of the sintered sample (g/cm^3) and D_T is the theoretical density. Microstructural and elemental analysis of the samples were performed by using Field Emission Scanning Electron Microscope (FESEM, JEOL JSM 7000F) and Energy Dispersion Spectrometer (EDS – Oxford/Inca), respectively. Phase analysis of the samples were carried out with X-ray diffractometer (XRD, Rigaku Miniflex) using $\text{Cu-K}\alpha$ radiation at a scanning speed of $2^\circ/\text{min}$ at 2θ : $10\text{--}80^\circ$. In addition, the parts cut from the samples were molded with bakelite and polished in the automatic polishing machine (Metcon) using various levels of sandpaper and piano discs. In the final stages, surface polishing process was applied with $3\ \mu\text{m}$ and $1\ \mu\text{m}$ diamond paste. The hardness of the samples was determined in a Vickers microhardness measuring device (Leica VH-MOT) by applying 12 seconds of action time and 9.8 N load. At least 15 measurements were taken for each sample and both average hardness values and standard deviations were calculated. Fracture toughness measurements

of the samples were also carried out using the same hardness device, applying 12 seconds of action time and 19.6 N load. The elasticity modules of the composites were calculated with the rule of mixtures. Fracture toughness values of the samples were calculated by Anstis equation (Equation 2) [13].

$$K_{IC} = k \times \left(\frac{E}{H}\right)^{1/2} \times \left(\frac{P}{c^{3/2}}\right) \quad (2)$$

here; k is the geometry constant (0.016 ± 0.004), P is the applied load, E is the modulus of elasticity of the composite, H Vickers hardness value and c is half of the average crack length.

17. RESULTS AND DISCUSSIONS

17.1. Densification behavior

The shrinkage curves for the produced samples were given in Figure 3 (a-d). These graphs were plotted as displacement of graphite punches (mm) versus temperature ($^\circ\text{C}$).

During the SPS process, the densification occurring in the powders with the increase of temperature at constant pressure is determined from the displacement amount of the graphite punches due to the shrinkage. After a certain temperature value that is different for each material and composition, the shrinkage is completed and remains constant [6, 8]. Therefore, in order to obtain a dense structure, the sintering temperature should be equal or higher than the temperature at which shrinkage is completed. In this study, the starting and completion temperatures of the shrinkage for monolithic Al_2O_3 and Al_2O_3 -nano-SiC composite samples were determined (see Table 2).

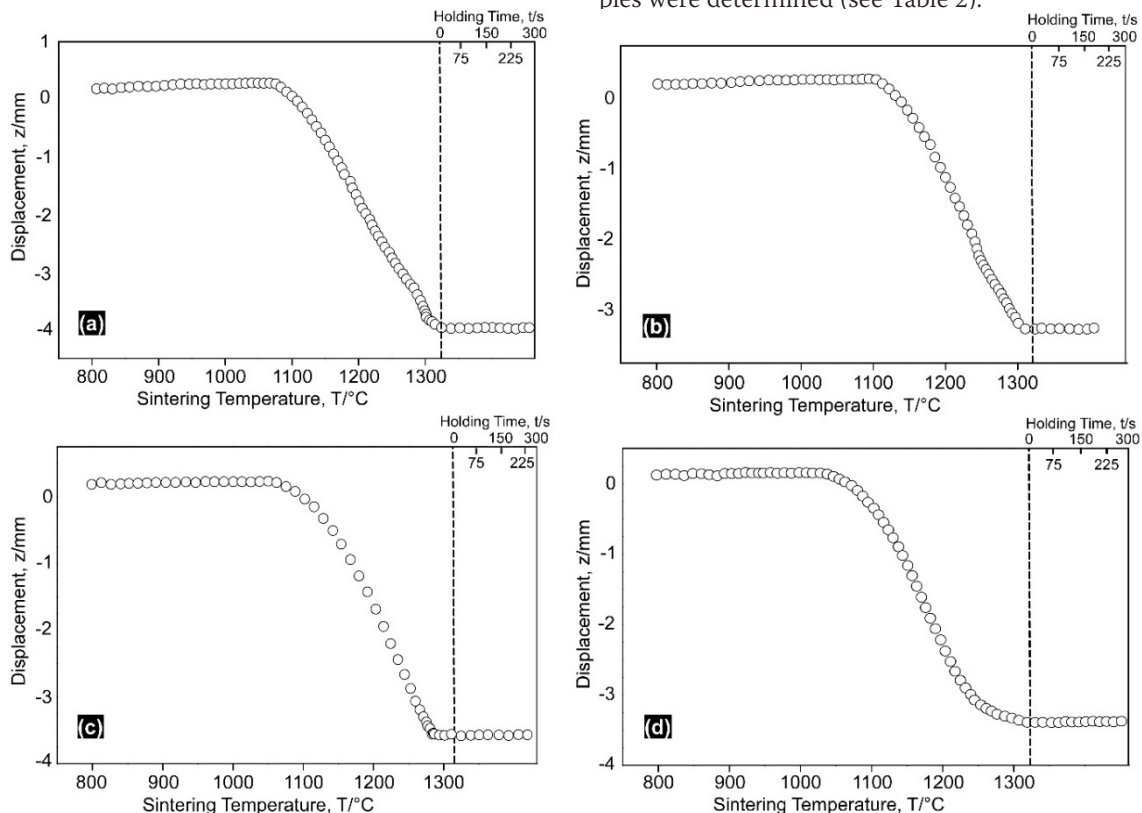


Figure 3. Shrinkage graphs of the samples produced by SPS process, 100A (a), 90A10S (b), 80A20S (c) and 70A30S(d).

Table 2. Starting and completion temperatures of the shrinkage.

Specimen Name	Shrinkage Temperatures (°C)	
	Starting	Completion
100A	1070	1325
90A10S	1105	1305
80A20S	1075	1290
70A30S	1045	1280

As seen in Figure 3 and Table 2, during SPS process performed with a constant heating rate, the starting and completion temperatures of the shrinkage decreased thanks to the nano-SiC added to Al_2O_3 . The reason for this decrease occurring in the starting and ending temperatures of sintering was thought to be due to the increase in the conductivity of the composite by SiC, whose electrical conductivity is higher than Al_2O_3 . The mechanism of the increase in electrical conductivity of Al_2O_3 by adding SiC has been explained by Saheb et al [2]. As a result, it is possible to conclude that an improvement took place in the sintering behavior of the Al_2O_3 thanks to added nano-SiC particles.

The densities of the specimens produced by the SPS process were determined by Archimedes' Principle. According to the results, it was understood that the relative density values of the specimens varied among 99.7% and 95.2% (see Table 3). The monolithic Al_2O_3 (99.7%) had the highest relative density value among all samples. The lowest relative density value (95.2%) belonged to the specimen of 70A30S sample containing 30% SiC by volume. It was determined that relative density values decreased with increasing nano-SiC ra-

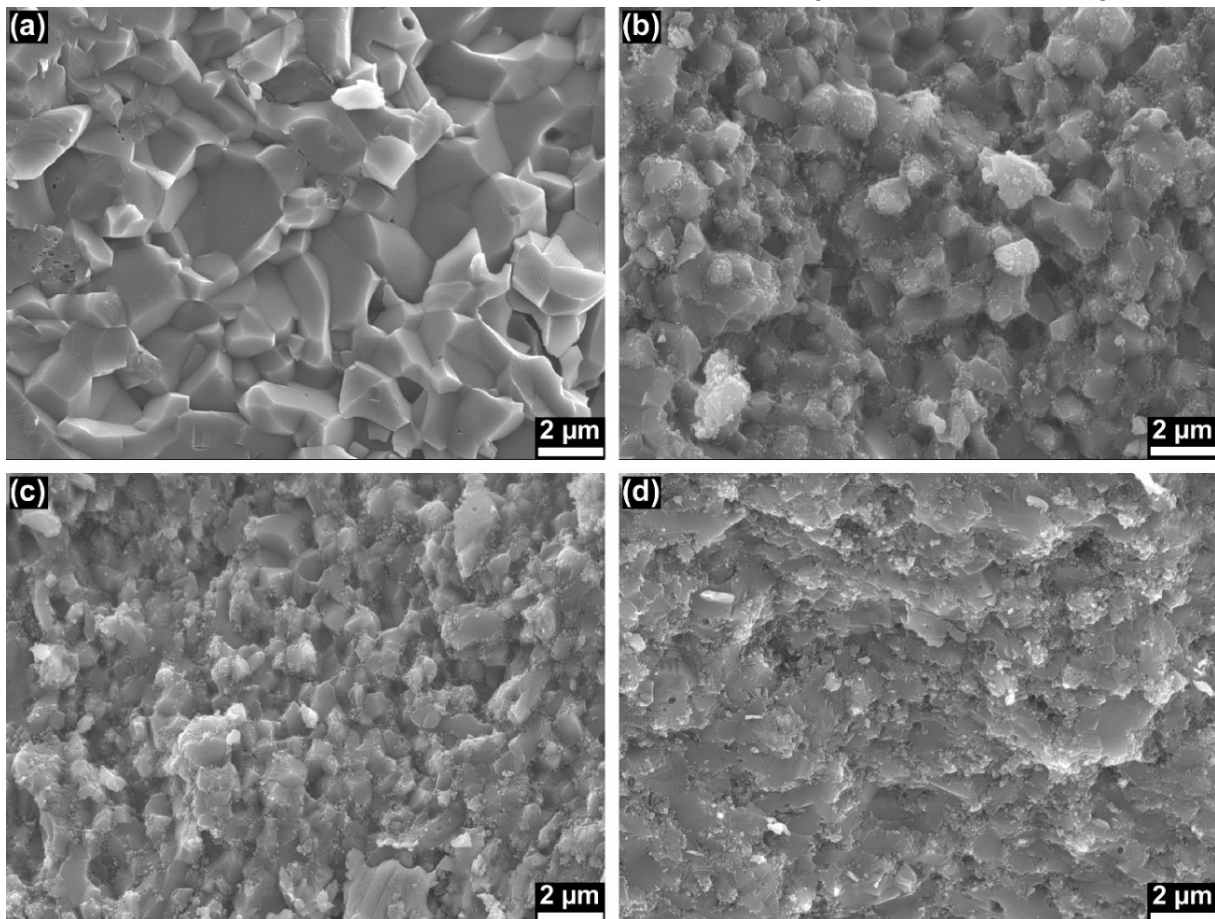
tio. This decrease in density values occurred due to the poor sintering property of the SiC. A similar behavior (decrease in density with increasing SiC ratio added to Al_2O_3) was observed in the study of Alweendo et al. [12].

Table 3. Relative density, hardness and fracture toughness values.

Specimen Name	Relative Density (%)	Hardness (Hv)		Fracture Toughness (K_{IC})	
		GPa	Std Dev	($MPa\cdot m^{1/2}$)	Std Dev
100A	99.7	18.27	± 0.73	2.94	± 0.36
90A10S	98.1	21.07	± 0.41	5.81	± 0.43
80A20S	97.2	22.34	± 0.57	6.09	± 0.39
70A30S	95.2	22.83	± 1.10	4.37	± 0.87

17.2. Microstructural Characterizations

FESEM images taken from the fracture surface of the produced specimens using secondary electron detector were given in Figure 4 (a-d). In Figure 4 (b-d), nano-sized SiC grains has been noticed. Especially in Figure 4 (b) and (c), it is seen that the nano-sized SiC grains were homogeneously distributed in the Al_2O_3 matrix. Therefore, it can be said that the ultrasonic nano-SiC dispersion process was successful up to 20% by volume. However, the same homogeneous distribution could not be observed in 70A30S sample containing 30% SiC by volume (Figure 4 (d)). In Figure 4 (a), the microstructure of monolithic Al_2O_3 , the coaxial grains were quite distinct and it is understood that there was intergranular fracture. The granular structure in the 70A30S sample was not evident (Figure 4 (d)). This was due to the transgranular fracture. The fracture mode started to transform from intragranular fracture to transgranular fracture

**Figure 4.** FESEM microstructures of spark plasma sintered specimens; 100A (a), 90A10S (b), 80A20S (c), 70A30S (d).

with the increasing SiC ratio. On the other hand, it is clearly seen that the grain size of the Al_2O_3 matrix decreased with the addition of nano-SiC to the structure. Nano sized SiC particles located around Al_2O_3 grains and prevented the propagation of the grain boundary. Therefore, the grain size of the Al_2O_3 matrix decreased with the nano-SiC addition.

The elemental distributions (by weight) of the EDS spectra taken from the general surface regions of the samples were given in Table 4. In this table, Al, Si, C and O were chemical symbols of aluminum, silicon, carbon and oxygen, respectively. It is understood that the initial powder compositions (by volume \rightarrow weight) and the values obtained from the EDS results of the produced samples were consistent.

Table 4. Results of elemental analysis

Specimen Name	Weight % Element			
	Al	Si	C	O
100A	62,38	-	-	37,62
90A10S	36,74	4,70	10,41	48,15
80A20S	39,60	10,60	15,84	33,96
70A30S	22,65	12,34	27,42	37,58

17.3. Phase Analysis

In order to understand the phases formed after sintering, XRD analysis were performed and the patterns were given in Figure 5. This process was carried out with an X-ray diffractometer using Cu-K α radiation at a scanning speed of 2°/min at 2 θ : 10-80°. As a result, it was understood that the monolithic Al_2O_3 sample had the structure of α - Al_2O_3 (JCPDS: 71-1683) after SPS process. In case of adding SiC up to 20%, the peaks of the SiC phase appeared and there was no change in the Al_2O_3 structure. However, peaks of the $\text{Al}_2\text{Si}_2\text{O}_5$ phase were revealed in the sample containing 30% SiC by volume.

17.4. Mechanical Properties

Vickers microhardness and fracture toughness values of Al_2O_3 -based composites sintered under 40 MPa pressure for 5 min. with the SPS method are given in Table 3. While the hardness value of monolithic Al_2O_3 was 18.27 GPa, it increased to 21.07 GPa with the addition of 10% SiC by volume and 22.34 GPa with the addition of 20% SiC by volume. This was due to the nano-SiC particles preventing dislocation movement during plastic deformation caused by hardness measurement. In addition, increasing in hardness could be explained by the reduction of the grain size of Al_2O_3 matrix by adding nano-SiC to the structure. The grain boundary areas increased with decrease in grain size and these grain boundary areas prevented the movement of dislocations. However, it was determined that the hardness value did not increase any more if 30% SiC by volume was added to the Al_2O_3 matrix (22.83 GPa).

As a result of fracture toughness measurements, it was understood that a significant improvement occurred in the fracture toughness value with nano-SiC addition to Al_2O_3 (Table 3). The fracture toughness value of monolithic Al_2O_3 , calculated as 2.94 $\text{MPa}\cdot\text{m}^{1/2}$, increased to 5.81 and 6.09

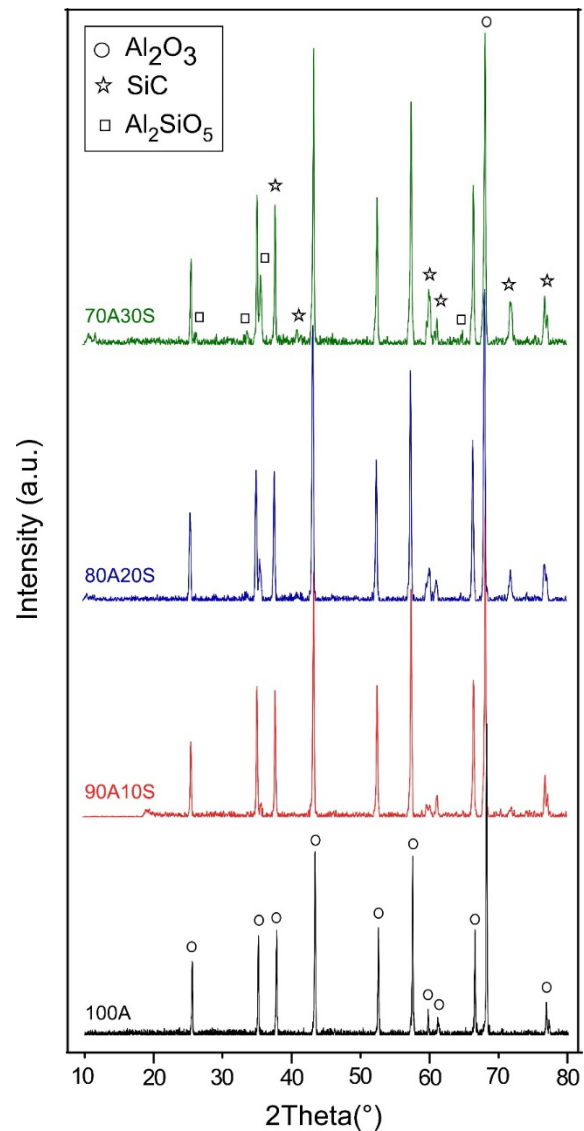


Figure 5. XRD patterns.

$\text{MPa}\cdot\text{m}^{1/2}$ with the addition of 10% and 20% SiC, respectively. This increase in fracture toughness can be explained by the "Crack Deflection" mechanism caused by nano-sized SiC particles, as Shi et al [14] mentioned. The directions of the cracks propagating in the structure changed when they intersected with the SiC grains and moved in a zigzag pattern (see Figure 6). In this way, the energy of the cracks was reduced and the fracture toughness values of the Al_2O_3 -nano SiC composite were improved.

However, the fracture toughness value of Al_2O_3 containing 30% nano-SiC by volume decreased to 4.37 $\text{MPa}\cdot\text{m}^{1/2}$. A similar decrease in fracture toughness after a certain SiC addition (30% SiC by weight) was observed in a study in the literature [15]. This situation was explained by three mechanisms: (I) high agglomeration of nano-SiC particles occurring at 30% SiC addition (see Figure 7), (II) low fracture toughness of the $\text{Al}_2\text{Si}_2\text{O}_5$ (1-1.8 $\text{MPa}\cdot\text{m}^{1/2}$ [16]), which formed in the 70A30S sample, (III) excessive residual stresses in the structure as a result of thermal expansion mismatches of Al_2O_3 and SiC. As seen in Figure 7, which is the high magnification SEM image of 70A30S, nano-SiC particles agglomerated in the Al_2O_3 grain boundary regions when 30% nano-SiC by vol-

ume was added.

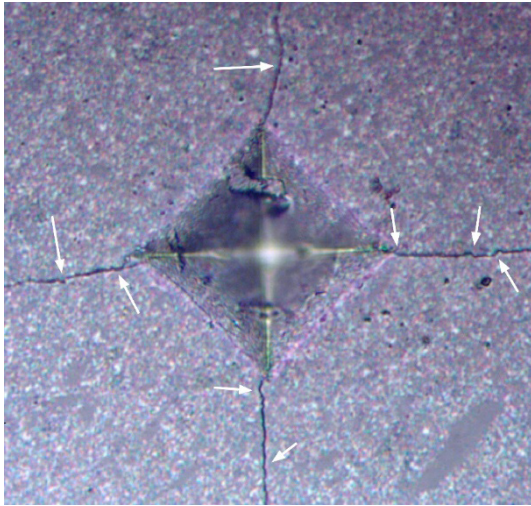


Figure 6. Vickers indentation cracks on the surface of produced Al_2O_3 -nano SiC composite.

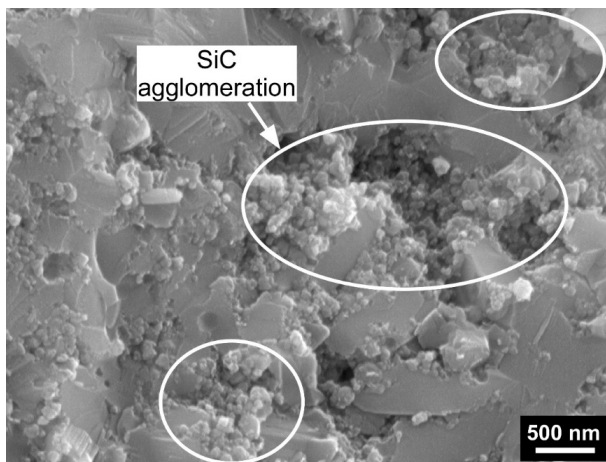


Figure 7. Agglomeration of nano-SiC particles in the grain boundary regions of Al_2O_3 .

18. CONCLUSIONS

As a result of the experimental studies, cylindrical shaped Al_2O_3 /nano-SiC specimens with a diameter of 50 mm were produced by spark plasma sintering process and their sintering behavior, density, microstructure, phase structure, hardness and fracture toughness were analyzed. According to these analysis:

1. The temperatures at which shrinkage started and completed were decreased with the increasing SiC addition. This situation was explained by the increase in the conductivity of the composite with the increasing SiC addition.
2. The relative density of monolithic Al_2O_3 was 99.7%. However, this value decreased up to 95.2% with the increasing SiC addition.
3. The grain size decreased and the fracture mode changed to transgranular fracture from intergranular fracture with the SiC addition.
4. The hardness increased from 18.27 GPa to 22.83 GPa.
5. While the fracture toughness of the monolithic Al_2O_3

was $2.94 \text{ MPa}\cdot\text{m}^{1/2}$, a maximum value of $6.09 \text{ MPa}\cdot\text{m}^{1/2}$ was obtained with the addition of nano-SiC.

6. Addition of 20 vol% SiC was the maximum point for mechanical properties, and over this addition amount the fracture toughness value decreased due to the agglomeration of nano-SiC, excessive residual stress and the formation of $\text{Al}_2\text{Si}_2\text{O}_5$ phase.

Acknowledgments

This work was supported by the Hakkari University Scientific Research Projects Unit (project number: FM2017BAP10). The author thanks to Prof. Dr. Gultekin Goller for his permission to use Biomaterials Research and Characterization Laboratory of Istanbul Technical University.

REFERENCES

- [1] D. Pravarthana et al. (2013). "Growth and texture of spark plasma sintered Al_2O_3 ceramics: A combined analysis of X-rays and electron back scatter diffraction," *Journal of Applied Physics*, vol. 113, no. 15, pp. 153510, doi:10.1063/1.4802439.
- [2] N. Saheb, U. Hayat, and S. F. Hassan. (2019). "Recent advances and future prospects in spark plasma sintered alumina hybrid nanocomposites," *Nanomaterials*, vol. 9, no. 11, pp. 1–43, doi:10.3390/nano9111607.
- [3] J. Liu, Z. Li, H. Yan, and K. Jiang. (2014). "Spark plasma sintering of alumina composites with graphene platelets and silicon carbide nanoparticles," *Advanced Engineering Materials*, vol. 16, no. 9, pp. 1111–1118, doi: 10.1002/adem.201300536.
- [4] J. Liu, H. Yan, and K. Jiang. (2013). "Mechanical properties of graphene platelet-reinforced alumina ceramic composites," *Ceramics International*, vol. 39, no. 6, pp. 6215–6221, doi: 10.1016/j.ceramint.2013.01.041.
- [5] K. Ahmad and W. Pan. (2015). "Microstructure-toughening relation in alumina based multiwall carbon nanotube ceramic composites," *Journal of the European Ceramic Society*, vol. 35, no. 2, pp. 663–671, doi:10.1016/j.jeurceramsoc.2014.08.044.
- [6] I. Akin. (2015). "Investigation of the microstructure, mechanical properties and cell viability of zirconia-toughened alumina composites reinforced with carbon nanotubes," *Journal of the Ceramic Society of Japan*, vol. 123, no. 1437, pp. 405–413, doi:10.2109/jcersj2.123.405.
- [7] D. Chakravarty, S. Bysakh, K. Muraleedharan, T. N. Rao, and R. Sundaresan. (2008). "Spark plasma sintering of magnesia-doped alumina with high hardness and fracture toughness," *Journal of the American Ceramic Society*, vol. 91, no. 1, pp. 203–208, doi:10.1111/j.1551-2916.2007.02094.x.
- [8] O. Ormanci et al. (2014). "Spark plasma sintered Al_2O_3 -YSZ- TiO_2 composites: Processing, characterization and in vivo evaluation," *Materials Science and Engineering C*, vol. 40, pp. 16–23, doi:10.1016/j.msec.2014.03.041.
- [9] S. Rattanachan, Y. Miyashita, and Y. Mutoh. (2008). "Microstructure and fracture toughness of a spark plasma sintered Al_2O_3 -based composite with BaTiO_3 particulates," *Journal of the European Ceramic Society*, vol. 23, no. 8, pp. 1269–1276, doi:10.1016/S0955-2219(02)00294-7.
- [10] M. Razavi, A. R. Farajpour, M. Zakeri, M. R. Rahimpour, and A. R. Firouzbakht. (2017). "Production of Al_2O_3 -SiC nano-composites by spark plasma sintering," *Boletin de la Sociedad Espanola de Ceram-*

ica y Vidrio, vol. 56, no. 4, pp. 186–194.

- [11] I. Álvarez, R. Torrecillas, W. Solis, P. Peretyagin, and A. Fernández. (2016). "Microstructural design of Al₂O₃-SiC nanocomposites by Spark Plasma Sintering," *Ceramics International*, vol. 42, no. 15, pp. 17248–17253.
- [12] S. T. Alweendo, O. T. Johnson, B. M. Shongwe, F. P. Kavishe, and J. O. Borode. (2020). "Microstructural and mechanical properties of alumina (Al₂O₃) matrix composites reinforced with SiC from rice husk by spark plasma sintering," *Materials Research*, vol. 23, no. 1, pp. 1–9.
- [13] G. R. Anstis, P. Chantikul, B. R. Lawn, and D. B. Marshall. (1981). "A Critical Evaluation of Indentation Techniques for Measuring Fracture Toughness: I, Direct Crack Measurements," *Journal of the American Ceramic Society*, vol. 64, no. 9, pp. 533–538.
- [14] X. L. Shi et al. (2010). "Mechanical properties of hot-pressed Al₂O₃/SiC composites," *Materials Science and Engineering A*, vol. 527, no. 18–19, pp. 4646–4649.
- [15] K. S. Torosyan et al. (2020). "Reactive, nonreactive, and flash spark plasma sintering of Al₂O₃/SiC composites—A comparative study," *Journal of the American Ceramic Society*, vol. 103, no. 1, pp. 520–530.
- [16] D. L. Whitney, M. Broz, and R. F. Cook. (2007). "Hardness, toughness, and modulus of some common metamorphic minerals," *American Mineralogist*, vol. 92, no. 2–3, pp. 281–288.



Building up Mathematical Modeling Using Spot Welding Parameters and Prediction Weld Nugget by Minitab

İlhan Çekiç^{1*} , Kadir Çavdar² 

¹Bursa Uludağ Üniversitesi, Mühendislik Fakültesi, Makine Mühendisliği Bölümü, 16059 Nilüfer Bursa.

²Bursa Uludağ Üniversitesi, Fen Bilimleri Enstitüsü, Makine Mühendisliği Anabilim Dalı, 16059 Nilüfer Bursa

Abstract

In serial production, problems are constantly encountered in the selection of welding parameters due to the excess of welding parameters and variations. In order to compensate for these variations, mostly high energy flux is used. In this study, an approach developed in order to estimate weld nugget diameter in determining the welding parameters for sheets with a thickness of 0.6-3 mm is introduced. Sheet is an iron-based material that has been given certain mechanical and chemical properties in standards, turned into sheets from thick plates by rolling processes. Minitab statistical program was used to create experimental data and mathematical operations. First of all, 7 source parameters were selected and experimental study was carried out for 64 experiments using the 1/2 partition factorial method of design of experiments(DOE) in Minitab software. With the experiments, real weld nugget diameters were obtained. These results were transferred to the Minitab software and the mathematical model of the system was established. Weld nugget diameter estimation procedures were carried out using the data of factorial design of experiments(DOE). Test and prediction data were transferred to Minitab software, regression graph was drawn and R-Sq and R-Sq (adj) values were calculated. In addition, samples were created with randomly selected data for verification and comparison was made by transferring them to Minitab. According to the results of this study, remarkable accuracy rates have been achieved in the weld nugget diameter estimation with Minitab.

Keywords: Resistance spot welding, weld nugget prediction, design of experiment, regression analysis, Minitab.

19. INTRODUCTION

Today, 7-12 thousand spot welding is used when a car is being produced. Electric Resistance Welding (ERW) is generally done by computer controlled robots. The quality of ERW is an extremely important issue in the automotive industry. The accuracy and consistency of parameter settings made with manual welding parameter calculations, operator experience and technician expertise may not be appropriate.

Welding parameter setting of each machine and point is a difficult process due to many sensitive factors. It takes a lot of trials with a large number of materials to find the optimum value of each spot to be spot welded, which cannot be done as it is very costly. In order to achieve the final standard welding quality, different sheet thicknesses such as electrodes etc. The process of adjusting the parameters in each different welding machine model by changing it is quite costly. Therefore, in the ERW spot welding process, it is important to be able to meet the weld quality improvement requirements with efficiency estimation and appropriate parameter

optimization.

When the literature is examined in general, it is seen that studies are carried out on a single sheet thickness by taking only the welding time, current and force. Different approaches can be seen for estimation methods.

In another method, welding current, electrode force and welding time other welding parameters can be kept constant. Welded joints can be subjected to tensile-shear tests to determine shear force and absorption energy values. In the study, parameter optimizations can be performed by using the surface methodology based on Box-Behnken design to generate a quadratic response model regression from Yue *et al.* [1].

There are also approaches to applying data mining techniques to estimate the weld nugget diameter in the ERW resource. With a relatively simple and straightforward approach, it can accurately estimate the diameter of a spot from easily measured signals during the welding process by Boersch *et al.* [2].

* Corresponding author
Email: i_cekic@hotmail.com



In addition, a real resource test dataset collected from the field can be predicted by using regression models such as a decision tree algorithm to extract decision rules. Here it can be seen that semantic rules are used to create accurate predictive models. With this method, allow engineers to reduce design and process alternatives response parameter (weld nugget width) can be effectively analyzed and predicted by Kim *et al.* [3].

There is a direct correlation between the selected parameters and the cooling rate and sheet thickness. It is an important factor in the formation of hardness values especially around the weld nugget region and weld nugget. It can be seen that the extreme hardness values negatively affect the rupture and weld nugget diameter values in the weld zone, which negatively affects the weld nugget diameter by Sheikhi *et al.*, Kemda *et al.* [4,12].

With samples created under variable welding currents I, electrode forces F, welding times T, preheating currents IA, single-predictive optimization and spot break load estimation can be performed. Signal-to-Noise (S/N) ratio analysis and response surface modeling can be performed using RSM (response surface methodology) for optimization and prediction by Duric *et al.* [5].

In the other study, it is to present a prediction for the welded metal sheets characteristics as a result of varying parameters of resistance spot welding, also to predict the optimal welded material property for any given resistance spot welding parameters, besides, to foresee the probability of failure in the welding process before happening using simulation from the study of by Hiba *et al.*, Hayat F. [8,10].

A modified central compound design can be adopted to formulate an effective regression model that requires fewer experiments. The response surface methodology can be used to achieve optimum process conditions. Force current, welding time and welding force input variables, shear strength and spot crush amount can be output variables. By using TRIP steel, it is possible to obtain an optimum weld quality under relatively low welding currents and extending the welding time by Kim *et al.* [9].

Rather than using the result of a non-destructive testing technique as input variables, classifiers are trained directly with the relevant welding parameters, namely welding current, welding time and electrode type (electrode material and machining). Algorithms are compared for accuracy and area under receiver operating characteristic curve criteria using nested cross validation. Support vector machines using radial weld nugget, acceleration, and random forest techniques can generally achieve the best performance by Pereda *et al.* [11].

It also includes weld adhesion, the influence of weld parameters on joint quality, major metallurgical defects in Al spot welds, and electrode distortion. The contact resistance caused by the presence of an oxide layer on the surface of

Al alloys and the need for high current application due to Al alloys cause rapid electrode tip wear and inconsistency in welding quality. Cleaning the oxide layer and increasing the electrode strength and applying a low current preheating can significantly reduce the contact resistance and improve the connection quality from Manladan *et al.* [13].

In the studies presented in this article, unlike previous studies, a model was created by studying not only 3 parameters (current, force and time), but 7 parameters as used in mass production. In addition, in order to establish the ERW model in the most ideal conditions and accuracy, an experiment design was made and a statistically accurate model was formed. Verification tests are performed on the model whose accuracy is certain and the accuracy of the model has been clearly tested. The created model can also be used by researchers who want to do different studies.

In this study, as can be seen in the outputs of the test design study in the Minitab program, the effects of cooling time, approach and printing time have been tested with the test specimens shown in Fig. 1 by making $\frac{1}{2}$ -fraction test design in standard sizes, different sheet thicknesses. Afterwards, the mathematical model of the system was created.

After obtaining the model, the parameters were considered individually in the Minitab program and their correlation with the weldnugget diameter was examined. In addition, randomly selected parameters were applied in the field and real weld nugget diameters were found. These weld nugget diameters have been tried to be estimated with Y_predict in Minitab program. Then, the accuracy of the system was investigated by examining the regression of the field and predicted values and calculating the R-Sq and R-Sq (adj) values.

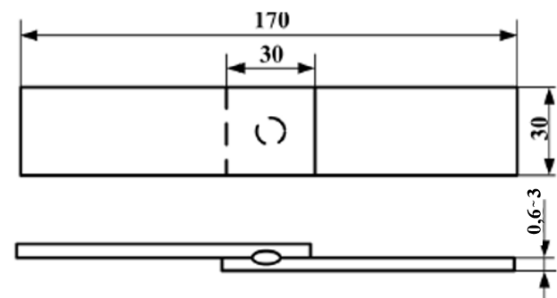


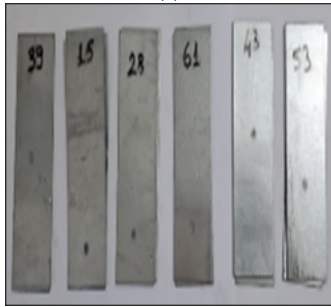
Figure 1. Welded specimen dimensions (in mm)

20. MATERIAL AND METHOD

The method used in the studies conducted in this section is summarized. In this research, ERW process was carried out under real conditions with a Unis Makina 100 kVA and 100 Hz fixed spot welding machine. In this study, 0.6-3mm ref. sheet thicknesses were used according to the sheet thickness and parameters in the experimental design. These sheets, 6 and 8 mm diameter copper alloy tip were used in the experiments, see Fig. 2. Welding parameters, welding time, force, cooling, squence, holding and sheet thickness. and the weld nugget diameter output was investigated by using $\frac{1}{2}$ fraction experimental design.



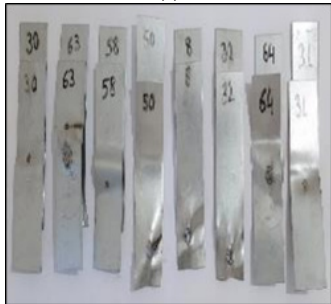
(a)



(b)



(c)



(d)

Figure 2. Application of experimental design data in the workshop (a) Welding application; (b,c,d) Tearable specimen

20.1. Design of Experiment-DoE

DoE is a systematic method for determining the relationship between factors affecting a process and the outcome of that process. In other words, it is used to find cause and effect relationships. This information is needed to manage process inputs to optimize output. In the design of the experiment, first of all the minimum and maximum values of each parameter are entered into the system. Then, what degree of experiment design will be done, that value is selected. The system is then asked to create the experiment design. The system randomly assigns each attempt to reflect the entire model.

In addition, Minitab 18 Statistical Software program was used in the studies. Here, an experimental design of 65 pa-

rameters was created, with 64 and 1 center point (Fig. 3). The test was repeated with the same parameters in order to guarantee the accuracy of the parameters and weld nugget diameters obtained.

Although different sheet thicknesses are used experimentally in the study, the mechanical and chemical composition of only 0.8 mm sheet for simplicity is given in Table 1 and Table 2. These sheets are supplied by Erdemir company and their certificate number is 0031742Y and dated 18.3.2020.

Fractional Factorial Design

Design Summary			
Factors:	7	Base Design:	7; 64
Resolution:	VII	Runs:	65
Replicates:	1	Fraction:	1/2
Center pts (total):	1	Blocks:	1

Figure 3. Minitab parameters of experiment design

Table 1. Chemical structure of 0.8 mm thick specimen sheet

FEE 220 BH-ZNT/F/2S (ERDEMİR 0380) -0.8mm								
	%C	%Mn	%Si	%P	%S	%Al	%Ni + %Cu + %Cr + %Mo	%C + %P
% min	0.007	0.15		0.05		0.02	≤ 0.5	≤ 0.16
% maks	0.06	0.7	0.5	0.09	0.03	0.07		

Table 2. Mechanical properties of 0.8 mm thick sheet

FEE 220 BH-ZNT/F/2S (ERDEMİR 0380) – 0.8mm				
Tensile Test	Tensile Strength (MPa)	Yield Strength (MPa)	%Elongation	
Min:max	305	400	200	270
				34

In Annex A, a part of the weld nugget diameters obtained as a result of the experiments carried out in the field, as opposed to the 1/2 partition factorial input parameters obtained by the experimental design, are summarized.

It is seen in Annex B that the input parameters and their double-triple combinations are effective on the system. The values given here are the values obtained after applying backward elimination against the alpha value in the Minitab program.

20.2. Backward Elimination

It is a method for determining which variables to keep or not in a model. The backward elimination begins with the model containing all terms and then progressively removes the terms one by one using the same method. No variable can re-enter the model.

The probability value *P* shows the amount of possible error we will make when we make the decision "there is a statistically significant difference" in a comparison. The maximum acceptable level of this error was suggested and accepted as 0.05. If the *P* value found in a test result is below 0.05, it means that there is a significant difference as a result of the comparison.

Alpha number is the threshold value at which we meet *P* values. Describes how excessively observed results should be to reject the null hypothesis of a significance test. The default backward elimination procedure ends when all of the variables included in the model are left with variables with a

P value greater than the value specified in Alpha.

2.2.1 Stepwise Method

Performs variable selection by adding or deleting predictors from the existing model based on the *F*-test. Stepwise is a combination of forward selection and backward elimination procedures. Stepwise selection does not proceed if the initial model uses all of the degrees of freedom.

2.1.2 Variable to Remove

Minitab calculates an *F*-statistic and *P*-value for each variable in the model. If the model contains *j* variables, then *F* for any variable, x_j , is this formula:

$$F = \left(\frac{SSE_{(j-x_j)} - SSE_j}{DFx_j} \right) / (MSE_j) \tag{1}$$

Here,

SS : Square of standard deviation

MS : Square of means

$SSE_{(j-x_j)}$: SS Error for the model that does not contain x_j

SSE_j : SS Error for the model that contains x_j

MSE_j : MS Error for the model that contains x_j

If the *P*-value for any variable is greater than the value specified in Alpha to remove, then Minitab removes the variable with the largest *p*-value from the model, calculates the regression equation, displays the results, and initiates the next step.

2.1.3 Variable to Add

If Minitab cannot remove a variable, the procedure attempts to add a variable. Minitab calculates an *F*-statistic and *p*-value for each variable that is not in the model. If the model contains *j* variables, then *F* for any variable, x_a , is this formula:

$$F = \left(\frac{SSE_{-j} - SSE_{(j+X_a)}}{DFx_a} \right) / (MSE_{(j+X_a)}) \tag{2}$$

DF : Degrees of freedom

SSE_{-j} : SS Error before x_a is added to the model

$SSE_{(j+x_a)}$: SS Error after x_a is added to the model

DFx_a : Degrees of freedom for variable X_a

$MSE_{(j+x_a)}$: MS Error after x_a is added to the model

If the *P*-value corresponding to the *F*-statistic for any variable is smaller than the value specified in Alpha to enter, Minitab adds the variable with the smallest *P*-value to the

model, calculates the regression equation, displays the results, then goes to a new step. When no more variables can be entered into or removed from the model, the stepwise procedure ends.

By making Minitab \ Stat \ DOE \ Factorial \ AnalysisFactorialDesign \ Stepwise \ backward elimination, the ideal probability coefficient $P > 0,05$ is automatically drawn in all input parameters. Here, resource time is the parameter with the greatest impact. As seen in Annex A, all parameters and their combinations affect the weld nugget diameter. Here; $S = 0.0847054$ R-Sq = 99.53% R-Sq (adj) = 96.69 and the accuracy of the system is quite high. Welding current is the input parameter with the greatest impact on the entire system, cooling as a single parameter the least effective. The singular and percentage effects of the effects of the parameters are shown below, Figures 4 and 5. Here, it is seen that the combinations of 2 and 3 of the parameters are much more effective instead of individual parameters. The values are given interactively in Fig. 6.

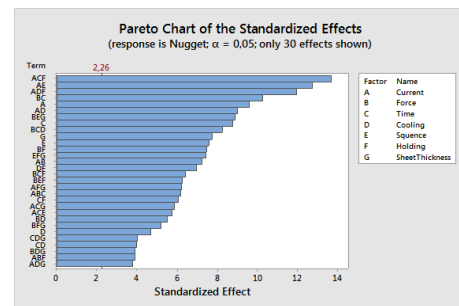


Figure 4. Standart effects of welding parametres

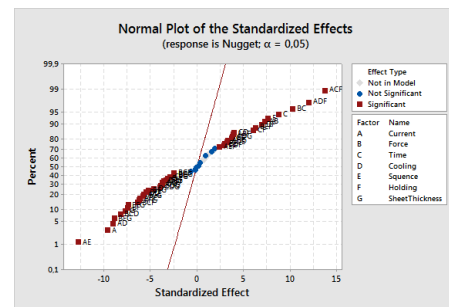


Figure 5. Percentage distribution of the effects of the weld parametres

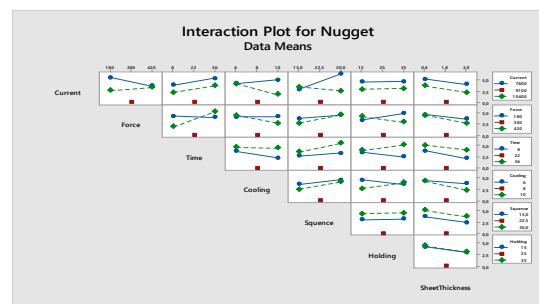


Figure 6. Interactive graph of welding parametres

In the Minitab, the mathematical model of the system was created as follows:

$$\begin{aligned} \text{Weld Nugget} = & [-70,3 + 0,01390 \text{ Current} - 0,1678 \text{ Force} - 1,799 \text{ Time} \\ & + 10,25 \text{ Cooling} + 0,891 \text{ Sequence} + 4,156 \text{ Holding} - 19,72 \text{ SheetThick} \\ & + 0,000009 \text{ Current*Force} + 0,000034 \text{ Current*Time} - 0,001484 \\ & \text{Current*Cooling} - 0,000197 \text{ Current*Sequence} - 0,000507 \text{ Current*Holding} \\ & + 0,000029 \text{ Current*SheetThick} + 0,005809 \text{ Force*Time} + 0,01413 \text{ Force*Cooling} \\ & + 0,000435 \text{ Force*Sequence} - 0,002555 \text{ Force*Holding} + 0,02007 \text{ Force*SheetThick} \\ & + 0,0717 \text{ Time*Cooling} + 0,04775 \text{ Time*Sequence} - 0,04365 \text{ Time*Holding} \\ & + 0,3685 \text{ Time*SheetThick} - 0,0865 \text{ Cooling*Sequence} - 0,3496 \text{ Cooling*Holding} \\ & - 0,123 \text{ Cooling*SheetThick} - 0,01809 \text{ Sequence*Holding} + 0,5262 \text{ Sequence*SheetThick} \\ & + 0,5950 \text{ Holding*SheetThick} - 0,000000 \text{ Current*Force*Time} - 0,000001 \text{ Current*Force*Cooling} \\ & + 0,000000 \text{ Current*Force*Holding} + 0,000002 \text{ Current*Force*SheetThick} - 0,000004 \text{ Current*Time*Sequence} \\ & + 0,000006 \text{ Current*Time*Holding} - 0,000023 \text{ Current*Time*SheetThick} + 0,000014 \text{ Current*Cooling*Sequence} \\ & + 0,000040 \text{ Current*Cooling*Holding} + 0,000104 \text{ Current*Cooling*SheetThick} + 0,000002 \text{ Current*Sequence*Holding} \\ & - 0,000034 \text{ Current*Holding*SheetThick} - 0,000211 \text{ Force*Time*Cooling} - 0,000017 \text{ Force*Time*Sequence} \\ & - 0,000033 \text{ Force*Time*Holding} - 0,000106 \text{ Force*Time*SheetThick} - 0,001166 \text{ Force*Cooling*SheetThick} \\ & + 0,000060 \text{ Force*Sequence*Holding} - 0,000709 \text{ Force*Sequence*SheetThick} - 0,000311 \text{ Force*Holding*SheetThick} \\ & + 0,000890 \text{ Time*Cooling*Holding} - 0,01024 \text{ Time*Cooling*SheetThick} - 0,000275 \text{ Time*Sequence*Holding} \\ & - 0,001501 \text{ Time*Holding*SheetThick} - 0,01721 \text{ Cooling*Sequence*SheetThick} - 0,007095 \text{ Sequence*Holding*SheetThick} - 3,736 \text{ Ct Pt}] \end{aligned} \quad (3)$$

Optimal values were used at certain intervals when determining the electrical resistance welding (ERW) parameters, Table 3.

Table 3. Minimum and max values of spot welding parameters (for 0.6-3mm sheets)

Parameters	min	max
Current (A)	7800	10400
Force (daN)	180	420
Time (cycle)	8	36
Cooling (cycle)	6	10
Sequence (cycle)	15	30
Holding (cycle)	15	35
SheetThic (mm)	0,6	3

20.3. Methods and Formulas for Prediction

While working here, the values of the weld nugget diameter in the model were estimated by increasing the values for each parameter from Minitab \ Stat \ DOE \ Factorial \ Predict into [14,15,16].

2.3.1 Fit

The fitted equation is:

$$\hat{y} = b_0 + b_{1x_1} + \dots + b_{kx_k} \quad (4)$$

\hat{y} : fitted response

x_k : k^{th} term. Each term can be a single predictor, a polynomial term, or an interaction term

b_k : estimate of k^{th} population regression coefficient

2.3.2 Prediction interval

$$\hat{y} \pm t_{(1-\alpha/2, n-p)} \mathbf{x} \mathbf{s}(\text{Pred}) \quad (5)$$

Here

$$\mathbf{s}(\text{Pred}) = \sqrt{s^2 (1 + x_0 (X \cdot X)^{-1} X_0)} \quad (6)$$

\hat{y} : fitted response value for a given set of predictor values

α : level of significance

n : number of observations

p : new value of the predictor

s^2 : mean square error

X : prediction matrix

X_0 : matrix of given predictor values

x_0 : transpose of the new vector of predictor values

2.3.2 Standard error of fitted value (SE Fit)

The standard error of the fitted value in a regression model with one predictor is:

$$SE \text{ Fit} = \sqrt{s^2 \left[\frac{1}{n} + \frac{(x_0 - \bar{x})^2}{\sum (x_i - \bar{x})^2} \right]} \quad (7)$$

The standard error of the fitted value in a regression model with more than one predictor is:

$$\sqrt{s^2 (X_0 (X \cdot X)^{-1} X_0)} \quad (8)$$

s^2 : mean square error

n : number of observations

x_0 : new value of the predictor

\bar{x} : mean of the predictor

x_i : i^{th} predictor value

X_0 : vector of values that produce the fitted values, one for each column in the design matrix, beginning with a 1 for the constant term

x_0 : transpose of the new vector of predictor values

X : design matrix

21. RESULTS

Here some parameters affect the weld nugget diameter, which is the output data, with a positive correlation, some with a negative correlation. While a single parameter is increased, other parameters are kept at a constant min value. The interaction of the spot welding parameters with the weld nugget diameter is given in Figures 7-13.

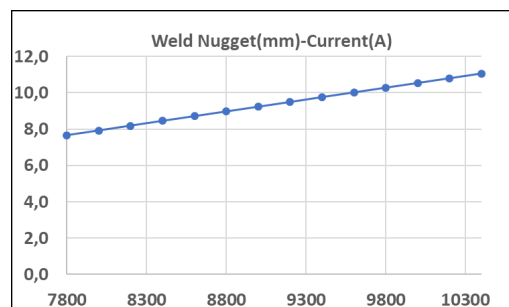


Figure 7. Weld nugget-current interaction

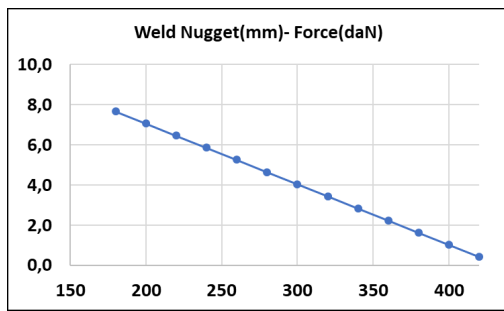


Figure 8. Welding nugget-force interaction

In the figure 7, it is seen that there is a positive correlation between current and nugget diameter. This situation is seen in the standardized effect graph that singularly, the current is a high factor. In the figure 8, it is seen that there is a negative correlation between the force and nugget diameter. This situation is seen in the standardized effect graph that singularly that the force is a not high factor.

In the figure 9, it is seen that there is a negative correlation between the time and nugget diameter. This situation is seen in the standardized effect graph that singularly, the time is a secondary factor. For this mathematical model, the minimum of the other factors was chosen, resulting in a nugget diameter negative effect. In the figure 10, it is seen that there is a negative correlation between the cooling and nugget diameter. This situation is seen in the standardized effect graph that singularly, the cooling is a very low impact factor.

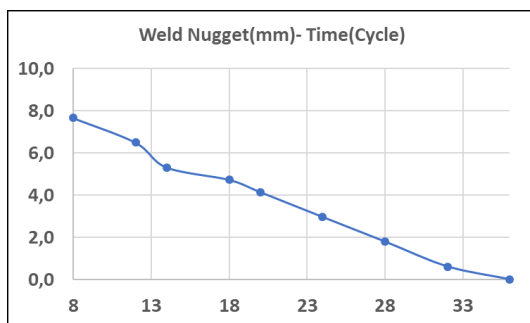


Figure 9. Weld nugget-time interaction

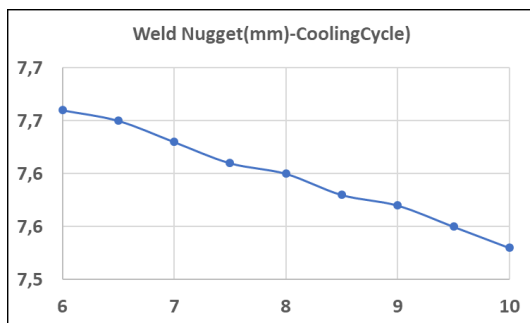


Figure 10. Weld nugget-cooling interaction

In the figure 11, it is seen that there is a negative correlation between the sequence and nugget diameter. This situation is seen in the standardized effect graph that singularly, the sequence is a secondary factor. For this mathematical model, the minimum of the other factors was chosen, resulting in a nugget diameter negative effect. In the figure 12, it is seen that there is a positive correlation between the holding and nugget diameter. This situation is seen in the standardized

effect graph that the holding is not a singularly factor. This factor acts on the system with the 2nd and 3rd combinations of other factors.

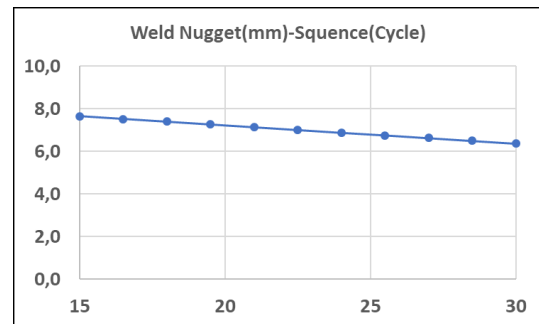


Figure 11. Weld nugget-sequene interaction

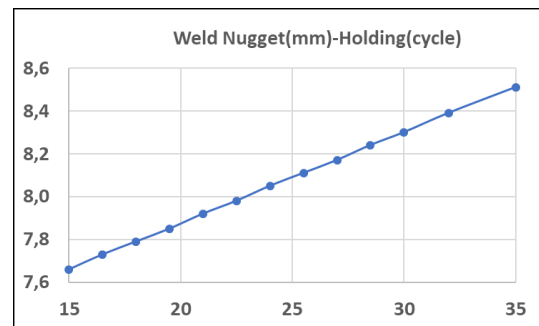


Figure 12. Weld nugget-holding interaction

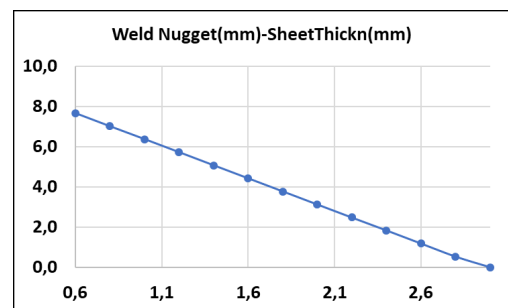


Figure 13. Weld nugget-sheet thickness interaction

In the figure 11, it is seen that there is a negative correlation between the sheet thickness and nugget diameter. This situation is seen in the standardized effect graph that singularly, sheet thickness is a secondary factor. For this mathematical model, the minimum of the other factors was chosen, resulting in a nugget diameter negative effect.

In addition, a study was conducted to test the accuracy of the model and randomly selected parameters were determined, see Table 4.

First of all, trial studies were made with randomly selected parameters in the field and the center diameter was measured. Y predict was made with the same parameters in the Minitab program and then regression analysis was applied by matching these values. The fitted line plot graph can be viewed graphically to view the relationship between a continuous predictive value and the opposite response. A linear, quadratic or cubic model can be selected for the data. A fitted line chart shows a scatter plot of the data with a regression line representing the regression equation. R2 or r2 and pronounced "R squared", is the proportion of the va-

Table 4. Random sample parameters, weld nugget diameters and Y predict values to verify

Blo-cks	Current	Force	Time	Coo-ling	Squen- ce	Holding	SheetT- hick	Weld Nugget	Y pre- dict
1	8800	180	25	10	25	20	1,5	4,74	4,5
2	7800	180	15	6	30	15	1,5	5,63	5,79
3	10400	180	36	10	20	35	1	7,49	9,29
4	7800	180	20	10	25	15	1	6,73	6,75
5	7800	180	25	10	20	35	1	6,01	5,98
6	9000	180	25	6	15	35	2,2	4,64	4,2
7	10000	180	36	10	30	35	2,2	7,28	7,09
8	10000	180	25	10	30	15	3	0,00	1,81
9	10200	180	22	6	15	35	3	0,00	1,9
10	7800	180	36	6	25	15	3	5,52	4,59
11	7800	180	20	10	20	35	0,8	5,90	5,85
12	10400	180	15	6	30	15	0,8	5,97	4,15
13	7800	180	20	10	15	35	0,8	5,21	5,39
14	10400	180	15	6	30	15	0,8	5,69	4,15
15	7800	180	36	6	30	35	2,4	7,21	7,17
16	7800	180	25	10	15	30	2,4	5,79	5,2
17	10000	250	10	6	15	30	1,5	4,35	3,57
18	10400	420	30	10	25	35	1	6,41	6,29
19	10400	420	30	6	30	35	2,2	5,15	3,57
20	10400	420	20	10	20	35	3	0,00	0,79
21	9800	420	25	10	25	15	2,4	0,00	0,76
22	7800	420	36	6	15	15	2,4	5,65	5,58
23	10400	420	36	6	15	35	2,4	6,12	6

riance in the dependent variable that is predictable from the independent variable(s). The adjusted R-squared is a modified version of R-squared that has been adjusted for the number of predictors in the model. In this study, RSq 91,7 and R Sq (adj) 91,4, which show a very high accuracy rate. [14].

Here, the most suitable model was found to be the cubic model as a result of experiments.

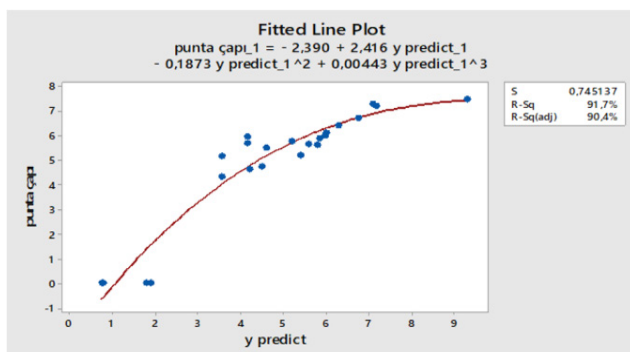


Figure 14. Regression plot of Minitab Y predict values with trial results

22. CONCLUSION

In solving current problems in the industry, math-based statistics programs are able to provide fast solutions, especially in the automotive sector. The statistical solutions of the Minitab program can be easily utilized in order to have more system inputs in the spot welding process and to obtain the optimum parameter.

Here, in determining the welding parameters, instead of determining the appropriate parameter by making many trials that will create high costs, statistics based Minitab program

was used. Following the experimental studies summarized above, it is possible to make the following inferences:

- Some of the weld parameters have a positive correlation for the spot diameter, while some have a negative correlation.
- According to this mathematical model, while the current value (A) and the pressure value (cycle) have a positive correlation; It has a negative correlation with force value (daN), time (cycle), cooling (cycle) and sheet thickness.
- In the last study, a high R-Sq and R-Sq (adj) values were obtained with randomly selected parameters, which gives information about the mathematical model accuracy we obtained.
- In general, in order to make long trials in parameter determination and / or to avoid problems in mass production, unnecessary costs are created by giving higher energy than necessary.

As a result; According to the results of the experimental studies summarized in this publication, it is possible to determine the spot welding parameters, which is done with a lot of trial and error, especially in the automotive sector, by entering the attached parameters in a statistical program, creating a mathematical model only once, and continuously. In this case, optimum parameters with much higher accuracy can be easily selected without unnecessary time and cost of trial parts.

With the DOE set of the design of experiments (DOE) in the Minitab, the effect of source welding nugget diameter parameter inputs was digitized and a mathematical model was created for the outputs of the study result.

REFERENCES

- [1] Yue X. K., Tong G. Q. Tong, Chen F., Ma X. L., Gao X. P. (2016), Optimal welding parameters for small-scale resistance spot welding with response surface methodology. Institute of Materials, Minerals and Mining, 22, 2. doi 10.1080/13621718.2016.1204799.
- [2] Boersch I., Füssel U., Gresch C., Großmann C., Hoffmann B.(2018). A non-destructive method to predict the welding spot diameter by monitoring process parameters. The International Journal of Advanced Manufacturing Technology, 99:1085–1099. doi 10.1007/s00170-016-9847-y.
- [3] Kim K.Y., and Ahmed F.(2018). Semantic weldability prediction with RSW quality dataset and knowledge construction. Advanced Engineering Informatics, 38:41-53. doi.org/10.1016/j.aei.2018.05.006.
- [4] Sheikhi M., Valaee T.M., Fattah-Alhosseini A., Usefifar G.R.(2017). Thermal modeling of resistance spot welding and prediction of weld microstructure. Metallurgical and Materials Transactions A: Physical Metallurgy and Materials Science, 48(11):5415-5423. doi: 10.1007/s11661-017-4314-4
- [5] Duric A., Klobčar D., Milčić D., Marković B.(2019). Parameter optimisation and failure load prediction of resistance spot welding of aluminium alloy 57547. Materials Science and Engineering, 659: 012042. doi:10.1088/1757-899X/659/1/012042,

- [6] Satonaka S., Kaieda K., Okamoto S. (2004). Prediction of tensile-shear strength of spot welds based on fracture modes. *Welding in the World: The International Journal of Materials Joining*, 48(5-6):39-45. doi.org/10.1007/BF03266430.
- [7] Hayat F. (2011). The effects of the welding current on heat input, nugget geometry, and the mechanical and fractural properties of resistance spot welding on Mg/Al dissimilar materials. *Materials and Design*, 32(4):2476-2484.
- [8] Kim T., Park H., Rhee S. (2005). Optimization of welding parameters for resistance spot welding of TRIP steel with response surface methodology. *Science and Technology of Welding and Joining*, 43(21):4643-4657. doi: 10.1080/00207540500137365.
- [9] Hiba K.H., Israa R.S., Iman A.Z. (2019). Prediction of spot welding parameters using fuzzy logic controlling. *Eastern-European Journal of Enterprise Technologies*, 5 (2):101. doi: 10.15587/1729-4061.2019.172642.
- [10] Pereda M., Santos J.I., Galán J.M., Martín Ó. (2015). Direct quality prediction in resistance spot welding process: Sensitivity, specificity and predictive accuracy comparative analysis. *Science and Technology of Welding and Joining*, 20(8):679-685. doi.org/10.1179/1362171815Y.0000000052.
- [11] Kemda B. V. Feujofack , Barka N., Jahazi M., Osmani D. (2015). Modeling of Phase Transformation Kinetics in Resistance Spot Welding and Investigation of Effect of Post Weld Heat Treatment on Weld Microstructure. *Metals and Materials International*. doi.org/10.1007/s12540-019-00486-x.
- [12] Manladan S.M. , Yusof F, Ramesh S., Fadzil M., Luo Z., Ao S. (2017). A review on resistance spot welding of aluminum alloys. *Int J Adv Manuf Technol*. doi 10.1007/s00170-016-9225-9
- [13] <https://support.minitab.com/en-us/minitab/18/help-and-how-to/modeling-statistics/regression/how-to/fit-regression-model/methods-and-formulas/stepwise/>, (2019), Date of Access: 06.11.2020, Topic: Stepwise.
- [14] <https://support.minitab.com/en-us/minitab/18/help-and-how-to/modeling-statistics/using-fitted-models/how-to/predict/methods-and-formulas/methods-and-formulas/>, (2019), Date of Access: 06.11.2020, Topic: Confidence interval.
- [15] <https://support.minitab.com/en-us/minitab/18/help-and-how-to/modeling-statistics/regression/how-to/fitted-line-plot/before-you-start/overview/>), (2019), Date of Access: 06.11.2020, Topic: Fitted line plot.

Annex A. ½ Division factorial experimental data (selected)

Std-Ordr	RunOrdr	CenterP	Blocks	Cur	Force	Time	Cooling	Squence	Holdding	SheetThicknln	Nugget
4	1	1	1	10400	420	8	6	15	15	3	0
64	2	1	1	10400	420	36	10	30	35	3	9,44
1	3	1	1	7800	180	8	6	15	15	3	0
65	4	0	1	9100	300	22	8	22,5	25	1,8	8,2
17	5	1	1	7800	180	8	6	30	15	0,6	4,81
48	6	1	1	10400	420	36	10	15	35	0,6	5,61
46	7	1	1	10400	180	36	10	15	35	3	8,36
25	8	1	1	7800	180	8	10	30	15	3	0
32	9	1	1	10400	420	36	10	30	15	0,6	7,64
29	10	1	1	7800	180	36	10	30	15	0,6	2,93
52	11	1	1	10400	420	8	6	30	35	3	0
34	12	1	1	10400	180	8	6	15	35	3	0
62	13	1	1	10400	180	36	10	30	35	0,6	6,09
16	14	1	1	10400	420	36	10	15	15	3	11,08
30	15	1	1	10400	180	36	10	30	15	3	8,96
9	16	1	1	7800	180	8	10	15	15	0,6	4,41
57	17	1	1	7800	180	8	10	30	35	0,6	0

Annex B. Input parameters and statistical impact analysis (backwise values)

Welding	DF	Adj SS	Adj MS	F-Value	P-Value	Kaynak	DF	Adj SS	Adj MS	F-Value	P-Value
Model	55	911,341	16,5698	35,02	0	Model	55	911,34	16,5698	35,02	0
Lineer	7	151,332	21,6189	45,69	0	Lineer	7	151,3	21,618	45,69	0
Current	1	43,858	43,857	92,68	0	3-Yollu Etkileşim	26	444,27	17,087	36,11	0
Force	1	4,736	4,7361	10,01	0,011	Current*Force*Time	1	17,925	17,92	37,88	0
Time	1	36,512	36,5118	77,16	0	Current*Force*Cooling	1	6,598	6,598	13,94	0,005
Cooling	1	10,288	10,288	21,74	0,001	Current*Force*Holdding	1	7,203	7,202	15,22	0,004
Squence	1	27,288	27,287	57,67	0	Current*Force*SheetThick	1	5,17	5,169	10,93	0,009
Holdding	1	0,375	0,3752	0,79	0,39	Current*Time*Squence	1	15,51	15,51	32,78	0
SheetThick	1	28,27	28,27	59,75	0	Current*Time*Holdding	1	88,97	88,97	188,02	0
2-Way Interaction	21	301,9	14,380	30,3	0	Current*Time*SheetThick	1	16,16	16,16	34,1	0
Current*Force	1	24,713	24,713	52,23	0	Current*Cooling*Squence	1	4,824	4,8235	10,19	0,011
Current*Time	1	0,006	0,0064	0,01	0,91	Current*Cooling*Holdding	1	67,692	67,6918	143,05	0
Current*Cooling	1	38,688	38,688	81,76	0	Current*Cooling*SheetThick	1	6,786	6,786	14,34	0,004
Current*Squence	1	76,891	76,891	162,49	0	Current*Squence*Holdding	1	2,612	2,6123	5,52	0,043
Current*Holdding	1	0,047	0,047	0,1	0,75	Current*Holdding*SheetThick	1	18,14	18,14	38,3	0
Current*SheetThick	1	0,248	0,247	0,52	0,48	Force*Time*Cooling	1	32,22	32,21	68,0	0
Force*Time	1	49,93	49,93	105,5	0	Force*Time*Squence	1	2,873	2,873	6,07	0,03
Force*Cooling	1	14,39	14,39	30,42	0	Force*Time*Holdding	1	19,393	19,39	40,98	0
Force*Squence	1	4,08	4,0804	8,62	0,017	Force*Time*SheetThick	1	2,928	2,928	6,19	0,035
Force*Holdding	1	26,458	26,4582	55,91	0	Force*Cooling*SheetThick	1	7,216	7,215	15,25	0,004
Force*SheetThick	1	3,041	3,040	6,43	0,032	Force*Holdding*Holdding	1	18,469	18,46	39,03	0
Time*Cooling	1	7,439	7,439	15,72	0,003	Force*Squence*SheetThick	1	37,546	37,54	79,35	0
Time*Squence	1	6,433	6,4326	13,59	0,005	Force*Holdding*SheetThick	1	12,843	12,84	27,14	0,001
Time*Holdding	1	17,26	17,26	36,48	0	Time*Cooling*Holdding	1	3,97	3,970	8,39	0,018
Time*SheetThick	1	1,108	1,107	2,34	0,16	Time*Cooling*SheetThick	1	7,576	7,576	16,01	0,003
Soguma*Yaklas	1	1,616	1,616	3,42	0,098	Time*Squence*Holdding	1	5,319	5,318	11,24	0,008
Soguma*Holdding	1	22,84	22,84	48,29	0	Time*Holdding*SheetThick	1	4,07	4,070	8,6	0,017
Cooling*SheetThick	1	6,747	6,747	14,26	0,004	Soguma*Holdding*SheetThick	1	6,144	6,144	12,98	0,006
Holdding*Holdding	1	0,007	0,006	0,01	0,90	Yaklaşm*Holdding*SheetThick	1	26,099	26,09	55,16	0
Holdding*SheetThick	1	0,014	0,013	0,03	0,87	Eğrilik	1	13,74	13,74	29,04	0
Holdding*SheetThick	1	0,024	0,024	0,05	0,82	Error	9	4,259	0,473		
						Total	64	915,6			



Fibre Volume Fraction and Impact Strength Analysis of Reinforced Polyester Composites

Dickson David Olodu^{1*} , Osagie Ihenyen² 

¹Department of Mechanical Engineering, Faculty of Engineering, Benson Idahosa University, PMB 1100, Benin City, Edo State, Nigeria

²Department of Production Engineering, Faculty of Engineering, University Benin, Benin City, Edo State, Nigeria

Abstract

Improper fibre volume analyses in most reinforced composites poses great challenges in polymer industries which results to the production of composites with low mechanical strength. This study investigates the fibre volume fraction and impact strength analysis of reinforced polyester composites. In this study, E-Glass fibres (hard and soft mat) were mixed with polyester at different composition by volume. The E-glass serves as reinforcement to the polyester, fourteen test specimens of the reinforced composites were developed with each of them having dimension of 210mm length, 150mm width and 50mm thickness respectively. The properties of the developed reinforced composites such as volume fraction, impact energy, and impact strength were analysed from the values obtained from compact tension and Charpy impact test respectively. The results obtained shows that the effective thickness of the developed reinforced composites ranged from 60mm to 100mm at fibre fraction which ranges from 0.32 to 0.50. The results obtained also shows that the specimens containing woven roving have greater resistance to fracture and impact damages due to high fibre volume fraction. Hence, the laminates impact strength is a function of its fibre volume fraction.

Keywords: E-glass fibre, Fibre Volume Fraction, Impact Strength, Reinforced Polyester Composites.

23. INTRODUCTION

Inadequate analysis of the production factors in composite production poses tremendous challenges. Fibre volume fraction and impact strength are major factors whose effects on composite such as reinforced polyester composites cannot be emphasised.

It has been observed that typical events such as cracking of coating, matrix, fibre exposure and breaks, and instantaneous fibre/matrix debonding in reinforced composite material are influencing conditions for which dominate crack growth, thereby posing a threat to the impact performance of these structures in service. Fracture events are often associated with finite increase in fracture area which leads to eventual catastrophic failure. These failures are imminently progressive due to the absence of sufficient and effective reinforcement, which prevent crack propagation through fibre bridging and crack arrest [1, 2].

Kao [3] examined toughness fracture of laminated composites, he observed that the energy required before fracture can take place is unexpectedly high, which is about five times larger than the separated Aluminium foil layer. Other

investigations were also carried out to estimate the microstructure fracture mechanism which was applied to study the limited stability of fracture mechanism [4, 5]. Williams [6] in his analysis of the fracture mechanics of composites failure reviewed how fracture mechanism can be applied to the various fracture modes which was observed in composites. From his investigation, It was observed that the conventional methods may be used for short-fibre composites, he also observed that oriented laminates undergo delamination which is often parallel to the applied loads. In his study, energy release rate methods were used to analyse these failures. Pahizgar et al. [7] applied linear elastic fracture mechanics to study orthotropic materials. It was shown that the fracture toughness of unidirectional composites was independent of the crack length but dependent on crack-fibre orientation. To verify these claims, glass epoxy material was used. The fracture toughness for different crack-fibre orientations were obtained by utilising Solid Sap finite element program and compact tension specimens. Hence, an empirical formula relating to the fracture toughness of the material for different crack-fibre orientation was found. Mandel et al., [8] examined the micromechanical growth of crack in

* Corresponding author
Email: dolodu@biu.edu.ng



fibre reinforced materials using a 2-D, in their study; micro-mechanical finite element was used to investigate the stress conditions near the crack tip. The mechanical properties, interface between the fibres/matrix material and the geometry were considered. A close agreement between finite element and experimental values for the load required for the initiation of crack growth in the material were obtained. According to them, the arrest by the fibres showed that micromechanical finite element studies are applicable for the development of engineering models for fracture toughness of fibre reinforced material. It was also shown that the presence of high modulus fibres could significantly reduce the opening mode (mode-I) stresses in the matrix material near the crack tip and could result in crack arrest resulting to an increase in the effective fracture toughness. Further, it was noted that the shear stresses in the matrix material adjacent to the fibre and bond stresses between the fibre and matrix material are larger for a shear mode loading than for an opening mode loading. Although the stresses do not directly result crack growth, they were observed to cause fibre delamination which in turn could result in unstable crack growth. Garo and Trotman [9] used the concept of linear elastic fracture mechanics to study the effect of water and thickness on the fracture behaviour of fibre glass composite. It was found from their work that the stress intensity factor and fracture resistance decreased considerably due to the presence of water in such materials. Also, it was found that thickness has an effect of increasing the fracture resistance and stress intensity factor; hence, analytical relations for the R-curves were presented to represent the behaviours of the material.

This research therefore focused on fibre volume fraction and impact strength analysis of reinforced polyester composites.

24. MATERIALS AND METHODS

24.1. Materials

Studies were carried out on samples fabricated by randomly varying plies of reinforcements in form of woven roving, hard and soft E-glass fibre mats, combined in unsaturated polyester resin (specific gravity 1.12, viscosity of 65cps and gel time of 25 min) matrix. The catalyst and accelerator used were methyl ethyl ketone peroxide (MEKP) and cobalt respectively due to their compatibility in polyester as curing agents at ambient temperature condition.

24.2. Reinforced Polyester Composite Specimen Manufacture and Preparation

The hand lay-up method was used for the production of 14 samples which consist of the randomly varied E-glass fibre reinforcement plies, neatly laid in an already prepared mould measuring $210\text{mm} \times 150\text{mm} \times 50\text{mm}$. Hence, the reinforcement was impregnated with catalysed polyester resin, and allowed for a period of one month to completely cure at ambient condition. The samples for the tests were cut into 28 specimens, for which 14 samples were compact test (CT)

specimens used for fracture mechanics test and the other 14 specimens were for impact tests respectively, using a hack saw cutting blade and tested in accordance with the ASTM and ISO standard for fracture mechanics and impact tests for composite materials respectively.

Table 1. The Table Below Shows the Variation Order in which Reinforcing Plies were Combined in the Specimen for the Fracture Mechanics and Impact Test Analyses.

Material Specimen	Reinforcement Composition	Geometry of Samples in millimetre (mm)		
		Length (L)	Width (W)	Thickness (t)
A	One ply of soft mat Two plies of woven roving One ply of soft mat	210	150	4.4
B	One ply of woven roving Two plies of soft mat One ply of woven roving	210	150	5.2
C	One ply of (42.7g) hard mat Two plies of woven roving	210	150	4.5
D.	One ply of woven roving Two plies of (42.7g) hard mat One ply of woven roving	210	150	6.4
E	One ply of soft mat Two plies of (42.7g) hard mat One ply of soft mat	210	150	7.1
F	One ply of (42.7g) hard mat Two plies of soft mat One ply of (42.7g) hard mat	210	150	5.7
G	Five plies of woven roving	210	150	7.7
H	Twelve plies of soft mat	210	150	8.4
I	Eight plies of (42.7g) hard mat	210	150	10.3
J	One ply of soft mat One ply of woven roving One ply of soft mat	210	150	6.8
K	One ply of soft mat Two plies of (42.7g) hard mat One ply of woven roving Two plies of (42.7g) hard mat One ply of soft mat	210	150	7.32
L	Two plies of soft mat Two plies of woven roving Two plies of soft mat	210	150	7.2
M	Two plies of woven roving Four plies of soft mat Two plies of woven roving	210	150	10.2
N	Two plies of (42.7g) hard mat Four plies of soft mat Two plies of woven roving	210	150	13.5

24.3. Fracture Mechanics Assumptions in Reinforced Composite Analysis

The following assumptions were made in this study;

- i) Resin interlayer is isotropic and has uniform thickness.
- ii) The plies or layers are perfectly bonded in the laminate everywhere except in the region where a flaw is initiated or present from the surface notched tip.
- iii) There is perfect bonding between the resin and the fibre.
- iv) The resin and the fibres are experiencing the same stress

due to the applied impact force.

v) Crack tip have zero radius.

24.4. Areal Weight (A_w) and Fibre Volume Fraction (V_f) Data Analysis

Material thickness for a reinforced composite laminates are function of the amount of resin included in the composite. This illustrates the fibre volume fraction as a characteristic of its areal weight (A_w). The areal weight is expressed in g of 1 m² of the reinforced mat; the areal weight depends on fibre density, bundle size, weave style and so on. Using the equation 1, the fibre volume fraction, V_f can be obtained if the fibre mass m , area, A , thickness of laminate, B and numbers of plies, n are known. Also, area weight, A_w can be evaluated using equation 1. This relationship between laminate thickness and fibre volume requires that the fibre density be known also before using Equation 1.

$$V_f = \frac{n A_w}{\rho_f B} \tag{1}$$

24.5. The Charpy Impact Test

The Charpy impact test was used to measure the energy absorption capacity of the reinforced polyester composite materials. A notched bar of reinforced composite specimen was supported as a simple beam so that the vertical faces are positioned away from the point of impact. The test specimens are trucked at the middle with a hammer which is incorporated on the test equipment. The impact test had a setup similar to the 3PB test and this is the most appropriate for the composite materials which damage and fracture in a brittle manner because of the presence of micro defect or a surface scratch; and the stress concentrated at these regions will accelerate the failure rate under sudden impact force. Moreover, the energy absorbed by the blow in machine was determined by a measuring device incorporated in the machine.

24.6. Experimental Procedure for Impact Strength Determination

Before the conduct of the Charpy impact test, the specimen geometry was marked out on the plate using the dimensions specified in the design. The specimens were cut, after which, the specimen was position on the anvil. The right position of the impactor (impact head) and the height of the pendulum were set. After securing the specimen, the pendulum was raised to position and allowed to freely swing towards the specimen to impact it to breaking, because the test was a destructive test similar to the fracture mechanics test.

In this study, the energy required to break test specimen was determined from the data recorded on the metering device on the machine. Furthermore, the impact energy for a composite material using fracture mechanics approach was obtained using Equation 2 [10, 11].

$$U = \frac{E}{\phi b(d-c)} \tag{2}$$

Where U= Impact Energy; E=Energy in kJ/m² or ft.lb/in² registered in the test specimen; b= Specimen breadth; d= Specimen Depth; c and ϕ are calibration factors which depend on specimen, crack dimension and compliance [12].

25. RESULTS AND DISCUSSIONS

25.1. Fibre Volume Fraction Analysis

The fibre volume fraction of the reinforcement used in the laminate were obtained using Equation 1, the results were presented on Table 2a and 2b respectively.

Table 2a. Reinforcement Volume Fraction Data Analysis

Reinforcement	Woven Roving	Hard Mat	Soft Mat
Mass, m (g)	1000	1000	200
Area, A (m ²)	1.50	2.268	5.67
Fibre Density, ρ_f (g/m ³)	1.11E+06	1.10E+06	1.76E+05
Areal Weight, A_w (g/m ²)	666.67	440.92	35.27

Table 2b. Reinforcement Volume Fraction Data Analysis

Specimen	Woven Roving	Hard Mat	Soft Mat	No. of Plies	Thickness, B (mm)	Volume Fraction, V_f
A	2	1	1	4	4.4	0.47
B	1	2	1	4	5.2	0.35
C	2	1	Nil	3	4.5	0.36
D	2	Nil	2	4	6.4	0.34
E	Nil	2	2	4	7.1	0.21
F	Nil	2	2	4	5.7	0.21
G	5	Nil	Nil	5	7.7	0.39
H	Nil	12	Nil	12	8.4	0.57
I	Nil	Nil	8	8	10.3	0.16
J	1	1	1	3	6.8	0.21
K	1	2	4	7	7.32	0.4
L	2	2	2	6	7.2	0.41
M	4	4	Nil	8	10.2	0.39
N	2	4	2	8	13.5	0.27

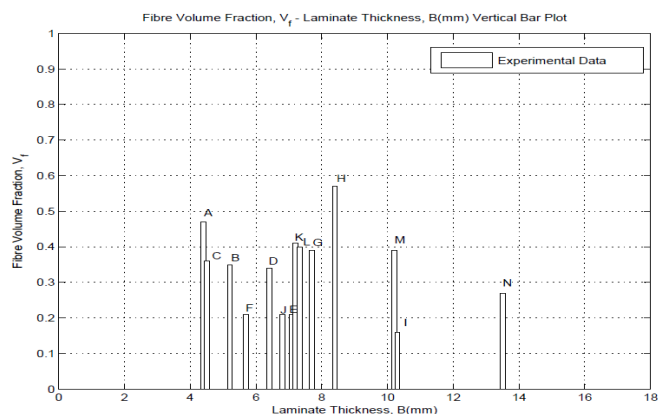


Figure 1. Bar Plot of Fibre Volume Fraction of Laminates against Test Specimen Thickness

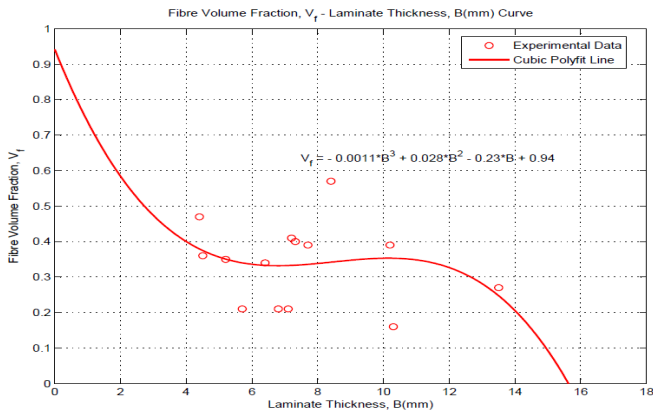


Figure 2. Graph of Fibre Volume Fraction of Laminates against Specimen Thickness Profile

Table 3. Impact Results for Specimens A to N using the Charpy Impact Test Machine

Composite Samples	Thickness ,B (mm)	No. of Plies	Volume Fraction, V _f	Impact Energy, E (J)	Impact Strength, U (J/mm ²)
A	4.4	4	0.47	87	6.2
B	5.2	4	0.35	75	4.51
C	4.5	3	0.36	72	5
D	6.4	4	0.34	78	3.75
E	7.1	4	0.21	84	3.7
F	5.7	4	0.21	87	4.77
G	7.7	5	0.39	108	4.38
H	8.4	12	0.57	96	3.57
I	10.3	8	0.16	39	1.18
J	6.8	3	0.21	60	2.76
K	7.32	7	0.4	72	3.07
L	7.2	6	0.41	120	5.21
M	10.2	8	0.39	155	4.75
N	13.5	8	0.27	130	3.61

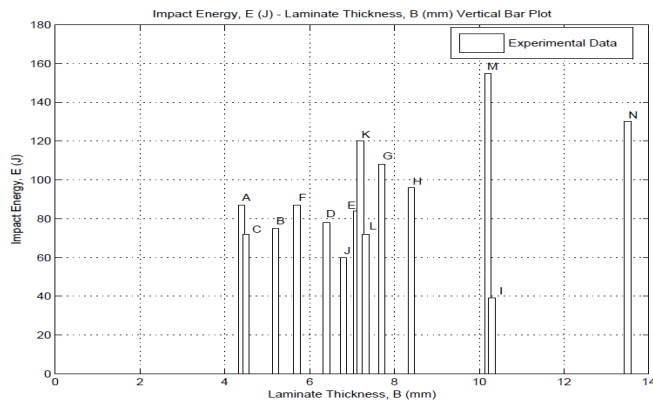


Figure 4. Bar Plot of Impact Energy of Laminates for Various Specimen Thicknesses

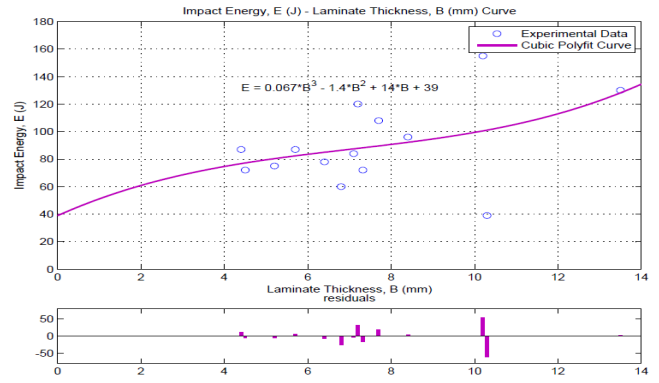


Figure 5. Impact Energy of Laminates versus Specimen Thicknesses Curve

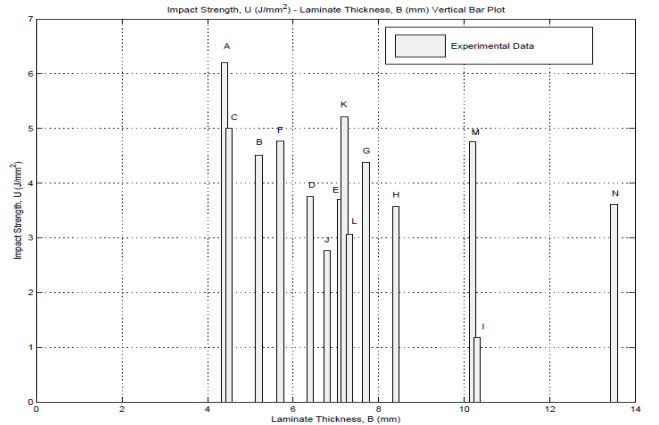


Figure 6. Bar Plot for Impact Strength of Laminates for Various Specimen Thicknesses

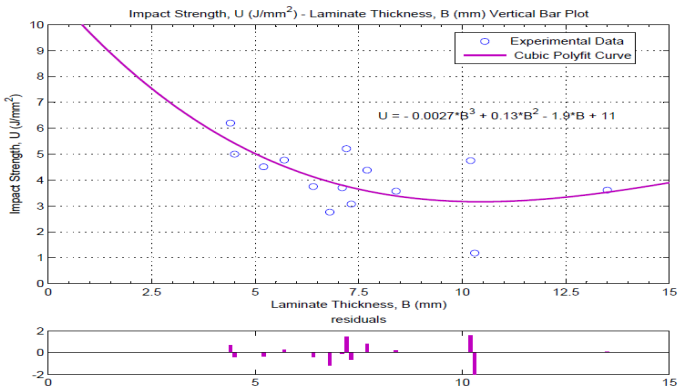


Figure 7. Impact Strength of Laminates versus Specimen Thicknesses Curve

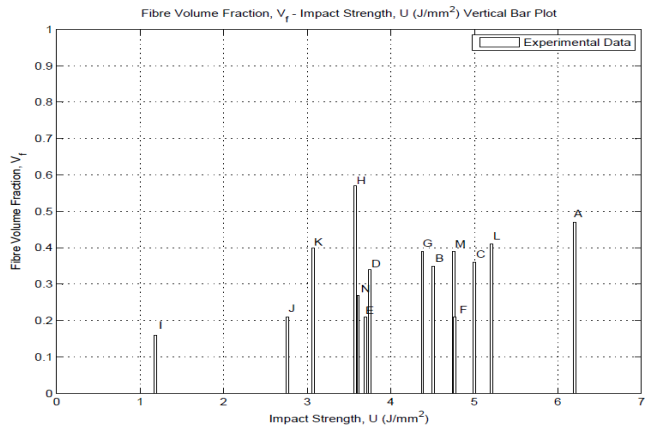


Figure 8. Bar Plot for Fibre Volume Fraction of Laminates versus Impact Strength

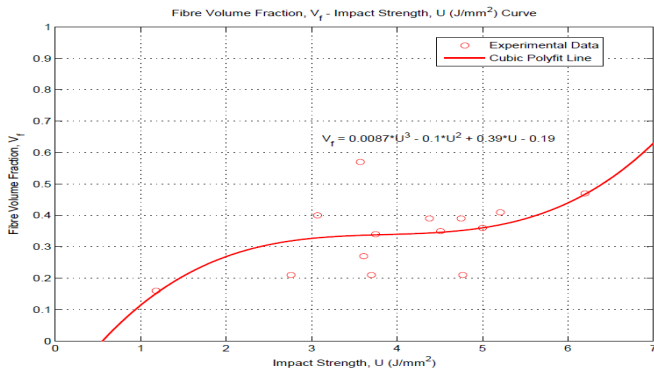


Figure 9: Fibre Volume Fraction of laminates versus impact strength curve

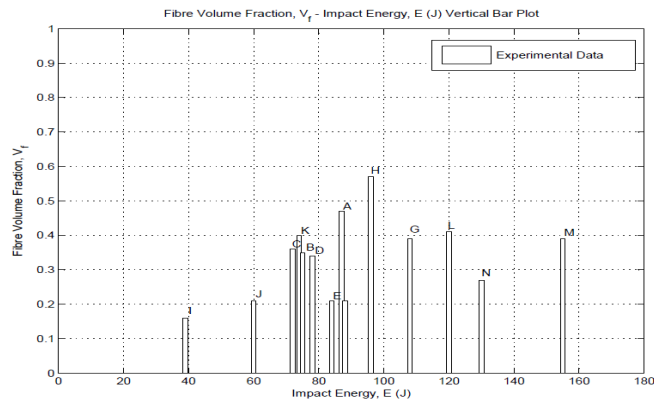


Figure 10: Bar Plot of Fibre Volume Fraction of Laminates Versus Impact Energy

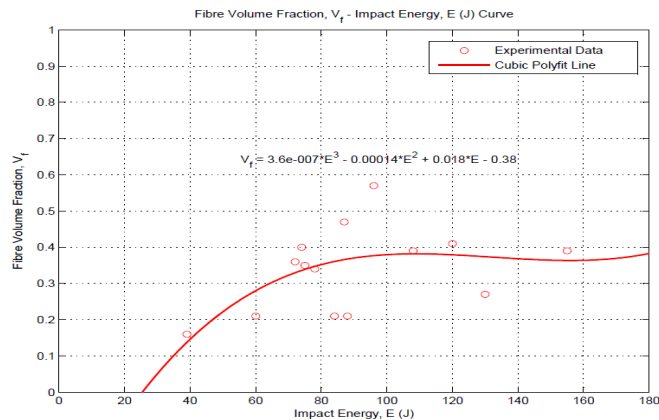


Figure 11: Fibre Volume Fraction of Laminates versus Impact Energy Curve

25.2. Discussion of Results

From the behaviour of the above bar plot and curve presented in figures 1 and 2 respectively, it was clear that as the fibre volume fraction is reduced, the thickness also shrinks which could be established that the fibre volume fraction determines the laminate thickness.

Using the Charpy impact machine, the impact strength was determined for the specimens containing varied volume fraction of reinforcements. It was observed that those specimens containing woven roving form of reinforcement had better impact resistance when compared with those that contained only soft and hard mat, irrespective of the volume fraction in which they were present. This was found to be as a result of the form, integrity, the virtue of the volume to

compaction ratio, and their filament’s length (Table 3). This observation was a testimony to the fact that for a composite structure to possess adequate impact properties, the fibre length should be considered and ensured it is sufficiently long enough to resist failure and ensure good performance. Hence, this will satisfy the purpose of the impact test to measure the toughness and energy absorption capacity of the material without failure under a single blow.

Figure 4 and 5 shows the experimental result curve for the impact energy versus specimen thickness, and from the curve, it was observed that the thickness and Glass fibre content plays a vital role in the impact strength of laminates with the exception of specimens E, L, J, I which were low in impact energy as a result of fibre composition. Hence, it can be said that the more the woven glass fabric percentage, the more the impact toughness. It was also observed that the impact energy increased significantly when the specimen thickness increased, this trend is true irrespective of laminate thickness, but depend on the fibre form and volume fraction. The maximum impact energy for specimen M is 155J. The level of increase in impact energy for each specimen depends on the fibre form rather than on fibre volume fraction. However, this is mainly due to increased number of load bearing fibres at the critical section compared to laminates which have low strength fibre composition. Moreover, the high impact energy in some test specimen such as specimen M is due to increased thickness, high fibre volume fraction and increased number of plies. This simply means that proper combination of these factors; specimen thickness, fibre volume fraction and number of plies can affect the results of impact energy. This made the results obtained from this experiment different from past literatures.

Figure 6 shows that the impact strength of the specimens is not a function of the thickness as some specimens with greater thickness had low impact strength, but it was a function of the reinforcement combinations as those with woven roving mats performed better under sudden impact force. But from figure 7, the trend of the curve was observed to drop with increasing thickness, which further proved that the impact performance is dependent on reinforcement combinations of the glass fibre mats used for the manufacturing of the specimens.

From figures 8 and 9, it is shown clearly that the fibre volume fracture has a significant contribution to the impact performance of reinforced polyester composites when exposed to sudden impact load. The curve indicated an increase in impact strength as the fibre volume fraction rises.

From the data analysis of the fibre volume fraction, the behaviour of the profile in figure 11 indicated a gradual increase in impact energy as the fibre volume fraction increased. This is to say that, considering the specimens used in this investigation, as the sudden impact force was applied, there was a rise in resistance as fibre volume fraction increased, but, later on, the deviation from what appears to be cons-

tant volume fraction line was minimal with in continuous increased in impact strength. This suggests that there exists a fibre volume fraction at which laminate possesses ultimate impact strength (figure 10).

26. CONCLUSIONS

Fibre volume fraction and impact strength analysis of reinforced polyester composites had been achieved. In this study, the thickness of the developed reinforced polyester specimens were varied using the fibre volume fraction. The effects of specimen thickness and fibre volume fraction on impact responses and fracture mechanism for each developed composite were investigated. The results obtained shows that the effective thickness of the developed reinforced composites ranges from 60mm to 100mm at fibre fraction which ranges from 0.32 to 0.50. The results obtained also shows that the specimens containing woven roving have greater resistance to fracture and impact damages due to high fibre volume fraction. Hence, the laminates impact strength is a function of its fibre volume fraction. The results obtained also shows that the thicker specimens based on the presence of woven roving reinforcement the greater the impact resistance to delamination and crack propagation for the same impact area. In other words, for identical sudden impact force, the damage and fracture areas of the thicker plates were much smaller than those of the thin plates.

Conflicts of Interest

There is no conflict of interest in this research article.

REFERENCES

- [1] Osaretin, M.O. and Olodu, D.D. Stress Mechanics of Reinforced Polyester Composites. *International Journal of Engineering and Innovative Research*. 2021, 3(1); 39-54
- [2] Ladeveze, P. and Le Dantec, E. Damage Modelling of the Elementary Ply for Laminated Composites. *Composite Science and Technology Journal*. 1992, 43: 257 – 267.
- [3] Kao, W. S. Fracture Toughness of a Laminated Composite. *Fracture of Polymers, Composites and Adhesives II*, Elsevier. 2003, 355-364
- [4] Mueller, D. H. and Krobjilowski, A. Improving the Impact Strength of Natural Fibre Reinforced Composites By Specifically Designed Materials and Process Parameter. *International Nonwovens Journal*. 2004, 13(4): 31–38.
- [5] Silva, J. F., Vieira, P., Morais, A. B., Marques, A. T. and De Castro, P. M. S. T. Mode-II Fracture Toughness of Glass Reinforced Composites. *Universidade de Aveiro, Campus Santiago, Aveiro, Portugal*. 2007, 38-50.
- [6] Williams, J. G. *Linear Fracture Mechanics*. *Advances in Polymer Science*, Springer Verlag, Berlin, Heidelberg, New York. 1978, 27: 69 – 82.
- [7] Parhizgar, S., Zachary, L. W. and Sun, C. T. Application of the Principle of Linear Fracture Mechanics to the Composite Materials. *International Journal of Fracture Mechanics*. 1982, 20: 3-15.
- [8] Mandel, J. A., Pack, S. C. and Tarazi, S. Micromechanical Studies of Crack Growth in Fibre Reinforced Materials. *Engineering Fracture Mechanics*. 1982, 16: 741-754.
- [9] Garo, A. C. and Trotman C. K. Effect of Water on Fracture Toughness of Reinforced Composites. *Engineering Fracture Mechanics Journal*. 1980, 24(2): 34-45/
- [10] Radif, Z. S. and Ali, A. Fracture Toughness of Kenaf Mat Reinforced Polyester Composite. *Pertanika Journal of Science and Technology*. 2001, 99(1): 177 – 187.
- [11] Idicula, M., Joseph, K. and Thomas, S. Mechanical Performance of Short Banana/Sisal Hybrid Fibre Polyester Composite. *Journal of Reinforced Plastics and Composites*. 2009, 29(1), 12 – 29
- [12] Liu, Q., Hughes, M., The Fracture Behaviour and Toughness of Woven Flax Fibre reinforced epoxy Composites. *Composites Part A: Applied Science and Manufacturing*, 2008, 8(4), 23-30.



Thermal Comfort in an Office Room Using Square Diffuser

Alper Yildirim^{1*} , Coskun Ozalp² 

¹Osmaniye Korkut Ata University, Department of Machinery and Metal Technology, Osmaniye, Turkey

²Osmaniye Korkut Ata University, Engineering Faculty, Energy System Eng. Dept., Osmaniye, Turkey

Abstract

The office is an important part of daily life, people spend most of their time working inside of the office and thus the quality of the indoor air environment is a significant factor affecting the productivity and happiness of office users. Many factors influence the pattern of airflow: indoor air quality, thermal comfort and energy saving in an office room. In this study, the effects of the square diffusers on thermal comfort investigated numerically for an office room. Numerical research was subsequently carried out using the validated CFD (computational fluid dynamics) model. This model solved the continuity, energy conservation and momentum equations in addition to $k-\epsilon$ model equation for turbulence modelling. Predicted Percentage of Dissatisfied (PPD) is a frequently used tool for assessing human comfort rating. A PPD based control HVAC (Heating, Ventilating and Air Conditioning) system has the potential to provide enhanced thermal comfort inside a location by taking into consideration all main thermal comfort variables. The CFD results revealed that the PPD values in the room varies on average between 10% and 20% and thus thermal conditions occurred according to ASHRAE standards in the model office room with a square diffuser.

Keywords: CFD, Diffuser, HVAC, PMV, PPD, Thermal Comfort

27. INTRODUCTION

The Heating, Ventilating and Air Conditioning (HVAC) system's most critical goal is to develop a comfortable and healthy environment and reduce indoor pollutant concentration. An effective design of HVAC system involves the appropriate installation of the exhaust and supply outlet with regard to a room's geometry configuration, distribution of indoor thermal conditions and indoor heat sources. The ventilation efficiency and energy saving in most air distribution systems are greatly affected by the supply, return and exhaust diffuser location arrangements [1]. If the ventilation process is incomplete or incorrect in the occupied zone, there is a possibility that people in these places may lose their working efficiency and even deteriorate their health. The first condition to be considered in order to prevent this unwanted possibility is the cleanliness of the air. Air temperature, air distribution and velocity in the area are other important elements. Thermal comfort is the definition of the comfort of the people in the occupied zone while continuing their physical or mental activities under physical factors such as temperature, humidity and air circulation. Thermal comfort is felt after a certain period of time in the occupied zone [2]. The main factors affecting thermal comfort conditions are given below [3].

27.1. Personal Factors

Clothing: The resistance given by clothing to reasonable heat gain transfer.

Metabolic heat: It is the heat person produce by physical activity. The stationary person will tends to feel colder than the exercise person. [4].

27.2. Environmental Factors

Air velocity: The velocity of the air that the person touches. The faster the air moves, the higher the heat exchange between the air and the person.

Air Temperature: The temperature of the air around the body (dry-bulb).

Radiant Temperature: Expressed as the temperature of an environment (including heat generating equipment, surfaces, sky and sun). This is commonly defined as the mean radiant temperature (MRT) and any strong unidirectional radiation such as radiation from the sun.

Air humidity: It is defined as the ratio of water vapor to a given volume of air.

Awad et al. [5] used various exhaust diffuser locations to investigate velocity distribution and air flow patterns. The

* Corresponding author
Email: alperyildirim@osmaniye.edu.tr



results revealed that the location of the exhaust diffuser had a significant impact on the level of the layers of thermal stratification that influenced the cooling coil load as a result. Cheng et al.[6] reported that 20.8% of energy savings were achieved when the supply inlet was located at the floor level and the return outlet was located at the occupied level. They also found that the distribution of the supply diffuser improved energy saving and indoor thermal comfort in the occupied zone. Chung and Kuo [7] used the effect of the supply and outlet diffusers places on indoor thermal comfort using various ventilation strategies in the occupied zone. Based on simulation result, they discovered that the longer supply air throw in the occupied region is, a much better the indoor thermal comfort obtained. He et al. [8] noted that the position of the exhaust vent did not considerably influence the pattern of air flow, but could considerable affect the level of indoor exposure.

The sensitivity of the PMV (Predicted Mean Vote) index was analyzed by d'Ambrosio Alfano et al. [9] for the accuracy of its six independent variables, including air temperature, mean radiant temperature, air velocity, metabolic rate, insulation of the clothing and relative humidity. The authors found that due to a substantial Sensitivity of PMV that mostly reaches or exceeds the A class width (± 0.20), the PMV comfort ranges published in the EN 15251 and ISO 7730 standards should be extended to permit for a more sustainable category of thermal indoor environment. In order to optimize the thermal environment in a train station with a high ceiling. Li et al. [10] evaluated various air distribution models. The numerical result showed that satisfactory thermal comfort was achieved using air distribution design and a stratified supplying air at midheight horizontally in the occupied region. Similarly, Han and Gu [11] conducted a numerical study of the thermal environment at Beijing International Airport. They reported that a satisfactory thermal environment was achieved in the occupied zone through the use of stratified air distribution in the terminal building. Three ventilation techniques (i.e. natural ventilation [NV], air conditioning [AC], and hybrid [HB]) were used by Lau et al. [12] to evaluate the thermal comfort of the occupants of educational facilities on a tropical university campus. Results showed that HB spaces have a significant advantage in terms of a higher rates of neutral thermal sensation votes, an overall level of thermal comfort, and temperature satisfaction levels over NV and AC spaces. It was also discovered, as compared to those in the AC spaces, occupants in NV and HB spaces maintained higher comfort temperatures and they may tolerate a larger range of acceptable temperatures. The goal of Khalil et al. [13]. is to evaluate and analyze the indoor thermal comfort in different cases in order to assign the correct inlet air temperature to the operating room. For this study, the PMV and PPD (Predicted Percentage of Dissatisfied) models in accordance with ISO 7730 were used. The results showed that inlet air temperature has a slight effect on the airflow patterns and air velocities inside the operating room at the same air change rate.

The PMV is one of the most well-known thermal comfort models. The standards firstly implemented by Fanger, ASHRAE 55 and ISO 7730 are based on that model. The PMV is an index that forecasts the mean value of the votes of a large number of people on a 7-point thermal sensation scale. It is based on the heat balance of the human body. When internal heat production is equal to the loss of heat to the environment in the body, thermal balance is achieved. Thermal sensitivity scale measurement ranges for thermal comfort are shown in Table 1 and numerical values of PMV and PPD (Predicted Percentage Dissatisfied) are seen in Figure 1. PPD indicates the estimated number of person who are not satisfied with their comfort condition[3]. As seen in figure 1, the suggested thermal limit for the 7-point PMV scale is between -0.5 and 0.5 in order to meet ASHRAE 55 requirements. Depending on the calculated PMV, the PPD may range from 5 percent to 100 percent. In order for the comfort ranges to comply with the standards, no space occupied point should be more than 20% PPD.

In this study, thermal comfort conditions were investigated by using a square diffuser in the office room.

Table 1. PMV index [14]

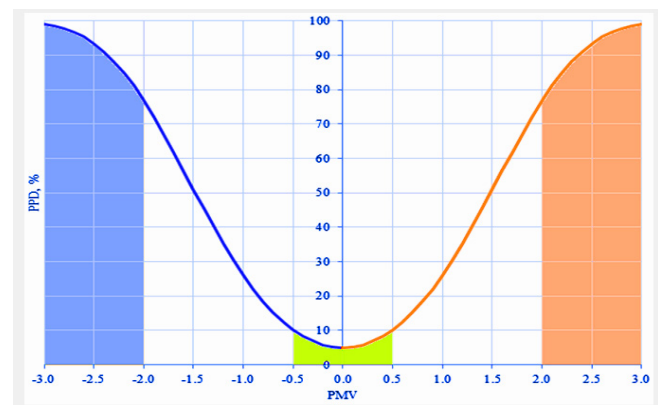
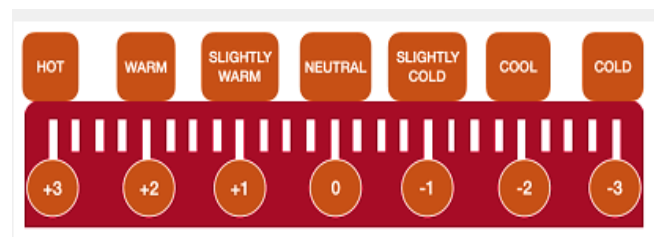


Figure 1. PPD numerical as a function of PMV values [15] to create a suitable thermal condition in avoiding occupant dissatisfaction, adverse effect on their productivity and overall building performance. Approach: Assessment was conducted using Babuc-A (Portable air quality monitor)

28. 2. MATERIAL AND METHODS

28.1. 2.1 Mathematical Models

In present study, commercial package “FLUENT 18” is used to solve and transform the partial differential equations based on the “SIMPLE” algorithm. More dense mesh structure was created in regions where velocity and temperature changes are high. For this reason, the exit part of the mesh and the surfaces around the geometries in the office model

are the parts with the most dense mesh structure and in other regions, less frequent mesh structure is preferred.

The indoor air was steady-state, incompressible flow and coincidence with the basic assumption of Boussinesq, invariable property. Considering the influence of buoyant force in the turbulence model, equation. Realizable k-ε model with the wall-function method were used.. Conservation of mass, energy and momentum equations as follows [16]unfinned in-line tube bank is simulated and compared with results from the literature. It is shown that the results are in accordance with the experimental studies in the literature. Heat transfer and pressure loss computations are carried out for four different axial and transversal pitch ratios; namely, (Formula presented.:

$$\frac{\partial u}{\partial x} + \frac{\partial v}{\partial y} = 0 \tag{1}$$

$$\frac{\partial}{\partial x}(\rho uu) + \frac{\partial}{\partial y}(\rho uv) = -\frac{\partial p}{\partial x} + 2\frac{\partial}{\partial x}\left[\mu_{eff}\frac{\partial u}{\partial x}\right] + \frac{\partial}{\partial y}\left[\mu_{eff}\left(\frac{\partial u}{\partial y} + \frac{\partial v}{\partial x}\right)\right] \tag{2a}$$

$$\frac{\partial}{\partial x}(\rho uv) + \frac{\partial}{\partial y}(\rho vv) = -\frac{\partial p}{\partial y} + \frac{\partial}{\partial x}\left[\mu_{eff}\left(\frac{\partial u}{\partial y} + \frac{\partial v}{\partial x}\right)\right] + 2\frac{\partial}{\partial y}\left[\mu_{eff}\frac{\partial v}{\partial y}\right] \tag{2b}$$

$$\frac{\partial}{\partial x}(\rho uT) + \frac{\partial}{\partial y}(\rho vT) = \frac{\partial}{\partial x}\left[\left(\frac{\mu}{Pr} + \frac{\mu_t}{Pr_t}\right)\frac{\partial T}{\partial x}\right] + \frac{\partial}{\partial y}\left[\left(\frac{\mu}{Pr} + \frac{\mu_t}{Pr_t}\right)\frac{\partial T}{\partial y}\right] \tag{3}$$

k-ε model turbulence model is chosen which is the two equation Reynolds – Averaged Navier Stokes based model and usually used in heat transfer problems. The Renormalization Group (RNG) k-ε turbulence model with enhanced wall treatment is selected because of its compatibility with the experimental works. Differential equations for turbulence energy dissipation rate (ε) and kinetic energy (k) are given in steady state as follows:

$$\frac{\partial}{\partial x}(\rho ku) + \frac{\partial}{\partial y}(\rho kv) = \frac{\partial}{\partial x}\left(\alpha_k \mu_{eff} \frac{\partial k}{\partial x}\right) + \frac{\partial}{\partial y}\left(\alpha_k \mu_{eff} \frac{\partial k}{\partial y}\right) + G_k - \rho$$

$$\frac{\partial}{\partial x}(\rho \epsilon u) + \frac{\partial}{\partial y}(\rho \epsilon v) = \frac{\partial}{\partial x}\left(\alpha_\epsilon \mu_{eff} \frac{\partial \epsilon}{\partial x}\right) + \frac{\partial}{\partial y}\left(\alpha_\epsilon \mu_{eff} \frac{\partial \epsilon}{\partial y}\right) + C_{1\epsilon} \frac{\epsilon}{k} G_k - C_{2\epsilon} \rho \frac{\epsilon^2}{k}$$

The inverse effective Prandtl numbers of ε and k are represented as α_k and α_ε, respectively. G_k denotes the turbulence kinetic energy generation and it is written as:

$$G_k = -\mu_t \left[2\left(\frac{\partial u}{\partial x}\right)^2 + 2\left(\frac{\partial v}{\partial y}\right)^2 + \left(\frac{\partial u}{\partial y} + \frac{\partial v}{\partial x}\right)^2 \right]$$

μ_{eff} is the effective turbulent viscosity and it can be calculated from;

$$\mu_{eff} = \mu + \mu_t$$

μ_t shows the turbulent (or eddy) viscosity,

$$\mu_t = \rho C_\mu \frac{k^2}{\epsilon}$$

where C_μ = 0.0845. The model constants C₁ and C₂ are given as 1.42 and 1.68, respectively

28.2. Physical Model

The dimensions of the modeled office room have been chosen as Length (X) x Height (Y) x Width (Z) = 4 m x 3.5 m

x 3 m. It has been accepted that there are people, refrigerators, lamps and computers in the room. Heat sources for the modeled office room are given in Table 2. It is acknowledged that the office does not have doors and windows. The configuration of the office room is given in Figure 2.

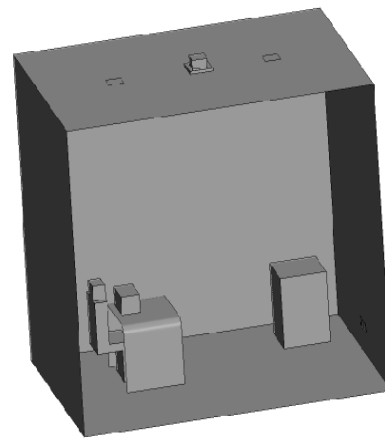


Figure 2. Geometrical arrangement of the office room.

28.3. Boundary Conditions

Table 2 shows the boundary condition for velocity and temperature at the air supply and exhaust. The cooling load according to the direction of the building is calculated according to the values given in Table 4. Cooling loads for humans, refrigerators, lamps and computers are taken from the ASHRAE basic manual. Heat sources for the modeled office room are given in Table 3. It is acknowledged that the office does not have doors and windows. Since there are temperature differences in the room, natural convection has occurred in the solution. The effect of Ra number was not examined in the study.

Table 2. Boundary conditions for case study

Diffuser	Flow Rate (kg/s)	T _{supply}	T _{exhaust}	T _{outdoor}
Square Diffuser(SD)	0.11	13 °C	23 °C	36 °C

Table 3. Heat sources for the modeled office room.

Heat Source	Cooling Load (W/m ²)
Person (seated)	70
Refrigerator	50
Lamp (2 pieces)	15
Computer	35
West wall	4
East wall	20
North wall	4
South wall	21
Floor	10
Ceiling	10

Table 4. Heat transfer coefficient values

	A (m ²)	U (W/m ² °C)
South	14	1.03
West	10.5	1.03
East	10.5	1.93
North	14	1.93
Ceiling	12	1.2
Floor	12	0.31

28.4. Mesh Independency Study

For the accuracy of CFD simulations and for the achievement of a fully converged solution, the quality of the grid plays an important role. It should be fine enough, particularly in the close zone of the diffuser, to avoid undesired numerical diffusion. The mesh independence is estimated and shown in Figure 3. In order to obtain an independent mesh result, three different mesh were chosen. It has been observed that the results with different mesh numbers are compatible with each other.

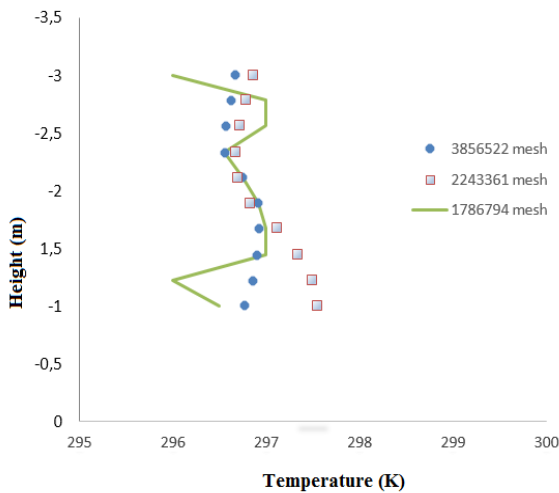


Figure 3. Square diffuser (SD) mesh independence

28.5. Validation of Study

Since there are no any studies to compare with described study in the literature, numerical calculations for velocity in the room compared with existing similar studies. The purpose of validation is to demonstrate the ability of the CFD model by using available experimental data to predict velocity. The CFD simulation is validated with experimental results from Particle Image Velocimetry (PIV) [17]. Geometrical and Reynolds number similarity were used to compare numerical study and experimental study. Figure 4 shows the comparisons between simulated and measured air velocity distributions. As a result, measured and simulated data agreed well.

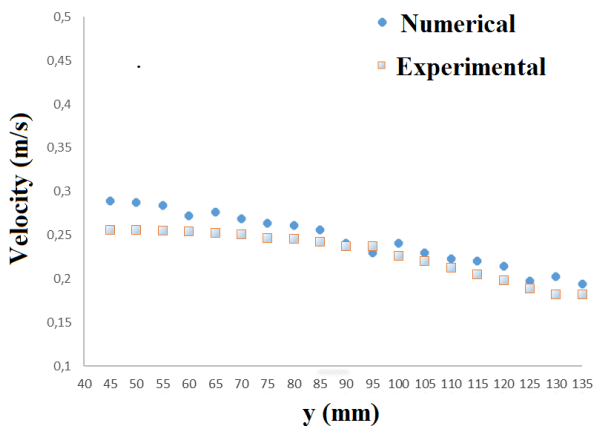


Figure 4. Comparison of PIV and CFD results

28.6. Calculation of PMV And PPD Values

While PMV and PPD were calculated, speed and temperature values were obtained from the CFD program. Metabolic rate, MRT, air relative humidity, clothing level values were accepted as 1 W/m², 2, % 60 and 0.6 m²C/W, respectively.

The PMV and equations are expressed as [6];

$$PMV = [0,303e^{-0,036M} + 0,028] \times \{ (M - W) - 3,05 \times 10^{-3} \times [5733 - 6,99(M - W) - p_a] - 0,42 \times [(M - W) - 58,15] - 1,7 \times 10^{-5} M (5867 - p_a) - 0,0014M(34 - t_a) - 3,96 \times 10^{-8} f_{cl} \times [(t_{cl} + 273)^{-4} - (\bar{t}_r + 273)^{-4}] - f_{cl} h_c (t_{cl} - t_a) \} \quad (9)$$

$$t_{cl} = 35,7 - 0,028(M - W) - I_{cl} \{ 3,96 \times 10^{-8} f_{cl} \times [(t_{cl} + 273)^{-4} - (\bar{t}_r + 273)^{-4}] + f_{cl} h_c (t_{cl} - t_a) \} \quad (10)$$

$$h_c = \begin{cases} 2,38(t_{cl} - t_a)^{0,25} & \text{icin } 2,38(t_{cl} - t_a)^{0,25} > 12,1\sqrt{v_{ar}} \\ 12,1\sqrt{v_{ar}} & \text{icin } 2,38(t_{cl} - t_a)^{0,25} < 12,1\sqrt{v_{ar}} \end{cases} \quad (11)$$

$$f_{cl} = \begin{cases} 1,00 + 1,290I_{cl} & \text{icin } I_{cl} < 0,078m^2c/w \\ 1,05 + 0,645I_{cl} & \text{icin } I_{cl} > 0,078m^2c/w \end{cases} \quad (12)$$

PPD is expressed by Fanger as a function of PMV, and its calculation is given in the following equation.

$$PPD = 100 - 95e^{-(0,03353 \times PMV^4 + 0,2179 \times PMV^2)} \quad (13)$$

29. RESULTS AND DISCUSSIONS

The levels of 0. 1, 0.6, and 1.1 meters correspond to ASHRAE's recommended measurement heights for seated subjects. Therefore in this study, measuring the airflow temperatures and velocities were set at the height of 0.1, 0.6 and 1.1 meters above the floor [9].

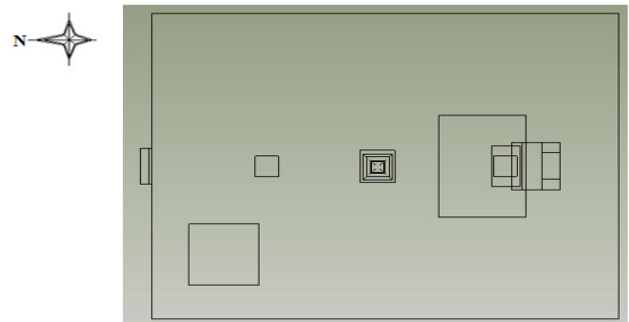


Figure 5. Top view of the office room

The PPD distribution contours of office room at the height of 0. 1, 0.6, and 1.1 are seen in Figure 6, Figure7 and Figure 8 respectively. From the PPD index in Figure 6 and 7, it can be seen that the indoor thermal comfort are uniform. Major portions of the office room are having a PPD value is between 0-20 %. The PPD contours where the value is less than 20 percent indicates that people are likely to feel slightly cool in the north part of the room. The PPD contours are shown for the height of 0.1 m in Figure 8. The large zone is affected by a PPD 20 % and below. However, the PPD value is varying drastically from 20 to 40 % in the central region of the office room and nearer to north wall face. When the office room, which is generally modeled, is air-conditioned using a square diffuser, it provided the thermal comfort conditions.

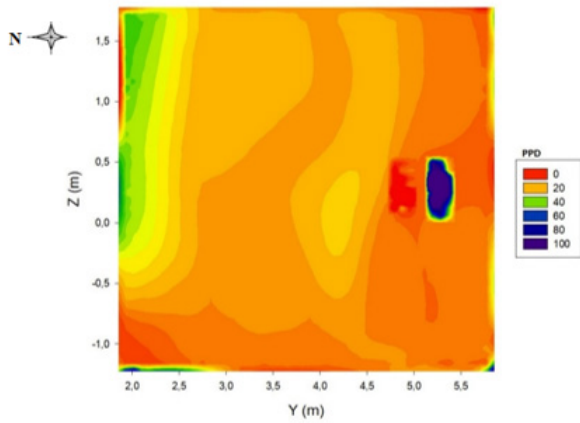


Figure 6. The PPD distribution contour of office room at the height of 0.1m

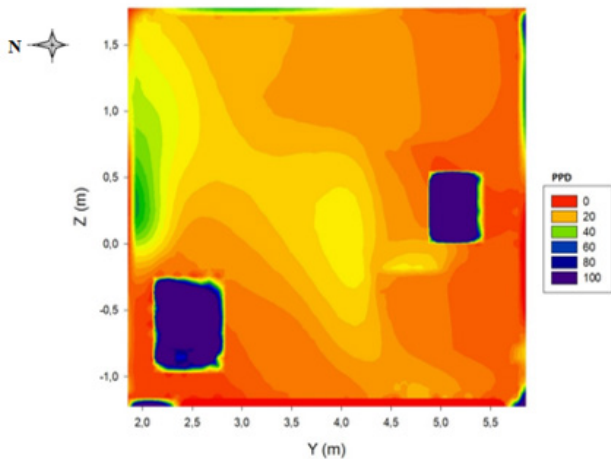


Figure 7. The PPD distribution contour of office room at the height of 0.6

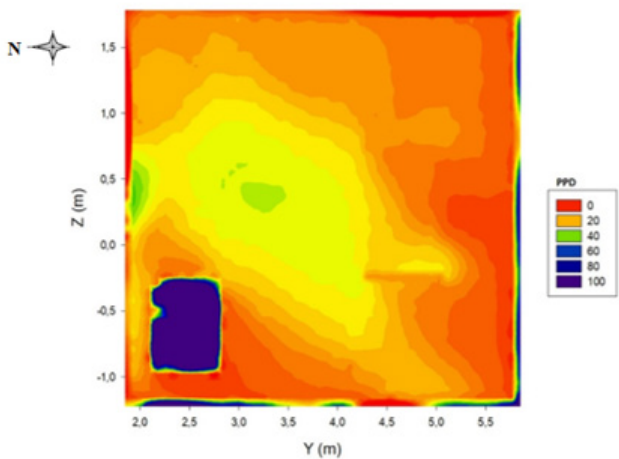


Figure 8. The PPD distribution contour of office room at the height of 1.1m

30. CONCLUSION

In HVAC engineering, CFD, an important tool, has been used to analyze data produced by models representing the complexities of flows evolve in the ventilated spaces. In a simplified office room, this study presents the results of a set of numerical investigations into the performance of square ceiling diffusers. ASHRAE thermal comfort conditions are observed in the air conditioning space with square diffuser. The values of PPD similar at different heights in the model

office room. In the place, the PPD is commonly less than 20%. However, the PPD value is varying drastically from 20 percent to 40 percent at the height of 1.1 meter in the some places of room.

The study also show that choosing the diffuser plays an important role in air-conditioning works, providing thermal comfort in home and workplace environments where people are present. In our previous work [18], we changed only the displacement and model of the diffuser in the room with the same physical features as this study. The comparison between two diffusers shows that a square diffuser at the same boundary conditions supplies better thermal comfort conditions of the office room.

As a continuation of this study; Numerical calculations can be made considering that there are objects and people in places with different geometries. While making these numerical calculations, parameters such as diffusers' inlet and outlet locations, diffuser geometry and number, different air velocities, doors and windows can be taken into consideration.

31. NOMENCLATURE

c_p	fluid specific heat, (kJ / kg)
C_a	model constant, ref.
C_a	model constant, ref.
f_{cl}	Ratio of clothed surface area
h_c	Convection heat transfer coefficient (W/ (m ² .K))
P	Pressure (Pa)
I_{cl}	Basic clothing insulation (m ² . °C /W)
M	Metabolic rate (W/m ²)
Pr	Prandtl number
q''	heat flux (W / m ²)
p_a	Water vapor partial pressure (Pa)
Re	Reynolds number
T	Temperature (°C)
t_a	Ambient air temperature (°C)
t_r	Mean radiant temperature (°C)
t_{cl}	Clothing surface temperature (°C)
W	Effective mechanic power (W/m ²)
v_{ar}	Relative air velocity (m/s)
u	velocity in x direction (m / s)
v	velocity in y direction (m / s)
x	x coordinate
y	y coordinate

Greek

β	pressure gradient, eq. (17), (Pa / m)
\dot{a}	energy dissipation rate (m^2 / s^3)
ν	kinematic viscosity (m^2 / s)
θ	dimensionless temperature, eq.
ρ	density (kg / m^3)
$\diamond p$	pressure loss, eq.
μ	dynamic viscosity $(Pa.s)$
μ_t	turbulent viscosity, eq.
μ_{eff}	effective turbulent viscosity, eq.
α_k	inverse effective Prandtl number of k
$\alpha_{\dot{a}}$	inverse effective Prandtl number of \dot{a}

REFERENCES

- [1] Ahmed, A.Q., Gao, S., Kareem, A.K., (2016). A numerical study on the effects of exhaust locations on energy consumption and thermal environment in an office room served by displacement ventilation. *Energy Conversion and Management*. 117: 74–85. doi: 10.1016/j.enconman.2016.03.004.
- [2] Ozsagiroglu, S., (2020). Bir mahalın termal konfor şartlarının hesaplamalı akışkanlar dinamiği yöntemi ile analizi. *Yıldız Teknik Üniversitesi*, (2020).
- [3] Volkov, A.A., Sedov, A. V., Chelyshkov, P.D., (2014). Modelling the thermal comfort of internal building spaces in social buildings. *Procedia Engineering*. 91(TFoCE): 362–7. doi: 10.1016/j.proeng.2014.12.075.
- [4] Bilgili, M., Şahin, B., Şimşek, E., Özbek, A., Yaşar, A., (2019). Heat Loss and Exergy Flow through Respiration of the Human Body under Different Meteorological Conditions. *European Mechanical Science*. 3(2): 45–51. doi: 10.26701/ems.531702.
- [5] Awad, A.S., Calay, R.K., Badran, O.O., Holdo, A.E., (2008). An experimental study of stratified flow in enclosures. *Applied Thermal Engineering*. 28(17–18): 2150–8. doi: 10.1016/j.applthermaleng.2007.12.017.
- [6] Cheng, Y., Niu, J., Du, Z., Lei, Y., (2015). Investigation on the thermal comfort and energy efficiency of stratified air distribution systems. *Energy for Sustainable Development*. 28: 1–9. doi: 10.1016/j.esd.2015.05.007.
- [7] KEE-CHIANG CHUNG., JEN-YU Kuo., (1999). Location on Thermal Comfort Analysis with Different Air Distribution Strategies. *J. THERMAL EN1/ & BLDG.& BLDG.* 22: 208–29.
- [8] He, G., Yang, X., Srebric, J., (2005). Removal of contaminants released from room surfaces by displacement and mixing ventilation: Modeling and validation. *Indoor Air*. 15(5): 367–80. doi: 10.1111/j.1600-0668.2005.00383.x.
- [9] d'Ambrosio Alfano, F.R., Ianniello, E., Palella, B.I., (2013). PMV-PPD and acceptability in naturally ventilated schools. *Building and Environment*. 67: 129–37. doi: 10.1016/j.buildenv.2013.05.013.
- [10] Li, Q., Zhang, T., Lv, W., (2009). European Journal of Medicinal Chemistry Original article A novel spectrophotometric method for the determination of aminophylline with boric acid in pharmaceutical and mixed serum samples. *European Journal of Medicinal Chemistry*. 44(4): 1452–6. doi: 10.1016/j.ejmech.2008.09.046.
- [11] Han, W.P., Gu, X.L., (2008). Application of binnacles to terminal 3 of Beijing Capital-International Airport and air distribution simulation. *J HVAC*. 38(115): 9.
- [12] Lau, S.S.Y., Zhang, J., Tao, Y., (2019). A comparative study of thermal comfort in learning spaces using three different ventilation strategies on a tropical university campus. *Building and Environment*. 148: 579–99. doi: 10.1016/j.buildenv.2018.11.032.
- [13] Khalil, A., Bassuoni, M.M., Elsamadony, M.O., Raslan, M.A., (2020). Assessment of Thermal Comfort in Operating Rooms Using PMV-PPD Model 2.
- [14] Marchenko, A., Temeljotov-Salaj, A., Rizzardi, V., Oksavik, O., (2020). The study of facial muscle movements for non-invasive thermal discomfort detection via bio-sensing technology. Part I: Development of the experimental design and description of the collected data. *Applied Sciences (Switzerland)*. 10(20): 1–29. doi: 10.3390/app10207315.
- [15] Shaharon, M.N., Jalaludin, J., (2012). Thermal comfort assessment-a study toward workers' satisfaction in a low energy office building. *American Journal of Applied Sciences*. 9(7): 1037–45. doi: 10.3844/ajassp.2012.1037.1045.
- [16] Nasif Kuru, M., Yilmaz, A., Aktaş, A.E., Erdinç, M.T., (2020). Numerical investigation of flow and heat transfer in axially-finned in-line tube banks. *Energy Sources, Part A: Recovery, Utilization and Environmental Effects*. 00(00): 1–16. doi: 10.1080/15567036.2020.1826600.
- [17] Yildirim, A., (2019). Numerical and experimental investigation of velocity and temperature distribution of an air conditioned room. *Osmaniye Korkut Ata University*, (2019).
- [18] Yildirim, A., Ozalp, C., (2019). Jet Lüle ile İklimlendirmesi Yapılan Bir Ofis Modelinde Konfor Seviyesinin (PMV/PPD) Sayısal Olarak Belirlenmesi. *Çukurova University Journal of the Faculty of Engineering and Architecture*. 34(September): 207–17.

Instructions for authors

All manuscripts must be in English. Pages should be numbered sequentially. The manuscript should be composed in accordance with the Article Template given above. The maximum length of contributions is 10 pages. For full instructions see the Information for Authors section on the journal's website:

<http://dergipark.gov.tr/ems/page/2805>

FORMAT OF THE MANUSCRIPT

The manuscript should be composed in accordance with the Article Template.

The manuscript should be written in the following format:

- A Title that adequately describes the content of the manuscript.
- A list of Authors and their affiliations.
- An Abstract that should not exceed 550 words. The Abstract should state the principal objectives and the scope of the investigation, as well as the methodology employed. It should summarize the results and state the principal conclusions.
- 4-6 significant key words should follow the abstract to aid indexing.
- An Introduction that should provide a review of recent literature and sufficient background information to allow the results of the article to be understood and evaluated.
- An Experimental section that should provide details of the experimental set-up and the methods used to obtain the results.
- A Results section that should clearly and concisely present the data, using figures and tables where appropriate.
- A Discussion section that should describe the relationships and generalizations shown by the results and discuss the significance of the results, making comparisons with previously published work. (It may be appropriate to combine the Results and Discussion sections into a single section to improve clarity.)
- A Conclusions section that should present one or more conclusions drawn from the results and subsequent discussion and should not duplicate the Abstract.
- Acknowledgement (optional) of collaboration or preparation assistance may be included. Please note the source of funding for the research.
- References must be cited consecutively in the text using square brackets [1] and collected together in a reference list at the end of the manuscript.

FIGURES

Figures (figures, graphs, illustrations digital images, photographs) must be cited in consecutive numerical order in the text and referred to in both the text and the captions as Figure 1, Figure 2, etc. Figures should be prepared without borders and on white grounding and should be sent separately in their original formats. If a figure is composed of several parts, please mark each part with a), b), c), etc. and provide an explanation for each part in Figure caption. The caption should be self-explanatory. Letters and numbers should be readable (Arial or Times New Roman, min 6 pt with equal sizes and fonts in all figures).

Graphics (submitted as supplementary files) may be exported in resolution good enough for printing (min. 300 dpi) in any common format, e.g. TIFF, BMP, GIF or JPG, PDF. However, graphs and line drawings should be prepared as vector images, e.g. CDR, AI.

Multi-curve graphs should have individual curves marked with a symbol or otherwise provide distinguishing differences using, for example, different thicknesses or dashing.

TABLES

Tables should carry separate titles and must be numbered in consecutive numerical order in the text and referred to in both the text and the captions as Table 1, Table 2, etc. In addition to the physical quantities, such as τ (in italics), the units (normal text) should be added in square brackets. Tables should not duplicate data found elsewhere in the manuscript. Tables should be prepared using a table editor and not inserted as a graphic.

REFERENCES

A reference list must be included using the following information as a guide. Only cited text references are to be included. Each reference is to be referred to in the text by a number enclosed in a square bracket (i.e. [3] or [2] to [4] for more references; do not combine more than 3 references, explain each).

References must be numbered and ordered according to where they are first mentioned in the paper, not alphabetically. All references must be complete and accurate. Please add DOI code when available. Examples follow.

Journal Papers:

Surname 1, Initials, Surname 2, Initials (year). Title. Journal, volume, number, pages, DOI code.

[1] Calikoz, R., Ozcanli, B., Serin, F., (2017). Simulating nonlinear materials under vertical forces by using intelligent . European Mechanical Science, 57(8): 531-538, DOI:10.5545/ems.2017.013.

Journal titles should not be abbreviated. Note that journal title is set in italics.

Books: Surname 1, Initials, Surname 2, Initials (year). Title. Publisher, place of publication.

[2] Ozgur, M.P. (2012). Fundamentals of Mechanical Engineering. Gunlubey, Ankara.

Chapters in Books:

Surname 1, Initials, Surname 2, Initials (year). Chapter title. Editor(s) of book, book title. Publisher, place of publication, pages.

[3] Akarca, G., Gelidor, M. (2016). Mechanical robotic systems. Calicka, V., Kurbetoglu, A., Merdan, M. (Eds.), Cutting Edge Robotics. Literatur Bergli, Mammendorf, 553-576.

Proceedings Papers:

Surname 1, Initials, Surname 2, Initials (year). Paper title. Proceedings title, pages.

[4] Seferci, N., Malikoglu, S., Tosun, N. (2009). Applied mechanic in process industry. IMSEC 2016 Conference Proceedings, 422-427.